NEA Leak Rate Benchmark

Final Report

OECD
BETTER POLICIES FOR BETTER LIVES

NEA
NUCLEAR ENERGY AGENCY

NUCLEAR ENERGY AGENCY
COMMITTEE ON THE SAFETY OF NUCLEAR INSTALLATIONS

NEA Leak Rate Benchmark Final Report

This document is available in PDF format only.

JT03539241

ORGANISATION FOR ECONOMIC CO-OPERATION AND DEVELOPMENT

The OECD is a unique forum where the governments of 38 democracies work together to address the economic, social and environmental challenges of globalisation. The OECD is also at the forefront of efforts to understand and to help governments respond to new developments and concerns, such as corporate governance, the information economy and the challenges of an ageing population. The Organisation provides a setting where governments can compare policy experiences, seek answers to common problems, identify good practice and work to co-ordinate domestic and international policies.

The OECD member countries are: Australia, Austria, Belgium, Canada, Chile, Colombia, Costa Rica, Czechia, Denmark, Estonia, Finland, France, Germany, Greece, Hungary, Iceland, Ireland, Israel, Italy, Japan, Korea, Latvia, Lithuania, Luxembourg, Mexico, the Netherlands, New Zealand, Norway, Poland, Portugal, the Slovak Republic, Slovenia, Spain, Sweden, Switzerland, Türkiye, the United Kingdom and the United States. The European Commission takes part in the work of the OECD.

OECD Publishing disseminates widely the results of the Organisation's statistics gathering and research on economic, social and environmental issues, as well as the conventions, guidelines and standards agreed by its members.

NUCLEAR ENERGY AGENCY

The OECD Nuclear Energy Agency (NEA) was established on 1 February 1958. Current NEA membership consists of 34 countries: Argentina, Australia, Austria, Belgium, Bulgaria, Canada, Czechia, Denmark, Finland, France, Germany, Greece, Hungary, Iceland, Ireland, Italy, Japan, Korea, Luxembourg, Mexico, the Netherlands, Norway, Poland, Portugal, Romania, Russia (suspended), the Slovak Republic, Slovenia, Spain, Sweden, Switzerland, Türkiye, the United Kingdom and the United States. The European Commission and the International Atomic Energy Agency also take part in the work of the Agency.

The mission of the NEA is:

- to assist its member countries in maintaining and further developing, through international co-operation, the scientific, technological and legal bases required for a safe, environmentally sound and economical use of nuclear energy for peaceful purposes;

- to provide authoritative assessments and to forge common understandings on key issues as input to government decisions on nuclear energy policy and to broader OECD analyses in areas such as energy and the sustainable development of low-carbon economies.

Specific areas of competence of the NEA include the safety and regulation of nuclear activities, radioactive waste management and decommissioning, radiological protection, nuclear science, economic and technical analyses of the nuclear fuel cycle, nuclear law and liability, and public information. The NEA Data Bank provides nuclear data and computer program services for participating countries.

COMMITTEE ON THE SAFETY OF NUCLEAR INSTALLATIONS (CSNI)

The Committee on the Safety of Nuclear Installations (CSNI) addresses Nuclear Energy Agency (NEA) programmes and activities that support maintaining and advancing the scientific and technical knowledge base of the safety of nuclear installations.

The Committee constitutes a forum for the exchange of technical information and for collaboration between organisations, which can contribute, from their respective backgrounds in research, development and engineering, to its activities. It has regard to the exchange of information between member countries and safety R&D programmes of various sizes in order to keep all member countries involved in and abreast of developments in technical safety matters.

The Committee reviews the state of knowledge on important topics of nuclear safety science and techniques and of safety assessments, and ensures that operating experience is appropriately accounted for in its activities. It initiates and conducts programmes identified by these reviews and assessments in order to confirm safety, overcome discrepancies, develop improvements and reach consensus on technical issues of common interest. It promotes the co-ordination of work in different member countries that serve to maintain and enhance competence in nuclear safety matters, including the establishment of joint undertakings (e.g. joint research and data projects), and assists in the feedback of the results to participating organisations. The Committee ensures that valuable end-products of the technical reviews and analyses are provided to members in a timely manner, and made publicly available when appropriate, to support broader nuclear safety.

The Committee focuses primarily on the safety aspects of existing power reactors, other nuclear installations and new power reactors; it also considers the safety implications of scientific and technical developments of future reactor technologies and designs. Further, the scope for the Committee includes human and organisational research activities and technical developments that affect nuclear safety.

Acknowledgements

Leading authors

Klaus HECKMANN   Gesellschaft für Anlagen- und Reaktorsicherheit, Germany

Contributors

Robert TREGONING   Chair of the Metal Subgroup, WGIAGE

Table of contents

List of tables

List of figures

List of abbreviations and acronyms

AEA	Atomic Energy Authority (United Kingdom)
ASME	American Society of Mechanical Engineers
B&PV	Boiler and Pressure Vessel
BfE	Bundesamt für kerntechnische Entsorgungssicherheit (Federal Office for the Safety of Nuclear Management, Germany)
BPVC	Boiler and Pressure Vessel Code
CAPS	CSNI Activity Proposal Sheet
CDR	Critical discharge rate
CF	Corrosion fatigue
CFD	Computational fluid dynamic
CFP	Crack face pressure
COA	Crack opening area
COD	Crack opening displacement
CPS	Computer program services
CSNI	Committee on the Safety of Nuclear Installations (NEA)
EPRI	Electric Power Research Institute (United States)
FEA	Finite Element Analysis
FSI	Fluid-structure-interaction
GUI	Graphical User Interface
HEM	Homogeneous equilibrium model
IAEA	International Atomic Energy Agency
ID	Inside diameter
IGSCC	Intergranular stress corrosion cracking
LBB	Leak-before-break
LEAPOR	Leak Analysis of Piping – Oak Ridge
MERIT	Maximizing Enhancements in Risk-Informed Technology
MW	Mid-wall
NEA	Nuclear Energy Agency
NRC	Nuclear Regulatory Commission (United States)
OD	Outside diameter
OECD	Organisation for Economic Co-operation and Development
ORNL	Oak Ridge National Laboratory (United States)
PWSCC	Primary water stress corrosion cracking

QA	Quality assurance
SCALE	Slit and Crack Analysis for Leak Estimation
SIA	Structural Integrity Associates, Inc.
SQA	Software Quality Assurance
WGIAGE	Working Group on Integrity and Ageing of Components and Structures (NEA)
WRC	Welding Research Council
xLPR	Extremely Low Probability of Rupture

Executive summary

Background

In the piping and components of nuclear power plants, degradation mechanisms may lead to wall-penetrating defects that may cause water to leak to the containment. One important aspect of these leaks is that they offer an opportunity to rapidly detect the defects and take countermeasures, which is part of the leak-before-break concept (LBB).

In assessing the consequences of a leak, it is important to estimate the mass flow rate through a defect. This encouraged the development of models to predict and compute the mass flow rates through leaks and also several experimental tests for the validation of these models.

The activity presented in this report was approved by the Nuclear Energy Agency (NEA) Committee on the Safety of Nuclear Installations (CSNI) in December 2018 (as recorded in the "Summary Record of the 64th Meeting of the Committee on the Safety of Nuclear Installations" [NEA/SEN/SIN(2018)3] [not publicly available]). The benchmark was conducted under the metal subgroup of the NEA Working Group on Integrity and Ageing of Components and Structures (WGIAGE). This report was approved by the CSNI on 30 May 2022 and prepared for publication by the NEA Secretariat.

Objective

The objective of this study is to compare leak rate computation practices and the applied tools and software solutions. Leak rate prediction is an important aspect of the leak-before-break assessment, as assessing the detectability of leaks requires an appropriate understanding of a fluid's flow through wall-penetrating cracks. In this context, the defects are postulated, and inevitable uncertainties concerning the exact geometric shape of defects are present. Therefore, the attainable accuracy of a leak rate prediction is fundamentally limited, so that complex three-dimensional numerical fluid simulations for leak flow are rare, and one-dimensional simulations are primarily used. However, the determination of the geometric shape and the influence of the surface morphology are also important aspects of the leak rate computation.

Work performed

Participants from ten organisations representing eight countries contributed analysis results to this comparative benchmark study. The participants described their individual approaches, applied tools, underlying methods and input data settings. The reporting of intermediate results within the analysis, if applicable and available, supported the interpretation and discussion of the results comparison. Besides the mass flow rate, the crack opening displacement was also determined for specific tasks.

Besides the actual cases, the analysis documentation and the comparison, this report also contains a compendium of methods. This compendium summarises the individual approaches for leak opening, morphology and flow resistance, and the fluid mechanical modelling, which are combined by the different participants in modular ways to predict leak flow rates. The compendium shows the conceptual differences in the different approaches and demonstrates that there is a variety of approaches that can be combined in different ways. The detailed descriptions of the individual model ingredients allow for an efficient comparison of the participants' approaches in the analysis cases.

The benchmark comprises two phases. The first phase involved open computation, i.e. the measured leak rates were communicated to the participants together with the actual leak setup. This initial phase made possible a common understanding of case descriptions and

analysis requirements in order to avoid misinterpretations and unclear specifications. The second phase involved blind analysis cases, cases where the measured leak rate value was not communicated to the participants. In the comparison of open and blind analysis cases, the obtained accuracy was similar.

Both phases started with the analysis of specimen tests measured at the Materials Testing Institute at the University of Stuttgart, Germany. In these laboratory tests, the flow rate of water under different stagnation conditions through artificial slits and fatigue cracks was measured.

Results and their significance

The analysis results show that the individual approaches can accurately predict the flow through these specimens, even for the blind analysis cases. Moreover, the methodological survey made it possible to group the results by assumptions concerning morphology/flow resistance and the applied flow model, which shows that participants applying similar models with different implementations obtain the same results.

Following a recommendation of the WGIAGE metal subgroup, the benchmark study also proposed one open and one blind analysis of an actual leak incident in an operating nuclear power plant. The analysis of these incidents confirmed that the uncertainties in a real leak case are much larger than in a laboratory test with controlled conditions, and it was expected that the assessment would give an estimate of a range of plausible values. In fact, the guesses and estimates by the participants in the leak assessment were consistent, and the estimated range of possible flow rates through a leak was in accordance with the necessary assumptions. It was found that the reported leak rate of one case could not be explained by the leak finding and the operational conditions, as all computational assessments underpredicted the reported leak rate. While being conservative with respect to the leak-before-break assessment, this finding shows that the validation of leak rate assessment methods with real leak incidents should be considered more intensively in the future in order to check if this is a singular finding and to assess the suitability of leak rate computation approaches for leaks in actual operating plants.

The parallel leak-before-break (LBB) benchmark study motivated the investigation of specific cases related to the LBB assessment and allowed a study of the details of leak rate computations for exercises from the LBB benchmark. The two sensitivity studies involved investigating specific assumptions in the leak rate computation and the influence of the different model approaches.

As an additional analysis case, a thin laboratory specimen inspired by steam generator tube leaks was also included in the analysis. This made it possible to assess also the suitability of different methods for the computation of leak flow through thin-walled specimens.

Conclusions and recommendations: the lessons learnt from the benchmark

- Leak rate tests under controlled conditions can be reproduced well by the available methods and tools. Differences between the computations and the measurements, as well as differences between different approaches, are satisfyingly small.
- Uncertainties in a real leak case are much larger than in a laboratory test with controlled conditions. Validation of leak rate assessment methods with real leak incidents should be considered more intensively in the future.
- The approach of documenting the individual models and tools showed that the leak rate computation can be a transparent combination of assumptions and computational models, instead of being a result of black box-like software.

Finally, it should be stated that the benchmark profited from the parallel activities of the LBB benchmark and the probabilistic fracture mechanics benchmark. In both activities,

leak rate assessment is a part of the analysis, and the present methodological survey and comparison helps with the interpretation of submitted results in the two adjoining activities.

1. Introduction and background

In the piping and components of nuclear power plants, degradation mechanisms may lead to wall-penetrating defects that cause a loss of the medium – in many cases it is cooling water leaking to the containment. These leaks are key events because they offer the opportunity to rapidly detect the defect and take countermeasures, which is a part of the leak-before-break concept (LBB). However, leaks are of course also a source of concern with respect to the loss of coolant from the coolant loop and with respect to damage to the exterior side, such as internal flooding, jet damage and pipe whip, and radiation release.

To assess the consequences of a leak, it is important to estimate the mass flow rate through a defect. This leak rate computation is a key part of the discussion of the aforementioned scenarios, and the result of this computation has an impact on the assessment of the safety relevance. This motivated the development of models to predict and compute the mass flow rates through leaks, as well as experimental tests for the validation of these models. Also, software products have emerged which facilitate the computation.

Due to the increasing importance of the LBB approach, the reliability of leak rate assessments is a key topic. This motivated the CSNI to address once again the question of leak rate computation practices, after a similar benchmark study in the 1990s focused on LBB concepts, and as another benchmark study on probabilistic fracture mechanics was about to start. In 2019, the metals subgroup of the Working Group on Integrity and Ageing of Components and Structures (WGIAGE) discussed a CSNI Activity Proposal Sheet (CAPS) on leak rate computation. While the activity is based on laboratory tests at the University of Stuttgart, the metals subgroup members commented on the CAPS, which led to an extension of the scope of the work.

This report is organised as follows. In Chapter 2, a compendium of methods summarises all the approaches that have been applied to the leak rate benchmark problems. The two phases of the benchmark are presented in Chapters 3 and 4; both show the exercise set, the computation documentation and the result synopsis in consecutive subsections. The report concludes with Chapter 5, which contains recommendations for future work.

2. Leak rate assessment: compendium of methods

2.1. Introduction

For the computation of leak flow rates, different aspects have to be considered that influence the final assessment. According to the investigation [1], these aspects can be sorted into three categories:

a. the cross section of the leak

b. the consideration of the morphology of the leak and the resulting fluid-dynamical resistance

c. the fluid motion together with the evaporation.

In each of these aspects, different approaches can be used for computation, which gives rise to a potentially high number of model combinations. This chapter is intended to provide a reference for the different models and assumptions applied within this benchmark. This short presentation is given in Sections 2.2, 2.3, and 2.4 for the leak opening, the flow resistance, and the fluid modelling, respectively. In Section 2.5, the software tools applied within this benchmark activity are presented. Section 2.6 is dedicated to regulatory aspects of specific models in codes and standards.

2.2. Leak opening computation

This part of the compendium gives a comprehensive summary of the methods applied by the different participants. The survey aims to present all approaches in a unified nomenclature. Crack opening displacement (COD) computations are required in the benchmark for through-thickness cracks in cylindrical pipes; the relevant geometrical properties for the characterisation are shown in Figure 2.1.

Figure 2.1. Geometrical characterisation of idealised cracks in cylindrical pipes
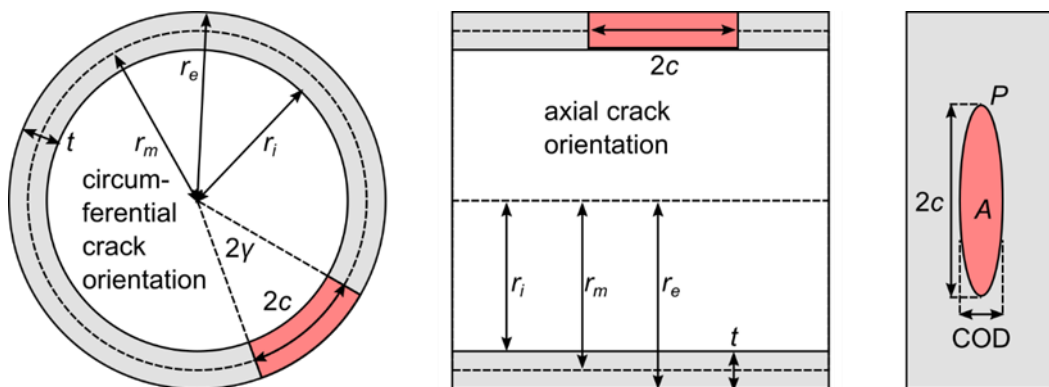
The computation involves the crack opening stresses, which give rise to a finite cross section area A enabling a leakage flow. The typical situations are interior pressure p and, for circumferential cracks, bending moment M. The nominal stresses (in absence of a crack and in the limit of $t \ll r_m$) in these situations can be derived analytically.

$$\sigma_a = \frac{r_i^2}{r_e^2 - r_i^2}p + \frac{M}{J_z}r_e\cos\varphi \approx \frac{r_m}{2t}p + \frac{M}{J_z}r_e\cos\varphi \qquad (1)$$

The moment of inertia is defined as $J_z = \left(r_e^4 - r_i^4\right)\pi/4$, and φ is the angle measured from the maximal bending. As the crack opening stresses act perpendicular to the orientation, the axial stresses σ_a are relevant for circumferential cracks, while the circumferential stresses σ_c are relevant for axial cracks.

$$\sigma_c = 2\frac{r_i^2}{r_e^2 - r_i^2}p \approx \frac{r_m}{t}p \qquad (2)$$

From these formulas, it is clear that the membrane stress acting on the crack faces is a multiple of the interior pressure. In case of leak flow, the space within the crack faces is also filled with pressurised fluids, thus a crack face pressure should be considered. However, the pressure is decreasing along the radial co-ordinate, typically between full pressure and saturation pressure for critical two-phase flow (see also Section 2.4.6), or between full pressure and ambient pressure for subcritical flow (less relevant for nuclear application).

Common characteristics of the pipe material are the elastic modulus E, the Poisson number ν, the yield stress σ_y, and the ultimate stress σ_u. The parametrisation of the stress-strain curve with a Ramberg-Osgood formula is also useful.

$$\epsilon(\sigma) = \epsilon_0\left[\frac{\sigma}{\sigma_0} + \alpha\left(\frac{\sigma}{\sigma_0}\right)^n\right] \qquad (3)$$

The determination of the cross section A (also called crack opening area [COA]) is a standard fracture mechanical problem which computes the displacements of the crack faces under consideration of material properties, loads and crack tip effects. The state of the art for this task is the use of elastic-plastic Finite Element Analysis (FEA), which can lead to the most accurate results. However, a number of analytical formulations for COA and COD have been proposed for standard situations. The methods applied in the benchmark are discussed in the following subsections.

2.2.1. Ductile Fracture Handbook, GE/EPRI method or Zahoor method

The GE/EPRI method for COD computation is based on references [2] and [3]. It is an approximative elastic-plastic approach for materials obeying a Ramberg-Osgood stress-strain behaviour. The COD can be written as the sum of an elastic and a plastic part.

$$COD = COD_{el} + COD_{pl} \qquad (4)$$

The elastic crack opening is computed by the V_1 function and the elastic material properties, together with the geometrical properties. For pure pressure loads (interior pressure p), the elastic contribution reads as follows.

$$COD_{el} = \frac{2a}{\pi r t}V_1\left(\frac{\gamma}{\pi}, \frac{r_m}{t}\right)\frac{p}{E} \qquad (5)$$

The elastic part for pure bending loads (bending moment M) uses the same V_1 function and also the moment of intertia I.

$$COD_{el} = \frac{4ar}{I} V_1\left(\frac{\gamma}{\pi}, \frac{r_m}{t}\right) \frac{M}{E} \tag{6}$$

The V_1 function depends on the ratio of pipe radius to wall thickness, and the angle of the crack γ/π just gives the fraction of the crack on the full circumference. The V_1 value is computed by FEA; the values from [5] are summarised in Table 2.1.

Table 2.1. Elastic coefficients for the GE/EPRI method, from [5].

γ/π	r_m/t	5	10	20
1/16		1.234	1.206	1.111
1/8		1.388	1.480	1.482
1/4		2.008	2.379	3.079
1/2		5.331	7.165	11.585

The plastic part is available either for pressure or for bending – while the linear-elastic solutions for separate loads can be superposed, this is not possible in the strict sense by the basic GE/EPRI method as proposed in [3]. The plastic part due to pressure p is based on the h_2 function.

$$COD_{pl} = \alpha\, \epsilon_0\, h_2\left(\frac{a}{b}, n, \frac{r}{t}\right)\left(\frac{p}{p_0}\right)^n \tag{7}$$

The plastic part in presence of a bending moment M is similar, with another h_2 function for this load case.

$$COD_{pl} = \alpha\, \epsilon_0\, h_2\left(\frac{a}{b}, n, \frac{r}{t}\right)\left(\frac{M}{M_0}\right)^n \tag{8}$$

An extension of the method is the consideration of a h_2-function for combined pressure and bending load – while the linear terms can be superposed, the plastic COD for combined loading requires its own h_2 function.[5] proposes to consider a constant PWR-like pressure and compute the plastic COD with a h_2 function for variable bending in the presence of this pressure. The h_2-coefficients for this load are summarised in Table 2.2.

Table 2.2. h_2 values for 15.51 MPa pressure in combination with bending from [5]

γ/π	r_m/t	$n = 2$	$n = 3$	$n = 3$	$n = 7$	$n = 10$
1/16	5	6.851	7.115	7.232	6.979	6.153
1/8	5	6.182	5.918	5.312	4.766	3.580
1/16	10	6.973	7.460	8.108	8.923	9.009
1/8	10	6.888	6.868	6.844	6.181	6.578
1/16	20	7.561	8.292	10.924	14.078	15.813
1/8	20	8.375	8.705	10.383	12.479	13.051

An extension to axial through-wall cracks under pressure loads is proposed in [37], where an adjusted V- and h_2-function is derived.

2.2.2. GE/EPRI elastic

This method is based on [2] and [3] as described in Section 2.2.1. It can also be used by skipping the plastic part of the model, thus by only considering equations (5) and (6). Since this approach does not require the numerical tables of the full GE/EPRI method, it is technically much simpler. However, its validity is restricted to smaller loadings.

2.2.3. GRS-PB method

The GRS-PB method [4] is a generalisation of the Wüthrich assessment [6] which allows computing the COA under combined membrane stress and bending loads. It is constructed as an underestimating approach for the conservative underestimation of the leak area in an LBB assessment. It is based on the elastic opening area of a crack in a plate under a stress σ.

$$A_{\text{plate}}^{\text{elastic}} = 2\,\pi\,\frac{\sigma}{E'}\,c^2 \tag{9}$$

In this equation, E' is the modulus of elasticity E for plane stress state, and $E/(1 - \nu^2)$ for plane strain. The bulging function $\alpha(\lambda)$ is used to map the solution to a cylindrical structure.

$$\alpha\left(\lambda_s = \frac{\sqrt[4]{12(1-\nu^2)}c}{\sqrt{r_m t}}\right) = \begin{cases} 1 + 0.1\lambda_s + 0.16\,\lambda_s^2 & \text{axial crack} \\ \sqrt{1 + 0.177\lambda_s^2} & \text{circumferential} \end{cases} \tag{10}$$

The shell parameter λ_s is a dimension-less quantity depending on the geometry of the pipe and the crack. The idea of the GRS-PB approach to modify this formulation by Wüthrich is to replace the stress σ with an equivalent of the bending stress.

$$A_{\text{GRS-PB}} = \alpha(\lambda_s)\left\{\frac{2\pi\sigma_p c^2}{E'} + \frac{M\pi}{J_z E'}\left[2rc^2 - \frac{c^4}{4r} + \frac{c^6}{96r^3} - \frac{c^8}{4608r^5}\right]\right\} \tag{11}$$

This method proposed to avoid an overestimation of the bending stress, which would be against the underestimating philosophy of conservative leak rate computation within LBB assessment.

2.2.4. LBB.ENG2 method

The LBB.ENG2 method [5] considers elastic-plastic material properties and a combination of pressure load with a bending moment. It shares the elastic COD with the GE/EPRI approach (see Section 2.2.1), but the plastic COD is computed differently (while also relying on the Ramberg-Osgood plasticity description). Approach [7] is applied in the following.

$$COD_{pl} = \frac{\alpha\epsilon_0\left(\frac{\sigma_T}{\sigma_0}\right)^{n-1}}{1 - \frac{\gamma}{\pi} - \frac{2}{\pi}\sin^{-1}\frac{\sin\gamma}{2}} + r_m\left(1 + \sin\frac{\gamma}{2}\right)\phi_{pl} \tag{12}$$

In this formulation, ϕ_{pl} is the plastic rotation in the presence of a crack.

$$\phi_{pl} = \left[\frac{\pi}{4\cos\frac{\gamma}{2} - 2\sin\gamma} \right]^{n-1} \left(\frac{2\sqrt{\pi}\ \Gamma\left(\frac{2+n}{2}\right)}{4\ \Gamma\left(\frac{3+n}{2}\right)} \right)^n \frac{\alpha\ I_B(\gamma)}{E\sigma_0^{n-1}} \left(\frac{M}{\pi r_m^2 t} \right)^n \qquad (13)$$

The integral I_B can be computed analytically with the scheme of [7], Appendix A.

$$I_B(\gamma) = 2\gamma^2 \left[1 + 8\left(\frac{\gamma}{\pi}\right)^{\frac{3}{2}} I_{B1} + \left(\frac{\gamma}{\pi}\right)^3 (I_{B2} + I_{B3}) \right] \qquad (14)$$

With six additional auxiliary quantities A_B, B_B, C_B, I_{B1}, I_{B2} and I_{B3}, the rotation can be computed explicitly.

$$
\begin{aligned}
A_B &= \sum_{j=0}^{3} a_{B,j} \left(\frac{r_m}{t}\right)^j \\[2mm]
B_B &= \sum_{j=0}^{3} b_{B,j} \left(\frac{r_m}{t}\right)^j \\[2mm]
C_B &= \sum_{j=0}^{3} c_{B,j} \left(\frac{r_m}{t}\right)^j \\[2mm]
I_{B1} &= \frac{A_B}{7} + \frac{B_B}{9}\frac{\gamma}{\pi} + \frac{C_B}{11}\left(\frac{\gamma}{\pi}\right)^2 \\[2mm]
I_{B2} &= \frac{2\ A_B^2}{5} + \frac{2\ A_B B_B}{3}\frac{\gamma}{\pi} + \frac{4A_B C_B + 2B_B^2}{7}\left(\frac{\gamma}{\pi}\right)^2 \\[2mm]
I_{B3} &= \frac{B_B C_B}{2}\left(\frac{\gamma}{\pi}\right)^3 + \frac{2C_B^2}{9}\left(\frac{\gamma}{\pi}\right)^4
\end{aligned}
\qquad (15)
$$

The numerical values of the polynomial coefficients of A_B, B_B and C_B in this approach are summarised in Table 2.3.

Table 2.3. Coefficients for the LBB.ENG2 method, from [7]

j	0	1	2	3
$a_{B,j}$	-3.26543	1.52784	-0.072698	0.0016011
$b_{B,j}$	11.36322	-3.91412	0.18619	-0.004099
$c_{B,j}$	-3.18609	3.84763	-0.18304	0.00403

This formulation of the LBB.ENG2 method (note that I_B differs in [5]) is a closed form for the combination of pressure and bending loads for Ramberg-Osgood plasticity.

2.2.5. Tada-Paris method

The Tada-Paris method [8] allows computing the COD under pressure load. The computed areas are purely elastic.

$$A = \frac{2\pi r_m t\ \sigma}{E'}\ G\left(\lambda_{TP} = \frac{c}{\sqrt{r_m t}}\right) \qquad (16)$$

For circumferential cracks, the stress is obtained by $\sigma^{\text{circ}} = p r_m / (2t)$, and the function $G(\lambda_{TP})$ is computed as follows.

$$G^{\text{circ}}(\lambda_{TP}) = \begin{cases} \lambda_{TP}^2 + 0.16\,\lambda_{TP}^4 & 0 < \lambda_{TP} \le 1 \\ 0.02 + 0.81\,\lambda_{TP}^2 + 0.3\,\lambda_{TP}^3 + 0.03\,\lambda_{TP}^4 & 1 \le \lambda_{TP} \le 5 \end{cases} \tag{17}$$

For axial cracks the stress is $\sigma^{\text{axial}} = 2\,\sigma^{\text{circ}}$, and the G-function is defined as follows.

$$G^{\text{axial}}(\lambda_{TP}) = \begin{cases} \lambda_{TP}^2 + 0.625\,\lambda_{TP}^4 & 0 < \lambda_{TP} \le 1 \\ 0.14 + 0.36\,\lambda_{TP}^2 + 0.72\,\lambda_{TP}^3 + 0.405\,\lambda_{TP}^4 & 1 \le \lambda_{TP} \le 5 \end{cases} \tag{18}$$

Note that the formulas of the stresses can be generalised as shown in equation (2).

2.2.6. WRC method

The method proposed by the Welding Research Council (WRC) [9] for computing starts also from a crack in an infinite plate under homogeneous load and corrections. The COA is given as follows.

$$A^{\text{ID/OD}} = A_{\text{plate}}^{\text{elastic}} \left[\sum_i \sigma_i H_i^{\text{ID/OD}} \left(\frac{r_i}{t}, \lambda_s \right) \right] \gamma(L_r) \tag{19}$$

The elastic plate solution under uniaxial load is similar to equation (9), but the uncorrected elastic modulus E is used instead of E'.

$$A_{\text{plate}}^{\text{elastic}} = 2\,\pi\,\frac{\sigma}{E}\,c^2 \tag{20}$$

The solution is mapped to a pipe by multiplying it with a H-function. This H-function depends on the actual load, the r_i/t-ratio, and the shell parameter λ. This approach also allows to give separate H-functions for the inner and outer side (ID/OD) of the pipe wall. For circumferential cracks, tables of H are given in [9] for three loads (constant load, linear stress variation through the wall, and bending moment), for seven r_i/t-ratios, nine λ_s-values, and for the inner and outer side. For axial cracks, the load states are constant load, linear stress variation and bending moment.

The last term is the plastic correction factor, which corrects the elastic approach and also considers biaxiality effects.

$$\gamma(L_r) = 1.008 - 0.33015\,L_r^2 + 5.53696\,L_r^4 - 3.96974\,L_r^6 + 2.00844\,L_r^8 \tag{21}$$

The load ratio L_r is computed by consideration of the biaxiality influence factor and the material's yield stress σ_Y.

$$L_r = F\left(B = \frac{\sigma_\parallel}{\sigma_\perp} \right) \frac{\sigma_\perp}{\sigma_Y} \tag{22}$$

The symbol $\sigma_\perp$ denotes the stress component perpendicular to the crack face, i.e. the crack opening stress, and $\sigma_\parallel$ the orthogonal stress tensor component. $F(B)$ is given for values of B between 0 and 2 in [9].

2.2.7. xLPR COD module

The circumferential crack xLPR COD module that provides elastic-plastic COD solutions is based on [23] and [24] for use in the Extremely Low Probability of Rupture (xLPR) programme [34]. It provides elastic-plastic COD solutions for circumferential cracks for simultaneously applied axial and crack face pressure with an applied bending moment. The axial crack COD module is based on [36] and [37].

2.3. Leak morphology and flow resistance consideration

Classically, the leak morphology (surface structure characteristics) is considered to enter the leak computation via flow resistance. According to custom surface characterisation approaches, the flow resistance has several contributions: form loss associated with the entrance into the leak channel, frictional pressure losses due to flow along the rough crack faces, as well as pressure losses due to bends in the flow path and effects of cross section changes. A total flow resistance can be defined as the sum of the individual parts.

$$\zeta_{\text{total}} = \zeta_{\text{in}} + \zeta_{\text{friction}} + \zeta_{\text{bends}} + \zeta_{\text{cross-section}} \tag{23}$$

Since many leak flow models (see Section 2.4) are unidimensional and have origins in pipe flow, the concepts are very similar to engineering approaches for piping system analysis.

2.3.1. Inlet pressure loss

The entrance resistance ζ_{in} is associated with form pressure loss at the entrance into the leak. This is related to the flow along the more or less sharp edge and the reduction of the effective cross section via the contraction of the flow (vena contracta). Another characterisation of this is the discharge coefficient c_d, which is the cross section fraction relative to the full leak cross section. Based on incompressible flow, ζ_{in} and c_d are often related to each other as follows.

$$\zeta_{\text{in}} = \frac{1}{c_d^2} - 1 \tag{24}$$

For crack-like leaks, the value of the discharge coefficient typically ranges from 0.62 to 0.95 [11]; a value of $\zeta_{in} = 0.5$ is also a common choice [10][20].

2.3.2. Roughness and morphology parameters

The surface of a crack-like leak created by a damage mechanism is irregular and rough, while the roughness of a known leak geometry can be measured (the roughness parameter R_z is often used).

When the COD is varying, the irregularities in the crack faces can either play a role as bendings in the flow path, or as surface roughness. This feature is considered by the improved morphology model [14]. This approach defines global values of roughness, and

if the two crack faces are close enough to each other, this global roughness plays the role of bendings, while the local roughness is the effective surface roughness μ_{eff}.

$$\mu_{\text{eff}} = \begin{cases} \mu_L & \dfrac{COD}{\mu_G} < 0.1 \\ \mu_L + \dfrac{\mu_G - \mu_L}{9.9}\left(\dfrac{COD}{\mu_G} - 0.1\right) & 0.1 < \dfrac{COD}{\mu_G} < 10 \\ \mu_G & \dfrac{COD}{\mu_G} > 10 \end{cases} \qquad (25)$$

The number of turns is computed analogously as an effective number n_{eff} depending on the COD, a local number n_L and a global number n_G.

$$n_{\text{eff}} = \begin{cases} n_L & \dfrac{COD}{\mu_G} < 0.1 \\ n_L - \dfrac{n_L}{11}\left(\dfrac{COD}{\mu_G} - 0.1\right) & 0.1 < \dfrac{COD}{\mu_G} < 10 \\ 0.1\,n_L & \dfrac{COD}{\mu_G} > 10 \end{cases} \qquad (26)$$

As cracks found in service are usually not ideally straight, a correction parameter K characterising the actual leak flow path divided by the pipe wall thickness is introduced.

$$K_{\text{eff}} = \begin{cases} K_{G+L} & \dfrac{COD}{\mu_G} < 0.1 \\ K_{G+L} - \dfrac{K_{G+L} - K_G}{9.9}\left(\dfrac{COD}{\mu_G} - 0.1\right) & 0.1 < \dfrac{COD}{\mu_G} < 10 \\ K_G & \dfrac{COD}{\mu_G} > 10 \end{cases} \qquad (27)$$

The morphology parameters μ_L, μ_G, n_L, K_{G+L} and K_G are specific to a damage mechanism, and recommendations for specific parameters exist.

2.3.3. Friction factor

The frictional pressure loss is an important part for many applications, and also this origin dates back to the analysis of rough pipes. The frictional resistance is proportional to the length of the leak channel $L = K_{eff}t$, with the Darcy-Weissbach friction factor λ.

$$\zeta_{\text{frcition}} = \int_0^L \frac{\lambda(z)}{d_h(z)} dz \underset{const.}{\overset{\lambda, d_h}{=}} \frac{\lambda L}{d_h} \qquad (28)$$

The ratio L/d_h is the hydraulic relative length of the leak, where L is just the wall thickness in the simplest case.

Nikuradse

The classical relation for λ was derived for sand-rough pipes in the form of the Nikuradse friction relation [16].

$$\lambda = \left[3.39 \log_{10}\left(2\,\frac{d_h}{2\,R_z} \right) - 0.866 \right]^{-2} \tag{29}$$

The Darcy-Weissbach friction factor λ depends in this model on the roughness $R_z = \mu_{\text{eff}}$, a natural generalisation of the parameter k of sand grain sizes in the analysis of rough pipes.

John et al.

The approach for the relation between the friction factor and the surface roughness of the flow channel proposed by [10] is based on the evaluation of laboratory tests with rough slit samples and fatigue cracks.

$$\lambda = \left[2 \log_{10}\left(\frac{d_h}{2\,R_z} \right) + 1.74 \right]^{-2} \tag{30}$$

This friction relation has a steeper increase of the friction factor in the regime of narrow cracks than the Nikuradse Karman friction factor – note that it diverges for very narrow cracks, which in turn leads to an infinite flow resistance.

Paul et al.

The approach proposed in [11] uses the formula of John et al. [10] for narrow slits, and the Nikuradse relation for wider slits.

$$\lambda = \begin{cases} \lambda_{\text{Nikuradse}} & \text{if } \dfrac{d_h}{2\,R_z} \geq 50 \\[2mm] \lambda_{\text{John}} & \text{if } \dfrac{d_h}{2\,R_z} < 50 \end{cases} \tag{31}$$

This considers the fact that John et al. focused on narrow, rough slits, and their relation is less accurate for wide smooth geometries, where the classical results from pipe flow are more representative. Instead of an inverse relative roughness value $d_h/2R_z$ of 50 as the border between the two definitions, a value of 55.48 might also be imposed.

KTA 3206

The safety standard KTA 3206 [20] is guided by the philosophy of a conservative underestimation of the leakage rate. One key element of this approach is the conservative overestimation of the friction factor. The safety standard proposes its own friction factor relation for this purpose.

$$\lambda = \min\left(2, \frac{1}{2}\left[\log_{10}\left(\frac{3}{2}\frac{d_h}{2\,R_z} \right) \right]^{-2} \right) \tag{32}$$

This relation is valid for $d_h/2R_z > 1$. In contrast to the other friction factor relations, it is not a best-estimate approach, but can be used for the underprediction of the leak rate.

2.3.4. Measurement of integral flow resistance

Instead of deriving the friction factor of a laboratory test from the roughness by an empirical relation, it is also possible to measure the single-phase flow resistance. This measured flow resistance value can be assumed in the two-phase flow computations as well. Of course,

this procedure is restricted to the laboratory tests where the flow resistance was measured. According to the Bernoulli equation for an incompressible fluid of density ρ, the flow resistance ζ of a leak is related to the mass flow rate m at a defined pressure drop Δp.

$$\zeta = 2 \, \rho \, \Delta p \, \frac{COA^2}{\dot{m}^2} - 1 \tag{33}$$

COA denotes the cross section of the leak. The use of the single-phase flow resistance for two-phase leak flow is a way to reduce uncertainties in the leak assessment for laboratory tests.

2.4. Fluid mechanical modelling

After the determination of the leak geometry and the characterisation of the resistance due to the morphology, the fluid mechanical analysis is required to predict the mass flow rate m. For single-phase incompressible fluid flow (such as cold water, in good approximation), the flow rate through a cross section A can be computed using the Bernoulli equation.

$$\dot{m} = A \sqrt{\frac{2\rho(p_0 - p_{ext})}{1 + \zeta}} \tag{34}$$

In this study, some of the fluid tests are in this regime, but others (and possibly the most relevant) have hot pressurised water in the stagnation volume, where evaporation would occur. This violates the assumption of single-phase incompressible fluid and gives rise to the more complex models discussed in the following subsections.

These models are defined with a common nomenclature, where the mass density is denoted as ρ, the specific enthalpy is denoted as h, the specific volume as $v = 1/\rho$, and the specific entropy as s. The indices (like ρ_L, ρ_G) indicate the liquid in gaseous/vapour phase, respectively. Mixture quantities also occur, which use the void fraction α.

$$\bar{\rho} = \rho_L(1 - \alpha) + \rho_G \alpha \tag{35}$$

The (local) velocity is denoted as w. It is also convenient to define the mass flux density $G = \dot{m}/A$, which is also related to the velocity by $w = G/\rho$.

2.4.1. Abdollahian-Chexal model

The Abdollahian-Chexal model [15] is constructed as an approximative scheme avoiding numerical complications of iterative solutions. It is based on the assumption that the pressure drops to the saturation pressure, and resistance occurs due to the friction factor λ and entrance losses described by the discharge coefficient c_d.

$$\dot{m} = A \sqrt{\frac{2\rho(p_0 - p_{sat})}{v_m + v_m \lambda \frac{L}{d_h} + \frac{v_0}{c_d^2}}} \tag{36}$$

While v_0 denotes the specific volume upstream, the average specific volume v_m is based on the mean pressure $\bar{p} = [p_0 + p_{sat}(T_0)]/2$.

$$v_m = v_L(\bar{p}) + \alpha(\bar{p}) \left[v_G(\bar{p}) - v_L(\bar{p})\right] \tag{37}$$

The remaining parameter, the quality α at the average pressure $\bar{p}$, is computed assuming the isenthalpic changes, $\alpha(\bar{p}) = [h_0 - h_F(\bar{p})]/h_{FG}(\bar{p})$. This model is an iteration-free approximation based on the estimate of the exit pressure and a simple correction of the fluid density.

2.4.2. ATHLET-CDR model

Thermal-hydraulical system codes are possible computation tools for two-phase flow through slit-like leaks. Within this benchmark, the thermal-hydraulic code ATHLET with the included critical discharge rate (CDR) model [1] was applied. The CDR model is based on the evolution of the mass fraction of liquid and vapour phase with time t and flow path distance z. Together with the mixture energy and the mixture momentum, four equations define the CDR model (gravitational influences are neglected in the following).

$$\frac{d}{dt}(\rho_L(1-\alpha)A) + \frac{d}{dz}(\rho_L(1-\alpha)wA) = -\psi A \tag{38}$$

$$\frac{d}{dt}(\rho_G \alpha A) + \frac{d}{dz}(\rho_G \alpha w A) = \psi A \tag{39}$$

$$\frac{d}{dt}\left(\left(\overline{\rho h} + \frac{\rho}{2}w^2 - p\right)A\right) + p\frac{dA}{dt} + \frac{d}{dz}\left(\left(\overline{\rho h}\, w + \frac{\rho}{2}w^3 - p\right)A\right) = q^* A \tag{40}$$

$$\frac{d}{dt}(\bar{\rho}wA) + \frac{d}{dz}\left((p + \bar{\rho}w^2)A\right) - p\frac{dA}{dz} = -R^* A \tag{41}$$

In this equation system, R^* denotes the (friction-influenced) pressure loss per length, and q^* the power density relevant for the energy balance, and ψ the mass transfer rate between the states. For stationary conditions, the time-dependence can be dropped out, and the equation system can be written as a matrix equation.

$$\hat{C}\frac{d}{dz}\boldsymbol{u} = \boldsymbol{r} \tag{42}$$

The 4-vector $\boldsymbol{u}$ reads (p, T, w, α). In the case of critical flow, the criticality at the exit plane implies a boundary condition at $z = L$ for the eigenvalues λ_i^C of the system.

$$\exists j\ \lambda_j^C = 0 \wedge \lambda_i^C > 0\ \forall\ i \neq j \tag{43}$$

With this boundary condition, the matrix equation (42) can be solved numerically. It is worth noting that the CDR model is a complex and accurate model, but relies intrinsically on critical flow conditions – it is not constructed for the (often simpler) case of subcritical

flow, where an appropriate continuation has to be chosen (e.g. the Bernoulli equation for cold water flow).

2.4.3. Burnell model

The Burnell model [12][18] is a model for short orifices for leak flow, which is the reason why it assumes only a very small amount of evaporation. The mechanism which is supposed to prevent evaporation is the surface tension. The model is formulated as a single-phase flow equation of a fluid of density ρ, undergoing a pressure drop from the upstream condition to a value $(1 - C)p_{sat}$, slightly below the saturation pressure.

$$\dot{m} = c_d\, A\, \sqrt{2\rho[p_0 - (1 - C)p_{sat}]} \tag{44}$$

The coefficient C is determined for one saturation pressure and corrected by a simple relation for the variation of the surface tension.

$$C(p_{sat}) = K \frac{\gamma(p_{sat})}{\gamma(p_{sat}^{ref})} \tag{45}$$

The values of $K = 0.264$ for $p_{sat}^{ref} = 175$ psia and $K = 0.284$ for $p_{sat}^{ref} = 200$ psia are used in [18].

2.4.4. Henry-Fauske model

A classical approach for the computation of evaporating liquid flow is the formulation of Henry and Fauske [13][38]. It is a class of models that share a common basis, as discussed in [11][14][15]; the notable extension to the original formulation is the consideration of friction effects. The key equation for the mass flow rate is the critical mass flow rate G.

$$G = \frac{1}{\dfrac{xv_G}{\gamma p_c} - (v_G - v_L)N\dfrac{dx_E}{dp}} \tag{46}$$

This model uses a phenomenological vapour generation rate, representing the delayed evaporation in a fast-flowing fluid discharge, while the equilibrium steam quality x_E can be derived from the stagnation entropy s_0 and the specific entropy of both phases.

$$x_E = \frac{s_0 - s_L}{s_G - s_L} \tag{47}$$

The factor N denotes the correction factor for the non-equilibrium evaporation, which depends on the steam quality x_E itself.

$$N(x_E) = \begin{cases} 20\, x_E & \text{if } x_E < 0.05 \\ 1 \text{ or } 1.2 & \text{if } x_E \geq 0.05 \end{cases} \tag{48}$$

The pressure at the exit at critical mass flux p_c is a result of different contributions to the pressure drop $\Delta p_{total} = (p_0 - p_{exit})$ and is itself a function of the mass flow rate G.

$$p_c = p_0 - \Delta p_{\text{in}} - \Delta p_{\text{friction}} - \Delta p_{\text{acc}} - \Delta p_{\text{area}} - \Delta p_{tort} \tag{49}$$

The term Δp_{in} is the pressure loss at the entrance in the leak which is associated with entrance effects. It is expressed in terms of the discharge coefficient c_d, and depends on the mass flux through the entrance (where the density is ρ_0 and the cross section area is A_0).

$$\Delta p_{\text{in}} = \frac{\dot{m}^2}{A_{in}^2 \rho_0} \frac{1}{2 c_d^2} = \frac{G_{exit}^2}{2 c_d \rho_0} \frac{A_{exit}^2}{A_0^2} \tag{50}$$

The frictional pressure drop $\Delta p_{\text{friction}}$ is a function of the friction factor λ (see equation (28)), which simplifies for the assumption of constant values of G, x and v_G (using averages).

$$\Delta p_{\text{friction}} = \lambda \left(\frac{L}{d_h} - 12 \right) \frac{G^2}{2} [(1-x)v_L + xv_G] \tag{51}$$

Alternatively, and especially in case of variations of the cross section A along the flow path, the frictional pressure loss can also be computed by the following expression.

$$\Delta p_{\text{friction}} = \lambda \frac{G^2}{2} \frac{A_{exit}^2}{A_{evap}^2} \left[6 v_0 + \left(\frac{L}{d_h} - 12 \right) [(1-x)v_L + xv_G] \right] \tag{52}$$

In this equation, x denotes the isenthalpic vapour quality at the average pressure. In the case of short leaks with $L/d_h < 12$, the frictional pressure drop is instead computed by the following equation.

$$\Delta p_{\text{friction}} = \lambda \frac{G^2}{2} \frac{A_{exit}^2}{A_{evap} A_0} 12 \, \rho_0 \tag{53}$$

The acceleration pressure drop Δp_{acc} is associated with the acceleration of the fluid due to the decreasing density induced by the phase transition (vapourisation).

$$\Delta p_{\text{acc}} = G_c^2 \frac{A_{exit}}{A_{evap}} \frac{A_{exit}}{A_0} \left[\left(1 - x_{exit}^{(h)} \right) v_{thr,sat,L} + x_{exit}^{(h)} v_{thr,sat,G} - v_0 \right] \tag{54}$$

In this expression, $x_{exit}^{(h)}$ denotes the isenthalpic equilibrium vapour quality at the crack exit plane, and $v_{thr,sat,L}$ and $v_{thr,sat,G}$ denote the specific volume at the throat of saturated liquid and vapour, respectively. Under certain simplifying assumptions, and a constant cross section, the pressure drop can also be computed as follows.

$$\Delta p_{\text{acc}} = G^2 x_c (v_G - v_L) \tag{55}$$

For cross section changes (from the interior side A_i to the exterior side A_e), the additional term Δp_{area} arises.

$$\Delta p_{\text{area}} = \frac{G_{\text{exit}}^2}{2} \left[v_L \left(1 - \frac{A_e^2}{A_i^2} \right) + x(v_G - v_L) \left(1 - \frac{A_c^2}{A_i^2} \right) \right] \tag{56}$$

An alternative formulation is given in terms of the interpolated area at the start of evaporation $z = 12d_h$, which is denoted A_{evap}.

$$\Delta p_{\text{area}} = \frac{G_{\text{exit}}^2 \, v_0}{2} \left[\frac{A_{exit}^2}{A_{evap}^2} - \frac{A_{exit}^2}{A_0^2} \right] + \frac{G_{\text{exit}}^2}{2} [1 - x \, v_F(\bar{p}) + x v_G(\bar{p})][1 - \frac{A_{exit}^2}{A_{evap}^2}] \tag{57}$$

In the latter equation $\bar{p}$ denotes the average pressure between the section past the entrance and the exit. The steam quality to be used here is the isenthalpic vapour quality at this average pressure, determined by the following equation (in which Δh is the latent heat of evaporation).

$$x^{(h)} = \frac{h_L(p_0, T_0) - h_{F,sat}(\bar{p})}{\Delta h(\bar{p})} \tag{58}$$

The tortuosity pressure loss Δp_{tort} is a function of the crack face morphology, more precisely of the number of turns n_t. This number can also be given in terms of the turn density per length η_t, where $n_t = \eta_t L_{eff}$.

$$\Delta p_{\text{tort}} = \frac{G^2}{2} n_t \frac{A_{exit}}{A_{evap}} [1 - x \, v_F(\bar{p}) + x v_G(\bar{p})] \tag{59}$$

The combination of equations (46) and (49) has to be solved, either iteratively or by numerical root finding, in order to find the critical pressure p_c and the CDR G_c. Compared to other approaches, the solution of a differential equation is avoided by the averaging strategy in the contributions to the pressure drop.

2.4.5. Metastable jet model

The metastable jet model [17] is an approach for the flow through short orifices, where no evaporation occurs and a jet of metastable liquid water forms. It is a single-phase compressible fluid equation without consideration of friction.

$$\dot{m} = A \, c_d \, \rho_{ML}(p_{ext}) \sqrt{2[h(p_0) - h_{ML}(p_{ext})]} \tag{60}$$

In this equation, h_{ML} and ρ_{ML} denote the specific enthalpy of the metastable fluid and its mass density, respectively.

2.4.6. Modified Bernoulli model or Zaloudek model

The modified Bernoulli equation is a simple estimation scheme for leak flow rates at sufficient subcooling [18][19][20]. This approach is based on the observation that the thermodynamic conditions at the exit plane are on the saturation line. A guess for this saturation condition is the saturation pressure at the stagnation temperature $p_{sat}(T_0)$. When the density reduction is neglected, the mass flow rate can be written as a Bernoulli equation (like equation (34)) with modified exterior pressure.

$$\dot{m} = A \sqrt{\frac{2\rho(p_0 - p_{sat})}{1 + \zeta}} \tag{61}$$

This simplification works very well for large subcooling (i.e. large pressure or temperature difference to saturation conditions) but fails for small subcooling (where it is very underpredicting) and cold water conditions (where the saturation pressure is below the exterior pressure).

2.4.7. Pana model

The Pana model [21] describes the unidimensional flow through a leak by modelling the flow between defined check points. This description concentrates on the subcooled stagnation conditions. The check points are indicated by the index '1' for a location downstream of the entrance region, and the index '2' by the exit plane. The mass flow to location '1' is modelled by the Moody model by an isentropic pressure drop from p_0 to p_1.

$$G_{\text{Moody}}(k, p_1) = \sqrt{\frac{2\,(h_0 - (1-x)h_L - x\,h_G)}{[x\,v_G + k(1-x)v_F]^2 \left(x + \dfrac{1-x}{k^2}\right)}} \tag{62}$$

The thermodynamic properties are to be taken at location '1': the parameter k is used for maximisation, $G(p_1) = \max_k G(k, p_1)$. The pressure drop from p_1 to p_2 is governed by the flow resistance ζ, which is an implicit relation of $p_2(p_1)$.

$$\zeta = -2 \int_{p_1}^{p_2} \frac{1 + G^2 \left(\dfrac{\partial v(p)}{\partial p}\right)_s}{G^2 v(p)}\, dp \tag{63}$$

The Pana model is solved by maximising G_{Moody} by the parameter k, and by maximising this result by the variation of p_1, under the side condition of $p_2(p_1) > p_{ex}$.

$$G_{\text{Pana}}(p_0, s_0, \zeta, p_{ex}) = \max_{p_1} \left[\max_k G_{\text{Moody}}(k, p_1)\right]_{p_2(p_1) > p_{ex}} \tag{64}$$

This approach can be used for critical mass flow as well as for subcritical discharge rates since the side condition acts directly in the iteration scheme. It is possible to solve equation (64) numerically with two nested optimisers.

2.5. Software

The previous sections show that the different parts of leak flow rate prediction require numerical computation of at least moderate complexity, and thus the methods were implemented in computer programs for reliable application of the approaches. This section presents the different software tools that were used in the benchmark activity.

2.5.1. ANSYS CFX

ANSYS-CFX is a general purpose commercial computational fluid dynamic software. It is used to simulate the behaviour of systems involving fluid flow, heat transfer and other related physical processes. ANSYS-CFX works by solving the equations of fluid flow over

a region of interest, with specified conditions on the boundary of that region. ANSYS CFX is stemmed from the programme CFX-4, (formerly known as Flow3D) which was originally developed by the United Kingdom Atomic Energy Authority (AEA). In 2003, just prior to the release of CFX-5.6, ANSYS Inc. of Canonsburg, PA, acquired the CFX division from AEA Technology.

The set of Navier-Stokes equations are used to describe the processes of momentum, heat and mass transfer. These partial differential equations are discretised and solved numerically. A single-phase or multiphase approach is used for the leak rate analysis. Detailed physical models can be referred to the ANSYS CFX theory manual [22]. The finite volume technique is adopted in ANSYS CFX. In this technique, the region of interest is divided into small sub-regions, so-called control volumes. The equations are discretised and solved iteratively for each control volume. As a result, an approximation of the value of each variable at specific points throughout the domain can be obtained. In this way, one derives a full picture of the behaviour of the flow. Additional code features include:

- steady-state and transient flows;

- laminar and turbulent flows;

- subsonic, transonic and supersonic flows;

- heat transfer and thermal radiation;

- buoyancy;

- non-Newtonian flows;

- transport of non-reacting scalar components;

- multiphase flows;

- combustion;

- flows in multiple frames of reference;

- particle tracking.

Full licence of the software needs to be purchased from ANSYS Inc. For purpose of study, the software can be downloaded on the ANSYS website with a free student licence for a problem size limit of 512K cells/nodes. ANSYS CFX is in compliance with 10CFR50, Appendix B, and has been approved for use at Candu Energy Inc.

2.5.2. ExcelSQUIRT

ExcelSQUIRT is a derivative of the SQUIRT software (see Section 2.5.8); both are owned and maintained by Battelle. It provides leak rate computation functionalities by separate tabs of an Excel spreadsheet.

The LeakRate tab calculates the leak rate for a given pipe geometry and set of thermal-hydraulic conditions (temperature and pressure). The CrackSize tab calculates the leakage crack size for a prescribed leakage detection limit, pipe geometry, loading conditions (moment and pressure), and thermal-hydraulic conditions. The crack type (e.g. corrosion fatigue [CF], intergranular stress corrosion cracking [IGSCC], primary water stress corrosion cracking [PWSCC]) and crack shape (rectangle, diamond, elliptical) are defined on the Info tab of the spreadsheet.

The Leak Rate code used in the software is that which is used in the latest version of Pro-LOCA. It is derived from Version 2.1.3 of SQUIRT with some modification to improve convergence. The COD calculations are based on the Pro-LOCA version of the COD

routine which was updated to improve the COD calculation under combined bending and tension. Details of this model can be found in [23], [24] and [25].

2.5.3. LeakH

The code LeakH was developed by ÚJV. Its main purpose is to be implemented into BASLBB code performing automatic LBB evaluation. The code is also used for evaluating effects induced by a postulated pipe break.

The mathematical model used in the LeakH code consists of few simple thermodynamic laws. One of the most important parts of the code are tables of water and steam properties. The tables contain a set of equations precisely describing the properties of water and steam according to [26].

Entrance parameters of leaking coolant can be up to 100 MPa and 800°C. These values are within the validity of the tables of water and steam properties. The model includes entrance loss pressure, crack surface friction influence and changes of crack areas through the wall thickness. Changes of flow direction in the crack of about 45° and 90° are also considered. Calculations are performed using the following simplifying assumptions:

1. Flow is assumed to be one-dimensional.
2. In two-phase region the flow is considered to be homogeneous, i.e. slip between phases is not considered.
3. Heat exchange with the environment is not considered.
4. Changes of area in the direction of flow are linear.
5. Flow is in steady state and input parameters do not vary in time.

The code was prepared in agreement with a quality assurance (QA), and its validation was performed based on comparison with PICEP (see Section 2.5.6) and measurement on an experimental device (pipe about 100 mm, primary circuit condition, artificial crack). Detailed information can be found in the code's user manual.

The code is available in ÚJV. It can be sold in this form based on negotiation with the customer (typically as a subroutine to be implemented into another code). It was sold to the Ignalina Nuclear Power Plant.

2.5.4. LEAPOR

LEAPOR (Leak Analysis of Piping – Oak Ridge) was developed at Oak Ridge National Laboratory (ORNL) as the module for performing leak rate calculations in the xLPR (Extremely Low Probability of Rupture) Version 2 (V2) probabilistic fracture mechanics code [34], jointly developed by the US Nuclear Regulatory Commission (USNRC) and the Electric Power Research Institute (EPRI), Inc. LEAPOR was developed using the thermo-hydraulic models employed in the SQUIRT leak rate code (see Section 2.5.8) [11] [14]. LEAPOR employs a four-regime model that was originally developed under the MERIT (Maximising Enhancements in Risk-Informed Technology) Programme [35] to represent the spectrum of leak rates from tight cracks to orifice flow, where the boundaries of each regime are defined by a ratio of the effective flow path length to the hydraulic diameter.

As one of a number of modules in the xLPR project, the LEAPOR code was required to be a Software Quality Assurance (SQA) auditable application, fulfilling the software work-practice requirements of ASME NQA 1-2008 (including Addenda 2009) Quality Assurance Requirements for Nuclear Facility Applications. The code structure must be designed to be maintainable for current and future needs. "Code maintainability" refers to

how easily a software system can be changed to add new features, modify existing features, find and fix bugs, and/or improve performance. Additionally, the xLPR Project SQA plan stated that the "source code components (source code and documentation) must be evaluated for correctness, consistency, completeness, accuracy, readability, and testability". These requirements were driven by the need to provide proven mechanisms for managing increasing and evolving complexity throughout the life cycle of the application. Further details about the theory and modelling decisions in LEAPOR and validation with experimental data can be found in [39].

LEAPOR-SA has the same capabilities and uses the same code as LEAPOR and incorporates a Graphical User Interface (GUI) to facilitate standalone applications outside of xLPR V2. The LEAPOR-SA GUI was written by the NRC staff. It provides a user-friendly method of entering the necessary parameters needed to calculate leak rates using LEAPOR-SA. The GUI is programmed in Fortran. As shown in Figure 2.2, operation parameters (i.e. numerical values for geometry, pressure, and temperature), crack parameters (i.e. crack shape including ellipse, rectangular as well as diamond and crack surface toughness type containing IGSCC, PWSCC base metal and weld metal, CF and user input) and crack size are needed. A two-dimensional table of crack lengths (2c) and CODs will be generated and the leak rate will be calculated for each 2c-COD pair. Here the 2c values are at the mid-wall (MW) location and the crack is assumed to be ideal (i.e. the crack angle at the MW, inside diameter [ID], and outside diameter [OD] locations are equal). The COD at the ID and OD are assumed to be equal. Error checking is performed prior to the computation to ensure valid inputs have been entered.

Figure 2.2. User Interface of LEAPOR-SA
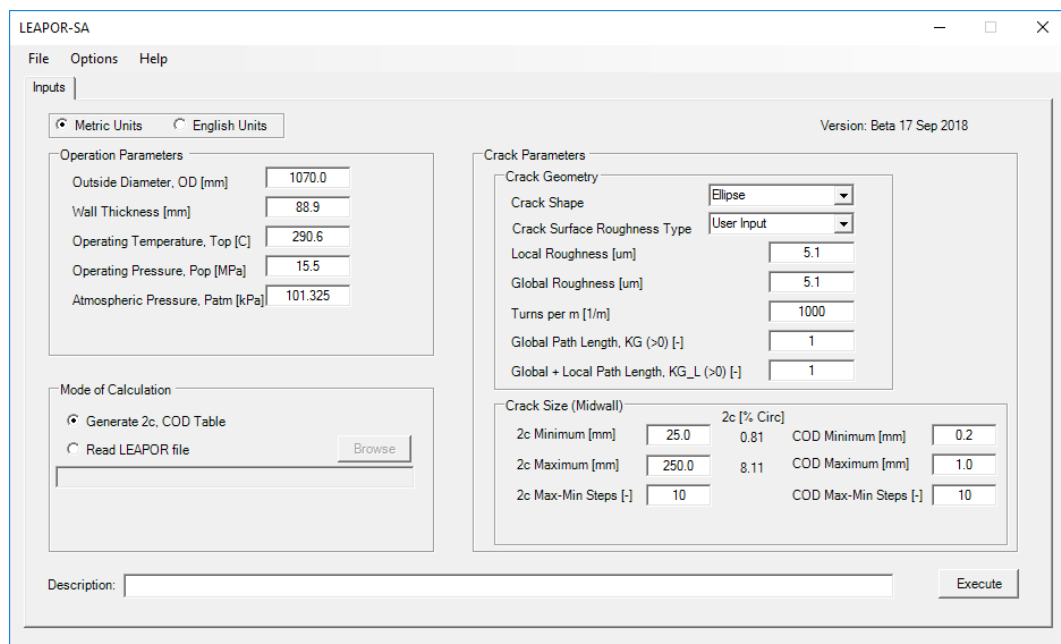
2.5.5. LOCI

The LOCI™ code is under development by OCI. LOCI™ is a new leakage code [40] being implemented within a modular and layered architectural software design that takes advantage of the object-oriented features and constructs available in the Fortran 2003

standard. Employing the LEAPOR[1] code (see Section 2.5.4) as a baseline prototype, LOCI™ includes, in addition to the *best-estimate* Henry-Fauske leakage-rate model (see Section 2.4.4) inherited from LEAPOR, four conservative leakage-rate models from the German safety standard KTA 3206 [20]. LOCI™ also includes three leakage-area COD models, specifically the GE/EPRI, KTA 3206 linear-elastic, and KTA 3206 elastic-plastic models.

In the context of an LBB assessment where emphasis is placed on the detection of small leakage rates, the distinction between *conservative* and *best-estimate* models becomes very important. This classification can provide guidance on where these models can be appropriately applied in terms of understanding margins and uncertainties. A *conservative* leakage-rate model is required to consistently underestimate the actual leakage rate and is typically applied in deterministic procedures, e.g. the deterministic approach in the German standard KTA 3206. A *best-estimate* leakage-rate model places greater emphasis on predictive accuracy. In a probabilistic framework, the model's estimated solutions can serve as a measure of central tendency (mean, median, or mode) for a prescribed statistical distribution characterising the uncertainties in the leakage-rate predictions. As noted above, LOCI™ provides both *best-estimate* and *conservative* leakage-area and leakage-rate models.

Also inherited from LEAPOR, LOCI™ contains a database of morphology parameters as a function of damage mechanism. The default values from this database can be considered in addition to user-input values in all analysis cases. A user interface for LOCI™ is currently under development by OCI (see Figure 2.3).

Figure 2.3. User Interface for LOCI™ (under development)
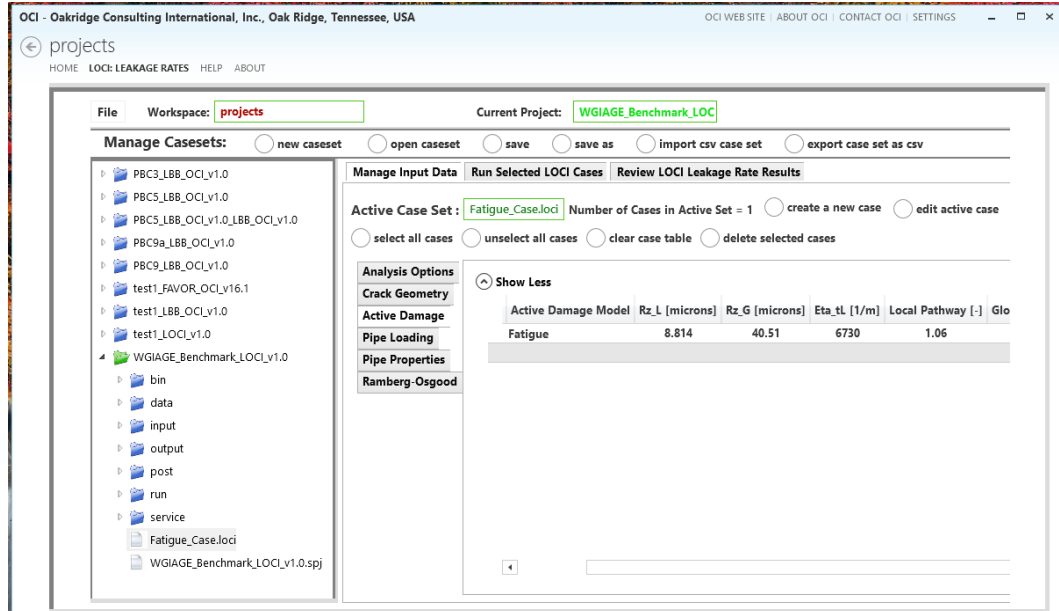
2.5.6. PICEP and SI-PICEP

The PICEP code is a computer code developed by EPRI for the leak rate assessment [27]. The PICEP calculates the flow through a crack in a pipe. PICEP uses the simplified

---

[1] Note that the OCI developer (Dr. Paul T. Williams) for LOCI™, before his retirement from ORNL, was the lead developer for the LEAPOR code.

engineering approach for elastic-plastic fracture analysis for finding the COD and COA. Fluid calculation options include single and two-phase flow as well as allowance for friction.

Later, Structural Integrity Associates, Inc. (SIA) developed the SI-PICEP code reflecting nuclear quality assurance from PICEP. The SI-PICEP is subject to formal quality assurance following SIA assurance procedures, which are in compliance with the requirements of 10CFR50, Appendix B, 10CFR21, and ANSI/ASME NQA-1-1989, 1994, and 2008/2009A and meets the applicable portions of ANSI N45.2.

2.5.7. SCALE

The SCALE code calculates crack opening parameters using the Tada-Paris model (see Section 2.2.5) for circumferential through-wall cracks and the Zahoor model (see Section 2.2.1) for axial through-wall cracks. It utilises a number of models for leak rate estimation. These models are of two categories. The Burnell (see Section 2.4.3) and Zaloudek (see Section 2.4.6) models are for subcooled flow leakage. These are homogeneous non-equilibrium models based on liquid-vapour surface tension and purely empirical. The model development is based on experimental verification and validation. These models do not consider any flow losses in terms of morphological roughness, though roughness is used in most leak flow estimation models. The losses can only be taken into account by means of a discharge coefficient. For critical flow, the throat pressure is not explicitly calculated. The other types of models are Henry's non-equilibrium and Homogenous Frozen (see Section 2.4.4). These are also homogenous non-equilibrium models; however, they consider critical flow based on stagnation and throat pressure. The relations between these two pressures (stagnation and throat) are through flow losses. Consequently, these models make provision for the consideration of morphological friction, form and turning losses. The SCALE code checks for the existence of the inertial and critical flow regimes.

2.5.8. SQUIRT

The SQUIRT (Seepage Quantification of Upsets In Reactor Tubes) computer code was developed as a tool for leak rate estimation, combining thermal-hydraulic and crack opening area models [11]. While the crack opening is based on the GE/EPRI method (see Section 2.2.1), the fluid-dynamical model is an implementation of the Henry-Fauske model (see Section 2.4.4). The friction factor approach is also carefully addressed; its implementation became a standard reference (described in Section 2.3.3.3).

SQUIRT led to the development of ExcelSQUIRT (see Section 2.5.2) and LEAPOR (see Section 2.5.4). It was widely distributed due to its availability through the NEA computer program services (CPS).

2.5.9. WinLeck

The WinLeck code was developed by GRS in the framework of several research projects since the mid-1990s. The code is designed for leak rate computation, mainly for water-steam-leaks, though it can also be used for gas/air leaks. The computational models in the code were validated by allowing the processing of many experimental data points and a systematic model validation matrix. The code is designed to support leak-before-break assessments.

Multiple models were implemented into WinLeck for the leak opening (GE/EPRI method, Section 2.2.1, GRS-PB method, Section 2.2.3, LBB.ENG2 method, Section 2.2.4, and others), the flow resistance, and the actual flow rate (Henry-Fauske model, Section 2.4.4,

Metastable jet model, Section 2.4.5, modified Bernoulli model, Section 2.4.6, Pana model, Section 2.4.7, and others). The programme structure allows for a combination of the different approaches and a comparison of the models' accuracy by simultaneous application on selected cases. This advantage allows to study specific model influences and also to identify uncertainties in reference test cases. A GUI (see Figure 2.4), a documentation, a validation report and tools for performing parameter studies are included.

Figure 2.4. Interface of the WinLeck code
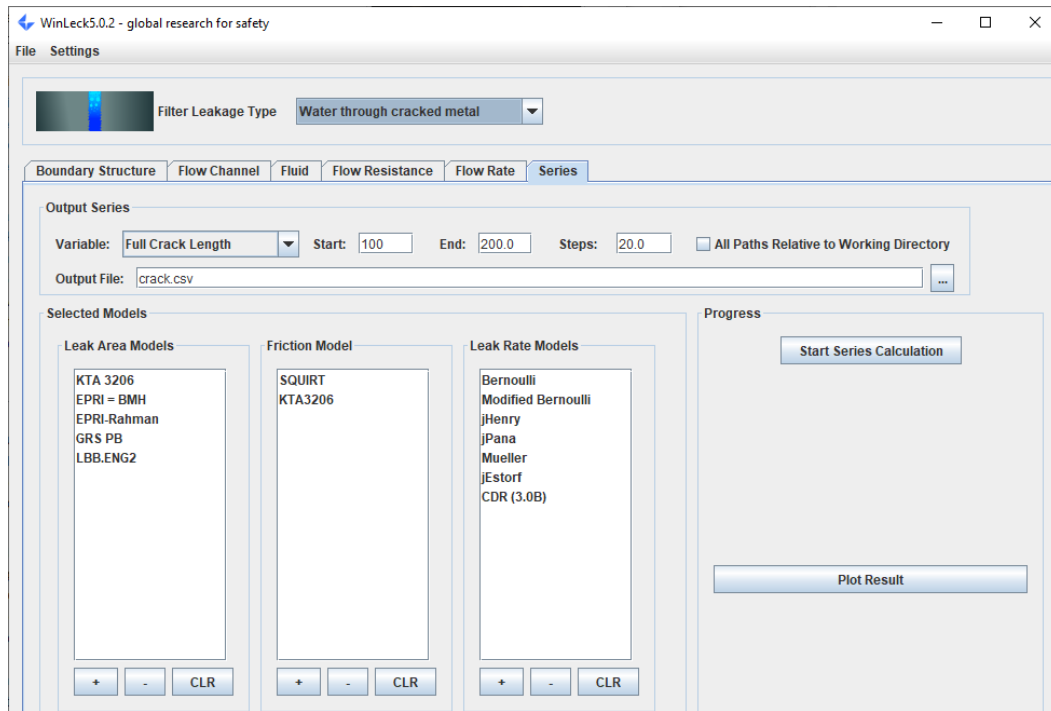
The WinLeck code is validated in numerous experiments and has a formal quality assurance procedure [28]. It is applied in research projects, case studies and LBB evaluations. The code can be made available to organisations on request without additional costs based on a licensing agreement.

2.6. Regulatory perspective

As leak rate computation is an essential part of LBB assessment, it is also subject to codes and standards. Within an LBB assessment, the leak rate computation is used to predict the flow through a postulated defect and to estimate the size of a defect that is reliably detected by leak monitoring devices. In this approach, the underestimation of the actual leak rate is conservative because a higher leak rate is more likely to be detected than a smaller leak rate. The situation is different in loss-of-coolant scenarios, where typically an overestimation of the coolant loss is conservative because the focus of the safety assessment is on the impact on pressure and temperature in the entire coolant loop.

The Standard Review Plan [29] does not specify details about recommended computational tools. The KTA standard [20] proposes several procedures in an Annex.

3. First benchmark phase

The first benchmark phase took place from 2019 to 2020. This phase concentrated on post-computation: the measured leak rates were communicated to the participants together with the circumstances of the operation and the leak. The first benchmark phase consists of four exercises: a laboratory test of an artificial slit, a laboratory test of a fatigue crack, an analysis of a real event in a nuclear power plant, and a sensitivity study on leak rate computation within an LBB assessment.

3.1. Exercise set

The exercise sets were provided to the participants in tabular form. These tables followed a structure of category, attribute, variable, value, and unit, in order to unify the presentation of leak settings and avoid misunderstandings. The exercise set categories were structure, structure material, loads, leak geometry, morphology and fluid. In the individual exercises, only those categories relevant for the individual case were provided. For example, in case of a fixed laboratory specimen with leaks, the material and load categories were omitted because their values do not enter the computation.

3.1.1. Artificial slit

The test case on the artificial slit specimen is based on the specimen "010T30" manufactured and measured in the "FSI" test rig at the University of Stuttgart. The information provided to the participants is summarised in Table 3.1; additional information on the tests is given in the appendix.

Table 3.1. Phase 1 artificial slit specification

Category	Attribute		Variable	Value	Unit
Structure	Geometry type		-	Plate	-
	Wall thickness		t	30	mm
	Additional loads			none	
Leak geometry	Approximate shape		-	Rectangle	-
	Interior	Full length	2c	27	mm
		Maximal width	COD	192-190-201	µm
		Cross section	COA	5.22	mm²
	Exterior	Full length	2c	28.15	mm
		Maximal width	COD	185-229-239	µm
		Cross section	COA	6.22	mm²
Morphology	Damage mechanism		-	Artificial	-
	Inlet form loss		zeta_in	Unknown	-
	Roughness	Local	Rz	22	µm
		Global	Rz	22	µm
	Bends	Local	N	0	-
		Global	N	0	-
	Measured total resistance		Zeta	4.32	-
Fluid (stagnation)	Pressure		p	variable	MPa
	Temperature		T	variable	°C

In the laboratory test, the temperature and pressure were variated, and the leak mass flow was measured. Two measurement principles were applied in the test (additional information on the instrumentation is given in the appendix). The fluid conditions and the measured values chosen for the computation benchmark are reproduced in Table 3.2.

Table 3.2. Phase 1 artificial slit fluid conditions and measured leak rates

Test no.	Data set	Pressure [bar]	Temperature [°C]	Measured mass flow rate [kg/s]	Second estimate [kg/s]
1	10	45.2	233.9	0.122	0.117
2	13	70.3	216.9	0.201	0.189
3	14	75.2	250.5	0.183	0.174
4	20	35.4	161.4	0.166	0.157
5	33	48.6	122.4	0.214	0.203
6	38	10.4	79.3	0.104	0.1

This information was the basis for each participant's evaluation.

3.1.2. Fatigue crack

The fatigue crack test case is based on the specimen "R5" tested at the University of Stuttgart. The specimen is made of a fatigue crack in a plate. The information provided for this exercise is summarised in Table 3.3; additional information on the tests is given in the appendix.

Table 3.3. Phase 1 fatigue crack specification

Category	Attribute		Variable	Value	Unit
Structure	Geometry type		-	Plate	-
	Wall thickness		t	7.8	mm
	Additional loads			None	
Leak geometry	Approximate shape		-	Rectangular	-
	Interior	Full length	2c	53.89	mm
		Maximal width	COD	79	µm
		Cross section	COA	4.26	mm²
	Exterior	Full length	2c	39.04	mm
		Maximal width	COD	48	mm
		Cross section	COA	1.87	mm²
Morphology	Damage mechanism		-	Fatigue	-
	Inlet form loss		zeta_in	Unknown	-
	Roughness	Local	Rz	Unknown	µm
		Global	Rz	40	µm
	Bends	Local	N	Unknown	-
		Global	N	Unknown	-
	Measured total resistance		Zeta	ca. 40	-
Fluid	Pressure		p	variable	MPa
	Temperature		T	variable	°C

From the variation of pressure and temperature in the test, six points were selected for the evaluation within the benchmark study. The selected points are shown in Table 3.4,

together with the measured flow rates as observed in the tests. As for the artificial slit case, a second estimate of the leak flow rate is also shown (additional information on the mass flow measurement can be found in the appendix).

Table 3.4. Phase 1 fatigue crack fluid conditions and measured leak rates

Test no.	Data set	Pressure [bar]	Temperature [°C]	Measured mass flow rate [kg/s]	Second estimate [kg/s]
1	2	65.7	204.3	0.016	0.0226
2	9	20.8	204.4	0.0061	0.0145
3	27	70.7	254.4	0.0164	0.0182
4	45	76.7	20.8	0.0408	0.0478
5	61	77.2	229.9	0.0165	0.0217
6	80	62.1	161.8	0.0331	0.0369

These two tables contain the information with which the participants started the evaluation.

3.1.3. Real event

The third exercise is the assessment of a real leak event from the operation of a nuclear power plant. A case discussed in [31] was chosen. The tabular specification of this test case is shown in Table 3.5. Due to a transcription error, a leak rate of 0.013 kg/s instead of 0.13 kg/s was used in the benchmark.

Table 3.5. Phase 1 real event case specification

Category	Attribute		Variable	Value	Unit
Structure	Geometry type		-	Pipe	-
	Outer diameter		D	37.7	mm
	Wall thickness		t	4.33	mm
Material	Number			"1.4550"	-
	Young's Modulus		E	186 000	MPa
	Yield stress		Rp0,1	167	MPa
	Ultimate stress		Rm	409	MPa
	Poisson number		nu	0.3	-
	Ramberg-Osgood	Prefactor	alpha	15.5	
		Exponent	n	2.5	
Loads	Pressure		p	15.9	MPa
	Bending		M	Unknown	Nm
Leak geometry	Orientation		-	Circumferential	-
	Approximate shape		-	Unknown	-
	Interior	Full length	2c	40	mm
		Estimated maximal width	COD	<0.05?	mm
		Cross section	COA	Unknown	mm²
	Mean	Full length	2c	36	mm
		Estimated maximal width	COD	0.05?	mm
		Cross section	COA	Unknown	mm²
	Exterior	Full length	2c	34	mm
		Estimated maximal width	COD	0.01?	mm
		Cross section	COA	Unknown	mm²

Table 3.5. Phase 1 real event case specification (Continued)

Category	Attribute		Variable	Value	Unit
Morphology	Damage mechanism		-	Fatigue	-
	Inlet form loss		zeta_in	Unknown	-
	Average roughness	Local	Rz	Unknown	µm
		Global	Rz	7.6	µm
	Mean roughness		Ra	2.3	
	Maximal roughness		Rt	10.6	
	Bends	Local	N	Unknown	-
		Global	N	Unknown	-
	Measured total resistance		Zeta	Unknown	-
Fluid	Pressure		p	15.9	MPa
	Temperature		T	40-70	°C
Leak rate	Measured flow rate		m	0.013(0.13)	kg/s

A key uncertainty in the analysis is the bending moment which influences the crack opening. Therefore, the variation of the bending moment and the assessment of the trend was part of the evaluation.

3.1.4. LBB sensitivity analysis

A leak assessment from the parallel LBB benchmark activity was included to study the sensitivity of the leak rate assessment in detail. The specification of the pipe in the LBB assessment is summarised in Table 3.6. This exercise represents a circumferential weld in a medium-sized pipe.

Table 3.6. Phase 1 LBB sensitivity study pipe specification

Category	Attribute	Variable	Value	Unit
Structure	Geometry type	-	Pipe weld	-
	Outer diameter	D	406.4	mm
	Wall thickness	t	40.462	mm
	Weld width	h	50.8	mm
Base material	Yield strength	Rp02	153.6	MPa
	Ultimate tensile strength	Rm	443	MPa
	Elastic modulus	E	176.7	GPa
	Poisson number	nu	0.3	-
	Ramberg-Osgood	σ_o	200.9	MPa
		ε_o	0.00114	-
		α	15.64	-
		n	3.75	-
Weld material	Yield strength	Rp02	316.5	MPa
	Ultimate tensile strength	Rm	542.4	MPa
	Elastic modulus	E	196.8	GPa
	Poisson number	nu	0.3	-
	Ramberg-Osgood	σ_o	332.35	MPa
		ε_o	0.00169	-
		α	0.386	-
		n	11.39	-
Loads	Axial force (prim.)	F	17.34	kN
	Axial force (sec.)	F	-4	kN
	Crack face pressure	p	7.75	MPa
	Bending (prim.)	M	21.59	kNm
	Bending (sec.)	M	68	kNm

The leak in this pipe is specified in the additional information shown in Table 3.7. A variation of the leak size in a circumferential through-wall flaw is assumed to conduct a sensitivity study.

Table 3.7. Phase 1 LBB sensitivity study leak specification

Category	Attribute		Variable	Value	Unit
Leak geometry	Orientation		-	Circumferential	-
	Approximate shape		-	Unknown	-
	Centre	Full length	2c	50-300	mm
		Maximal width	COD	Unknown	mm
		Cross section	COA	Unknown	mm²
Morphology	Damage mechanism		-	PWSCC	-
	Entry discharge coefficient		c_d	0.95	-
	Roughness	Local	µL	17 or 114	µm
		Global	µG	114	µm
	Bends	COD-dep.	N	5 940	1/m
		COD-indep.	N	5 020	1/m
	Path deviation	Local	K	1.2	-
		Global	K	1.2	-
	Measured total resistance		Zeta	Unknown	-
Fluid	Pressure		p	15.5	MPa
	Temperature		T	340	°C
Leak rate	Measured flow rate		m	Around 0.0608	kg/s

Two evaluations were requested: one for a local roughness value of 114 µm, and one for the local roughness of 17 µm.

3.2. Computation

3.2.1. BARC

BARC's analyses of the benchmark problems are performed with the SCALE (Slit and Crack Analysis for Leak Estimation) code (see Section 2.5.7).

3.2.2. GRS

GRS's analyses of the benchmark problems are performed with the WinLeck code (see Section 2.5.9) developed by GRS. WinLeck make it possible to flexibly specify the input variables of the individual benchmark exercises.

The artificial slit case provides the measured flow resistance value. Consequently, it is used as the best available information, while the surface morphology is not considered. As critical flow conditions are expected, the cross section on the exterior side is chosen for the modelling. Two different flow models are applied: the Pana model (Section 2.4.7) and the ATHLET-CDR model (Section 2.4.2). Both are considered as best-estimate descriptions, with the notable difference that the Pana model is based on equilibrium flow assumptions, while the ATHLET-CDR model considers non-equilibrium effects. The computed values of both models are shown in Table 3.8. Note that the CDR model only predicts critical flow and is not applicable to subcritical flow.

Table 3.8. GRS results of the artificial slit case

Data number	10	13	14	20	33	38
Pressure [bar]	45.2	70.3	75.2	35.4	48.6	10.4
Temperature [°C]	233.9	216.9	250.5	161.4	122.4	79.3
ATHLET-CDR [kg/s]	0.131	0.217	0.192	0.169	-	-
Pana [kg/s]	0.115	0.204	0.168	0.163	0.211	0.0969
Reference [kg/s]	0.122	0.201	0.183	0.166	0.214	0.104

The two models predict very similar results, with the ATHLET-CDR model showing a trend to higher mass flow rates, and the Pana model to lower rates. The experimental measurements mostly lie between the two models' results (with one exception, where it is slightly below the Pana value).

The fatigue crack analysis is done in analogy to the artificial slit case, but only the Pana model is applied. The results are shown in Table 3.9.

Table 3.9. GRS results of the fatigue crack

Data number	2	9	27	45	61	80
Pressure [bar]	65.7	20.8	70.7	76.7	77.2	62.1
Temperature [°C]	204.3	204.4	254.4	20.8	229.9	161.8
Computed leak rate [g/s]	25.4	8.75	20.4	34.8	24.6	28.0
Measured leak rate [kg/s]	16.0	6.1	16.4	40.8	16.5	33.1

The deviation between the model computation and the measurement is significantly larger than for the artificial slit case. In four cases, the computed leak rate is higher, and in two cases it is lower than the measured flow rate.

In the real event analysis, two different approaches are chosen for the leak opening area: one underestimating approach based on GRS-PB (see Section 2.2.3), and one based on a best-estimate approach, considering the LBB.ENG2 method (see Section 2.2.4). In both cases, the friction effects are modelled using the approach by Paul et al. (see Section 2.3.3), and the fluid motion is modelled using the Bernoulli model (the temperature is not considered to be of importance in this case). The high bending moment value is set to 0.1 kNm by engineering judgement, and the moderate bending moment to half of this value. The computed values are shown in Table 3.10.

Table 3.10. GRS result of the real event analysis

Bending moment [kNm]	Leak rate [g/s]	
	Unterestimation	Best-estimate
0	7.1	24
0.05	16	54
0.1	28	110

Compared with the reference result, the underestimation analysis includes a value below the reported value in the analysis example (13 g/s), while all best-estimate computations are above this value. Besides the uncertainty in resistance- and crack opening computation,

a negative bending moment could be an explanation for this discrepancy. The main conclusion from this task is that real events have possibly large uncertainties that lead to a large scatter band in a computational assessment. With respect to LBB-conservativity, at least in this example all best-estimate values overpredict the actual leak rate.

The LBB sensitivity problem consists of the computation of the COD (with the LBB.ENG2 method, see Section 2.2.4), the friction factor and flow resistance, and finally the fluid motion (with the ATHLET-CDR method, see Section 2.4.2), which represent analytical approaches of best-estimate quality. The two options of local roughness have the meaning of either using or ignoring an improved morphology model, making it possible to consider the roughness-bends transition for small crack openings. The result is shown in Table 3.11.

Table 3.11. Result of the LBB sensitivity analysis

Local roughness		114 µm		17 µm	
Full crack length	Crack open. displ.	Friction factor	Mass flow rate	Friction factor	Mass flow rate
[mm]	[mm]	[-]	[g/s]	[-]	[g/s]
50	25	∞	0	10.8	0.05
75	39	∞	0	1.26	4.63
100	55	∞	0	0.59	12.42
125	71	∞	0	0.39	25.05
150	90	∞	0	0.29	41.45
175	113	∞	0	0.23	63.01
200	139	113.3	11	0.19	90.73
225	167	7.48	55	0.164	124.32
250	198	2.67	107	0.15	166.58
275	231	1.42	167	0.134	213.57
300	284	0.76	258	0.12	289.53

It is worth comparing the COD to the effective roughness in this table, because the friction factor by Paul et al. becomes very large as they are of the same order. Obviously, the computed friction factor is much higher if no adjustment of the roughness is considered, which leads to a divergence of the friction factor below a full crack length of 200 mm. This divergence is avoided by assuming a local roughness value – although the friction factor for the smallest crack is also very high.

In conclusion, the exercise set was fully treatable with the WinLeck software. The individual exercises showed that leak rate predictions can be very accurate (artificial slit case) in idealised situations, but that in practice uncertainties are important to consider, where assessment can give an estimate of the range of possible values. The last exercise, the sensitivity analysis, showed clearly that careful choices of input parameters are required because this might have a large effect.

3.2.3. KEPCO E&C

KEPCO E&C' analyses of the benchmark problems were performed using a PICEP code developed by EPRI (see Section 2.5.6). PICEP is based on Henry's homogeneous non-equilibrium critical flow model as modified by Abdollahian and Chexal (see Section 2.4.4).

The wall thickness, full lengths of the crack at both interior and exterior, COD values measured at three different positions, and COA were provided for the artificial slit case. The wall thickness and full lengths were employed for the analysis, and the COD values at

both interior and exterior were assumed to be 0.193 and 0.221 mm, respectively, so that the calculated cross section is the same as the provided COA. For crack morphology parameters, a surface roughness of 22 μm was applied and the number of turns was assumed to be 0 m⁻¹. The calculated values are summarised in Table 3.12. These results are generally underestimated compared to the measured values.

Table 3.12. Results of the artificial slit case calculated by KEPCO E&C

Data number	10	13	14	20	33	38
Pressure [bar]	45.2	70.3	75.2	35.4	48.6	10.4
Temperature [°C]	233.9	216.9	250.5	161.4	122.4	79.3
Computed leak rate [kg/s]	0.095	0.163	0.141	0.127	0.149	0.081
Reference [kg/s]	0.122	0.201	0.183	0.166	0.214	0.104

In case of the fatigue crack analysis, global roughness was provided, and the statistical number of turns value of 6 730 m⁻¹ was adopted according to Rahman's research [14]. The predicted leak rates, as listed in Table 3.13, are lower than the measured leak rates. There's a more significant discrepancy between the model computation and the measured values (as referenced in Table 3.13) in case of low pressure and temperature.

Table 3.13. Results of the fatigue crack calculated by KEPCO E&C

Data number	2	9	27	45	61	80
Pressure [bar]	65.7	20.8	70.7	76.7	77.2	62.1
Temperature [°C]	204.3	204.4	254.4	20.8	229.9	161.8
Computed leak rate [kg/s]	0.012	0.0024	0.0089	0.015	0.0123	0.0116
Measured leak rate [kg/s]	0.016	0.0061	0.0164	0.0408	0.0165	0.0331

The real event analysis includes the calculation of the COD. Participants in this benchmark project were required to select three levels of applied moment. The elastic-plastic estimation scheme, based on the GE/EPRI ductile fracture handbook (see Section 2.2.1), was adopted to predict the COD. In case of the applied moment, the high bending moment value ($M_{H.L}$) was calculated based on the design bending moment described in the ASME Boiler and Pressure Vessel (B&PV) Code Section NB [32]. Below is the equation used for this calculation:

$$M_{H.L.} = \frac{2I}{D_o}\left(1.5S_m - \frac{P_i D_o}{2t}\right)$$

where I, D_o, P_i and S_m are the moment of inertia, outer diameter, internal pressure, and design stress intensity, respectively. The S_m value of 138 MPa was used according to ASME B&PV Code Sec. II. The medium and zero level of bending moments are set to be half of $M_{H.L}$ and zero, respectively. The evaluated values are shown in Table 3.14. The assumption of applied bending moment caused the overestimation of the COD values as compared to the reference values and resulted in the over-prediction of the leak rate as well.

Table 3.14. Result of the real event analysis evaluated by KEPCO E&C

Bending moment [kNm]	Leak rate [g/s] best-estimate
0	64.9
0.235	1 038.9
0.470	4 409.8

The LBB sensitivity analysis aims to find out the effect of local roughness, especially for the tight crack case. For the COD prediction, the elastic-plastic estimation scheme was employed based on the GE/EPRI ductile fracture handbook (see Section 2.2.1). Henry's homogeneous non-equilibrium critical flow model was adopted. Since PICEP receives one variable for surface roughness, only the results for a surface roughness of 114 µm are presented in Table 3.15.

Table 3.15. Result of the LBB sensitivity analysis by KEPCO E&C

Local roughness		114 µm
Full crack length	Crack open. displ.	Mass flow rate
[mm]	[µm]	[g/s]
50	26	1.3
75	41	3
100	58	5.6
125	77	9.4
150	99	14.4
175	124	21.2
200	155	31.1
225	191	47.3
250	233	69.7
275	283	100.3
300	342	141.5

In conclusion, the exercise set for Phase I was treatable with the PICEP software. It is worth noting that there is a more significant discrepancy between the model computation and the measured values (Table 3.13) in case of low pressure and temperature.

3.2.4. KINS

KINS' analyses of the benchmark problems were performed using a LEAPOR code developed by Oak Ridge National Laboratory (see Section 2.5.4). LEAPOR is based on the modified Henry-Fauske model for the thermo-hydraulic calculation (see Section 2.4.4).

The wall thickness, full lengths of the crack at both interior and exterior, COD values measured at three different positions, and COA were provided for the artificial slit case. The wall thickness and full lengths were employed for the analysis, and the COD values at both interior and exterior were assumed to be 0.193 and 0.221 mm, respectively, so that the calculated cross section is the same as the provided COA. For crack morphology parameters, both local and global roughness were assumed to be 22 µm, and local and global path deviations of 1.1 were applied. The calculated values are summarised in Table 3.16. This result is generally underestimated compared to the measured values.

Table 3.16. Results of the artificial slit case calculated by KINS

Data number	10	13	14	20	33	38
Pressure [bar]	45.2	70.3	75.2	35.4	48.6	10.4
Temperature [°C]	233.9	216.9	250.5	161.4	122.4	79.3
Computed leak rate [kg/s]	0.095	0.167	0.143	0.131	0.153	-
Reference [kg/s]	0.122	0.201	0.183	0.166	0.214	0.104

For the fatigue crack analysis, global roughness was provided, and the statistical local roughness value of 8.814 μm was adopted according to Rahman's research [14]. Local and global path deviations were assumed to be 1.017 and 1.06, respectively [14]. The predicted leak rates, as listed in Table 3.17, are higher than the measured leak rates. There's a significant discrepancy between the model computation and the measured values (as referenced in Table 3.17) as compared to the artificial slit case.

Table 3.17. Results of the fatigue crack calculated by KINS

Data number	2	9	27	45	61	80
Pressure [bar]	65.7	20.8	70.7	76.7	77.2	62.1
Temperature [°C]	204.3	204.4	254.4	20.8	229.9	161.8
Computed leak rate [kg/s]	0.0285	0.0077	0.026	-	0.0293	0.03
Measured leak rate [kg/s]	0.016	0.0061	0.0164	0.0408	0.0165	0.0331

The real event analysis includes the calculation of the COD. Participants in this benchmark project were required to select three levels of applied moment. The elastic-plastic estimation scheme, based on the GE/EPRI ductile fracture handbook (see Section 2.2.1), was adopted to predict the COD. In case of the applied moment, the high bending moment value ($M_{H.L.}$) was calculated based on the design bending moment described in the ASME Boiler and Pressure Vessel (B&PV) Code Section NB [32]. Below is the equation used for the calculation:

$$M_{H.L.} = \frac{2I}{D_o}\left(1.5 S_m - \frac{P_i D_o}{2t}\right)$$

where I, D_o, P_i and S_m are the moment of inertia, outer diameter, internal pressure, and design stress intensity, respectively. The S_m value of 138 MPa was used according to ASME B&PV Code Sec. II. The medium and zero level of bending moments are set to be half of $M_{H.L.}$ and zero, respectively. The evaluated values are shown in Table 3.18. The assumption of the applied bending moment caused the overestimation of the COD values as compared to the reference values and resulted in the over-prediction of the leak rate as well.

Table 3.18. Result of the real event analysis evaluated by KINS

Bending moment [kNm]	Leak rate [g/s] best-estimate
0	-
0.235	3 727
0.470	1 538

The LBB sensitivity analysis aims to find out the effect of local roughness, especially for the tight crack case. For the COD prediction, the elastic-plastic estimation scheme was employed based on the GE/EPRI ductile fracture handbook (see Section 2.2.1). The modified Henry-Fauske model was adopted to evaluate the friction factor, flow resistance, and fluid motion (see Section 2.4.4). The results are summarised in Table 3.19.

Table 3.19. Result of the LBB sensitivity analysis by KINS

Local roughness		114 µm		17 µm	
Full crack length	Crack open. displ.	Friction factor	Mass flow rate	Friction factor	Mass flow rate
[mm]	[µm]	[-]	[g/s]	[-]	[g/s]
50	26	0.924	2	0.924	2
75	40	0.924	5.4	0.924	5.4
100	56	0.924	11.2	0.639	12.4
125	73	0.924	20	0.416	24.1
150	93	0.924	32.8	0.310	40.4
175	116	0.924	50.7	0.248	62.3
200	143	0.924	75.2	0.209	91.3
225	175	0.924	108.4	0.182	129.5
250	212	0.924	152.8	0.162	179.5
275	255	0.924	211.8	0.147	245
300	306	0.636	302.9	0.136	330.6

When the full crack length is less than 275 mm, the computed friction factors with the local roughness of 114 µm are much higher than those with adjusted local roughness of 17 µm, which leads to the underprediction of the leak rate.

In conclusion, the exercise set for Phase I was treatable with the LEAPOR software except for the low pressure and temperature case (see Table 3.16 and Table 3.17). In addition, the artificial slit case, which is an idealised experimental case, shows a good agreement with measured results, while the results of fatigue crack and real event analysis were quite different. This is attributed to the fact that the greater the number of variables to be assumed, the greater is the difference from the referenced value.

3.2.5. KIWA

KIWA's analyses of the benchmark problems are done with the ExcelSQUIRT code (see Section 2.5.2). ExcelSQUIRT has a simplified user interface as compared to previous versions (SQUIRT or WinSQUIRT). ExcelSQUIRT also lacks an opportunity to obtain intermediate results that are part of an analysis (leak rate is the only result from an analysis).

The artificial slit case provides the measured flow resistance values. KIWA used the mean COD values as input data for the analysis, although a better agreement was observed when using the maximum COD values (see Figure 3.1).

Table 3.20. KIWA results of the artificial slit case

Data number	10	13	14	20	33	38
Pressure [bar]	45.2	70.3	75.2	35.4	48.6	10.4
Temperature [°C]	233.9	216.9	250.5	161.4	122.4	79.3
KIWA [kg/s]	0.0918	0.154	0.1345	0.12	0.137	0.0805
Reference [kg/s]	0.122	0.201	0.183	0.166	0.214	0.104

Figure 3.1. KIWA results of the artificial slit case, sensitivity analysis using different COD
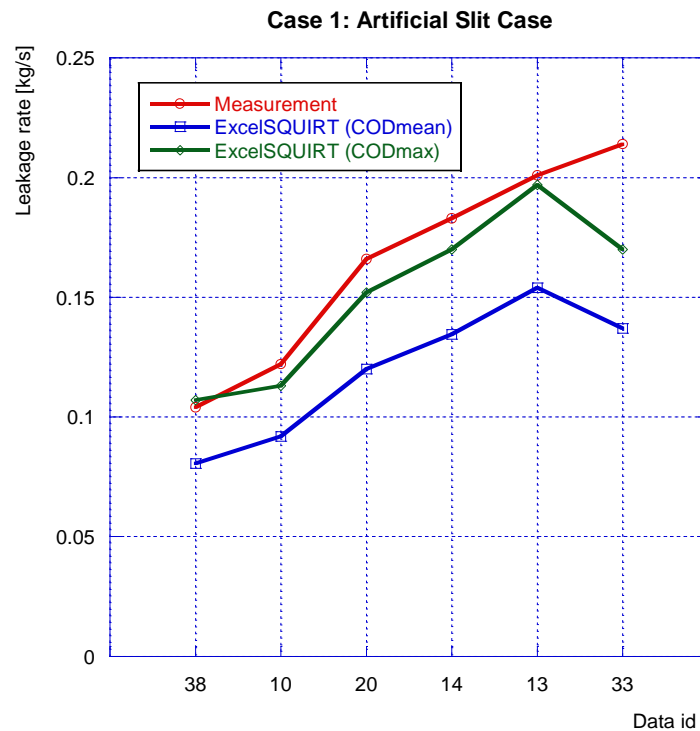
The fatigue crack analysis is done in analogy to the artificial slit case. The results are shown in Table 3.21.

Table 3.21. KIWA results of the fatigue crack

Data number	2	9	27	45	61	80
Pressure [bar]	65.7	20.8	70.7	76.7	77.2	62.1
Temperature [°C]	204.3	204.4	254.4	20.8	229.9	161.8
Computed leak rate [kg/s]	0.023	0.0055	0.021833	-	0.024	0.024
Measured leak rate [kg/s]	0.016	0.0061	0.0164	0.0408	0.0165	0.0331

As shown in Table 3.21, no result was obtained for case 45 using ExcelSQUIRT. In order to get a valid result, it was necessary to assume a higher temperature for this case.

In **the real event analysis**, the bending moment in the plant is unknown, but relevant for the answer. Also, other inputs are given with great uncertainty. A sensitivity analysis is therefore needed, and KIWA investigated different bending moments that cause bending stress between 0 and 50 MPa. The internal pressure of 15.9 MPa causes an axial stress of 23.2 MPa. The COD evaluation using KIWA's in-house code gave inconsistent results. Therefore, checks were also performed with the WinLeck code from GRS. The results are shown in Figure 3.2.

Figure 3.2. KIWA results of the real event analysis, sensitivity analysis using different global bending stresses
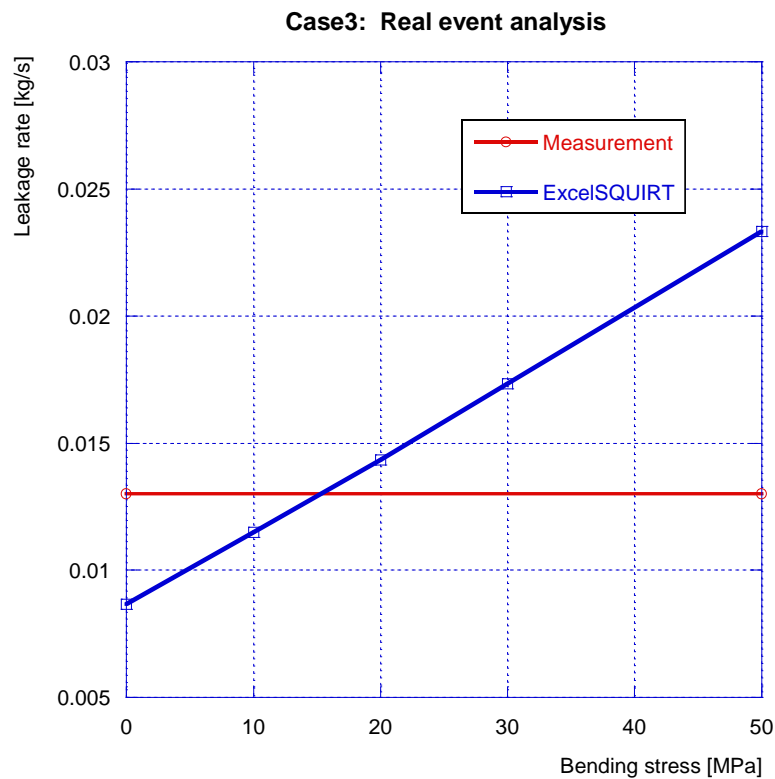
As can be seen from this sensitivity analysis, the best agreement was obtained using a global bending stress of 15 MPa.

The LBB sensitivity problem involves analysing how the results are affected by using different crack lengths (50 to 300 mm). An investigation of the influence of the local roughness was also part of this analysis. The results are shown in Figure 3.3 (using a local roughness of 17 μm).

Figure 3.3. KIWA results of the LBB sensitive study, sensitivity analysis using different crack lengths
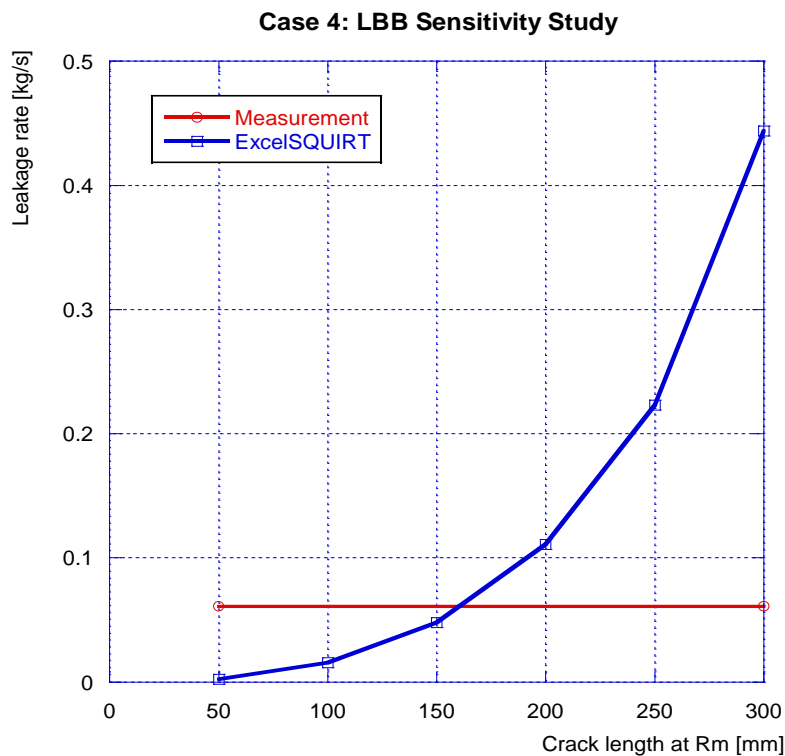
3.2.6. NRC

The leak rate for the artificial slit case was determined using LEAPOR, (see Section 2.5.4). The geometry and thermodynamic parameters for the artificial slit problem that were given in the problem description were used for the inputs to the calculation using LEAPOR and its GUI input programme, LEAPOR-SA. The specified inside diameter and outside diameter crack lengths (2c) were used and the COD values were the average of the three specified in the problem description. A rectangular crack cross section was assumed. A second set of calculations was performed using COD values derived from the tabulated 2c and COA values. The specified total resistance value, zeta, was not used in the calculation as LEAPOR internally performs its own calculation of the Darcy friction factor. Since the slit was artificial and no further information was given, a value of zero was assumed for the number of turns per unit length parameter, and an entry loss coefficient of 0.95 is hard-coded in LEAPOR. The leak path deviation parameters were assumed to be unity. The calculation for single-phase leak, data number 38, could not be performed because LEAPOR is specifically designed for two-phase calculations, and the LEAPOR solver could not converge for the data number 33 calculation; no leak rate data are reported for these two cases.

Table 3.22. NRC results of the artificial slit case

Data number	10	13	14	20	33	38
Pressure [bar]	45.2	70.3	75.2	35.4	48.6	10.4
Temperature [°C]	233.9	216.9	250.5	161.4	122.4	79.3
Leak rate (2c, COD) [kg/s]	0.0969	0.1738	0.14802	0.13671	N/A	N/A
Leak rate (2c, COA) [kg/s]	0.1310	0.2495	0.2079	0.1957	N/A	N/A

The results of the artificial slit calculations mirror the measured mass flow rates given in Table 3.2, with the predicted leak rate calculated using the average of the three values of the COD, 194 and 218 µm for interior and exterior, respectively, consistently underestimating the measured values. Using the COD calculated from the COA and 2c for the interior and exterior, 230 and 185 µm, respectively, the calculated leak rates consistently overestimated the measured values.

As for the artificial slit case, LEAPOR was used to perform the leak rate estimates for the fatigue cracks. COD-dependent crack morphology parameters for CF with local roughness of 8.8 µm, global roughness of 40.5 µm, turns per metre of 6 730, global path length of 1.017 and global plus local path length of 1.06 were chosen. As before, the COD was evaluated from the COA and 2c values, but since the calculated COD values did not differ significantly from the tabulated COD values, only calculations using the tabulated COD values were performed. Data number 45 could not be evaluated because it involved a single-phase leak.

Table 3.23. NRC results of the fatigue crack

Data number	2	9	27	45	61	80
Pressure [bar]	65.7	20.8	70.7	76.7	77.2	62.1
Temperature [°C]	204.3	204.4	254.4	20.8	229.9	161.8
Leak rate [g/s]	0.028	0.0077	0.0261	N/A	0.0293	0.030

As opposed to the artificial slit case, LEAPOR tended to overestimate the measured leak rate for the fatigue crack cases. This result was somewhat surprising since the morphology parameters that were used had a relatively large value for the number of turns, a parameter that has a strong influence on the calculated leak rate. The difference between the measured leak rate value and the LEAPOR estimate did not show a correlation with the degree of undercooling, which could have indicated errors in the model implementation. Since the temperatures and pressures for the different measurements were generally similar, there is a possibility that the differences lie in the leak rate measurements. This hypothesis may be supported by the spread in measured values between the first and second measurements.

The NRC could not provide leak rate data for the real event analysis because the water temperature for this problem, 40–70°C, would have resulted in single-phase flow. The best-estimate COD values for each bending moment were evaluated for 50% crack face pressure (CFP), the under-estimate for 0% CFP and the over-estimate for 100% CFP. All of the reported COD values are those at the mid-wall. The moment for the medium bending moment was selected so that the sum of the axial stress and the bending stress was approximately 25% of the yield stress, and the high moment resulted in approximately 60 MPa bending stress. No additional axial force beyond that from internal pressure was added to any of the evaluations.

Table 3.24. NRC result of the real event analysis

Bending moment [kNm]	COD [mm]			
	Under est.	Best est.	Over est.	Comment
0	0.075	0.120	0.177	Zero moment
0.06	0.178	0.249	0.334	Medium moment
0.2	0.658	0.806	0.972	High moment

The last Phase I exercise was the LBB sensitivity analysis, where the leak rate was estimated for varying crack lengths and two different local roughnesses, 114 and 17 µm. Table 3.25 shows the friction factors and mass flow rates for each of the crack lengths, as well as the COD-dependent effective roughness (mu_{eff}) and effective number of turns per unit length (ntL_{eff}). For most crack lengths, the friction factor remained constant for the 114 µm local roughness until very long crack lengths, and corresponding CODs were reached. The COD-dependent effective number of turns changed only slightly. For the 17 µm local roughness, the friction factor decreased rapidly for longer crack lengths, and the effective roughness increased. Since the effective number of turns only depends on the ratio of the COD to global roughness, the effective number of turns was the same for the 114 and 17 µm local roughness calculations.

Table 3.25. NRC result of the LBB sensitivity analysis

Local roughness		114 µm				17 µm			
Full crack length	Crack open. displ.	Friction factor	mu_{eff}	ntL_{eff}	Mass flow rate	Friction factor	mu_{eff}	ntL_{eff}	Mass flow rate
[mm]	[mm]	[-]	[µm]	[1/m]	[kg/s]	[-]	[µm]	[1/m]	[kg/s]
50	0.019	0.924	114	5 904	0.0013	0.924	17.7	5 904	0.0013
75	0.030	0.924	114	5 852	0.0036	0.924	18.6	5 852	0.0036
100	0.042	0.924	114	5 795	0.0076	0.924	19.6	5 795	0.0076
125	0.056	0.924	114	5 729	0.0141	0.634	20.8	5 729	0.0157
150	0.072	0.924	114	5 653	0.0235	0.426	22.2	5 653	0.0283
175	0.091	0.924	114	5 563	0.0372	0.318	23.8	5 563	0.0458
200	0.111	0.924	114	5 468	0.0549	0.260	25.6	5 468	0.0676
225	0.133	0.924	114	5 364	0.0777	0.222	27.5	5 364	0.0948
250	0.157	0.834	114	5 250	0.1064	0.196	29.5	5 250	0.1283
275	0.183	0.573	114	5 127	0.1419	0.177	31.7	5 127	0.1689
300	0.223	0.385	114	4 938	0.1985	0.158	35.2	4 938	0.2321

3.2.7. OCI

OCI's analyses of the benchmark problems were carried out with the LOCI™ code (see Section 2.5.5), developed by OCI.

In the context of an LBB assessment where emphasis is placed on the detection of small leakage rates, the distinction between *conservative* and *best-estimate* models becomes very important. This classification can provide guidance on where these models can be appropriately applied, taking account of margins and uncertainties. A *conservative* leakage-rate model is required to consistently underestimate the actual leakage rate and is typically applied in deterministic procedures, e.g. the deterministic approach in the German standard

KTA 3206. A *best-estimate* leakage-rate model places greater emphasis on predictive accuracy. In a probabilistic framework, this model's estimated solutions can serve as a measure of central tendency (mean, median, or mode) for a prescribed statistical distribution characterising the uncertainties in the leakage-rate predictions. LOCI™ provides both *best-estimate* and *conservative* leakage-area and leakage-rate models.

Note on morphology parameters

LOCI™ contains a database of morphology parameters preselected as a function of damage mechanism. In Table 3.26, the values from this database are compared to the parameters provided in the problem statements for three cases: (1) Fatigue crack, (2) Real event, and (3) LBB sensitivity.

Table 3.26. Morphology parameters as a function of damage mechanism

Data Source	Damage Mechanism	Rz(local) (microns)	Rz(global) (microns)	Rt(max) (microns)	h_{tL} 1/m	K_G (-)	K_{G+L} (-)
LOCI Database	fatigue	8.814	40.51	NA	6730	1.017	1.060
Fatigue Crack Case	fatigue	NA*	40.00	NA	NA	NA	NA
Real Event Case	fatigue	NA	7.60	10.6	NA	NA	NA
LOCI Database	PWSCC	16.86	114	NA	5940	1.009	1.243
LBB Sensitivity	PWSCC	17 or 114	114	NA	5940	1.2	1.2

*NA = not available

OCI results for the artificial slit case

Two leakage-rate models included in LOCI™ are applied in the analysis of the *artificial slit case*: 1) the extended Henry-Fauske *best-estimate* model (see Section 2.4.4) and 2) the *conservative* modified Bernoulli model (see Section 2.4.6). The computed values from both models are shown in Table 3.27 and comparisons to the measured leakage rates for this case are presented in Figure 3.4.

As shown in Figure 3.4, the leakage-rate results for the modified Bernoulli model consistently underestimate the actual leakage rate for this case, thus satisfying the design intent of a conservative model as required by the KTA 3206 standard [20]. Compared to the modified Bernoulli model, the results from the Henry-Fauske model provide predicted leakage rates that are closer to the experimentally-measured data for the *artificial slit case*, as expected for a best-estimate model.

Table 3.27. OCI results for the artificial slit case using LOCI™

Data number	10	13	14	20	33	38
Pressure [bar]	45.2	70.3	75.2	35.4	48.6	10.4
Temperature [°C]	233.9	216.9	250.5	161.4	122.4	79.3
Henry-Fauske [kg/s]	0.0966	0.171	0.146	0.134	0.156	0.0932
modified Bernoulli [kg/s]	0.0563	0.102	0.0844	0.0818	0.105	0.0496
Measured leak rate [kg/s]	0.122	0.201	0.183	0.166	0.214	0.104

Figure 3.4. Artificial slit case LOCI™ solutions from Henry-Fauske and modified Bernoulli models
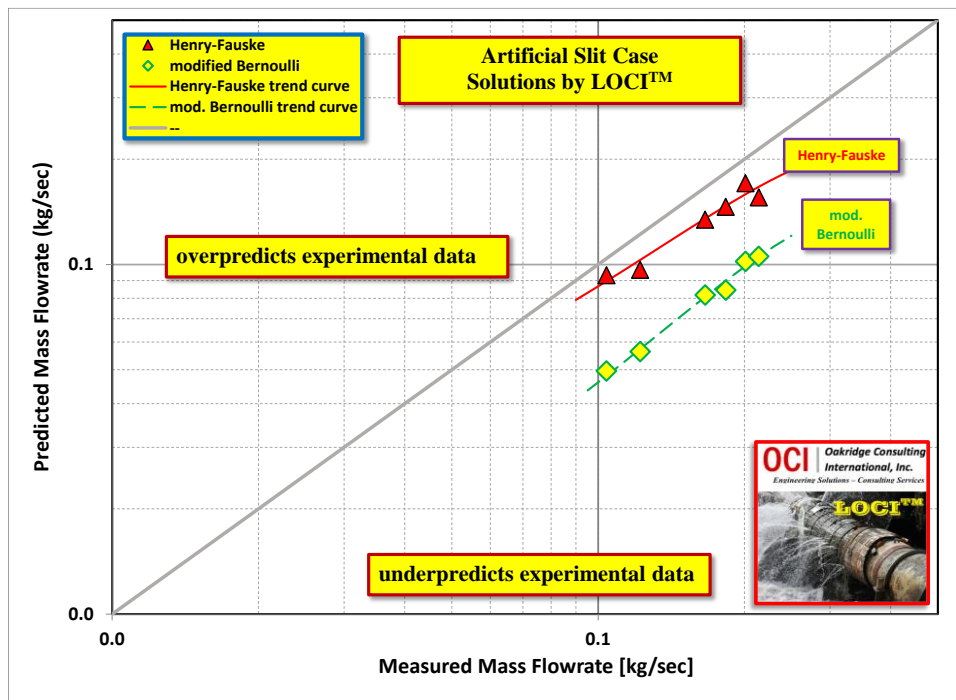
OCI results for the fatigue crack case

LOCI ™ analysis results for the fatigue crack case are listed in Table 3.28 and shown in Figure 3.5. Flow-rate solutions were calculated for each case using the *conservative* modified Bernoulli and the *best-estimate* Henry-Fauske models. For the Henry-Fauske solutions, a comparison is made in Table 3.28 between the morphology parameters provided in the fatigue crack problem statement and the parameters taken from the LOCI™ database (see Table 3.26).

Table 3.28. OCI results for the fatigue crack case using LOCI™

Data number	2	9	27	45	61	80
Pressure [bar]	65.7	20.8	70.7	76.7	77.2	62.1
Temperature [°C]	204.3	204.4	254.4	20.8	229.9	161.8
Henry-Fauske* [g/s]	28.1	7.7	25.7	34.7	28.9	29.6
Henry-Fauske** [g/s]	28.4	7.7	26.0	35.0	29.2	30.0
modified Bernoulli [g/s]	15.3	4.3	11.1	20.6	15.1	16.8
Measured leak rate [g/s]	16.0	6.1	16.4	40.8	16.5	33.1

*Morphology parameters provided in fatigue crack case problem statement.
**Morphology parameters taken from Table 3.26 LOCI™ database.

Figure 3.5. Fatigue crack case solutions from the Henry-Fauske and modified Bernoulli models
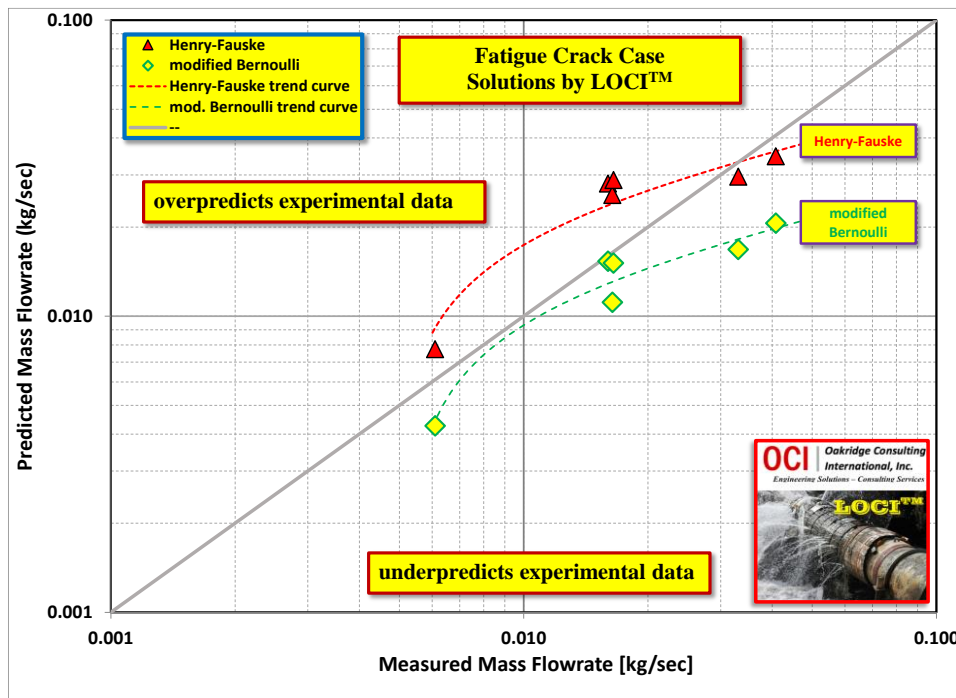
As observed for the artificial slit case, the *conservative* modified Bernoulli leakage-rate solutions are consistently lower than the *best-estimate* Henry-Fauske predictions. The modified Bernoulli leakage-rate predictions trend towards underestimating the experimental data.

OCI results for the real event case

LOCI ™ analysis results for the real event case are listed in Table 3.29 for three bending levels: 1) no bending, 2) medium bending at 0.05 [kN-m], and 3) high bending at 0.1 [kN-m]. In addition to the applied bending moment, pressure loading is also included in the required leakage-area analysis using the modified GE/EPRI model available in LOCI™.

Table 3.29. OCI results for the real event case using LOCI™

Bending moment [kN-m]	Leak rate [g/s]		
	Under-estimate	Best-estimate	Over-estimate
0	29.2	54.8	291
0.05	31.5	59.2	292
0.1	33.9	63.8	292

The Henry-Fauske solutions in Table 3.29 make use of the LOCI™ flow regimes that are defined in a transition model developed for the MERIT project and described in [44]. This transition model is divided into four flow regimes as shown in Figure 3.6.

- Regime 1: $L_{eff} / D_h > 30$ (Henry-Fauske model for two-phase critical [choked] flow)

- Regime 2: Bridge between Regime 1 and Regime 3 (Henry-Fauske model at $L_{eff} / D_h = 30$)

- Regime 3: Transition – linear interpolation of G_c^2 solution between $4.6 < L_{eff} / D_h < 12$

- Regime 4: Orifice flow of subcooled liquid – $p_c / p_0 = 0.522$ (fixed) at $L_{eff} / D_h = 4.6$

where

L_{eff} = effective crack flow length including morphology effects
D_h = hydraulic diameter of crack flow channel
G_c = critical leakage rate of mass flux at crack exit
p_c = critical pressure at crack exit
p_0 = fluid pressure inside of pipe

In Table 3.29, three estimation types are included:

1. an ***under-estimate*** solution based on the *linear-elastic GE/EPRI* leakage-area model (Section 2.2.2) and the modified Bernoulli leakage-rate model (Section 2.4.6),

2. a ***best-estimate*** solution based on the *linear-elastic GE/EPRI* leakage-area model (Section 2.2.2) and the Henry-Fauske leakage-rate model (Section 2.4.4) (Regime 1 – two-phase critical flow), and

3. an ***over-estimate*** solution based on the *elastic-plastic GE/EPRI* leakage-area model (Section 2.2.1) and the LOCI™ leakage-rate model for high flows (Regime 2 – bridge between Regime 1 and Regime 3).

Figure 3.6. Transition model in LOCI™ – flow regime definitions.
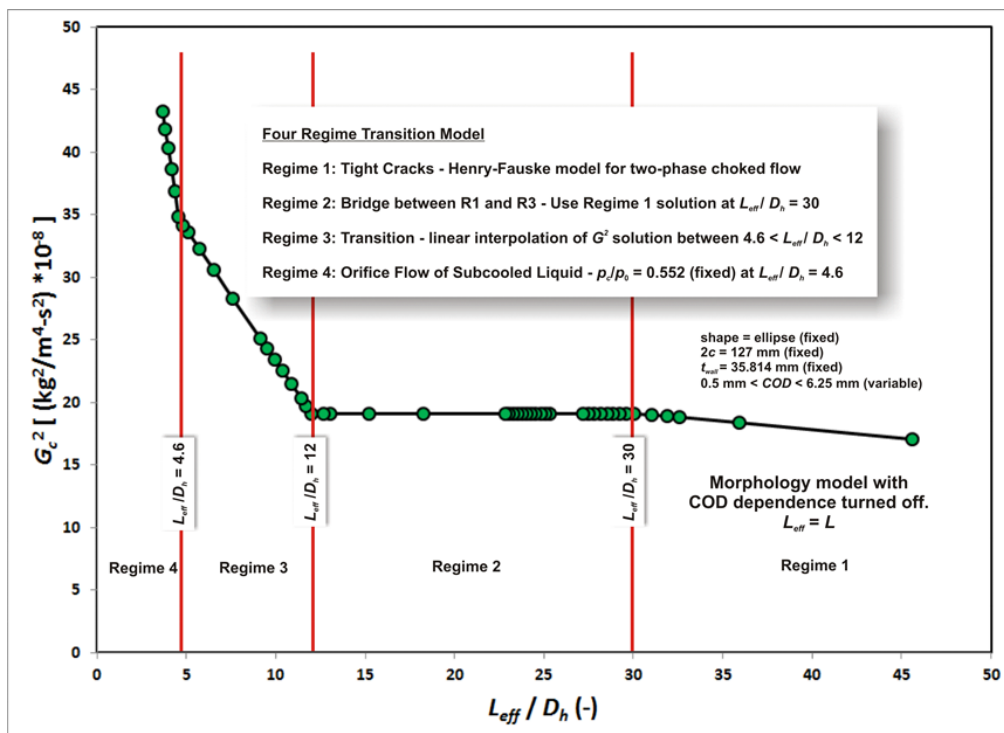
OCI results for the LBB sensitivity case

The OCI results for the LBB sensitivity case are presented in Table 3.30, where all cases were executed using the Henry-Fauske model implemented in LOCI™. The CODs were calculated using the EPFM GE/EPRI method (Section 2.2.1).

Table 3.30. OCI results of the LBB sensitivity analysis

Local roughness		Rz (local) = 114 µm		Rz (local) = 17 µm	
Crack length, 2*c*	Average COD	Darcy friction factor, *f*	Mass flow rate	Darcy friction factor, *f*	Mass flow rate
[mm]	[µm]	[-]	[g/s]	[-]	[g/s]
50	26	0.924	2.83	0.924	2.83
75	40	0.924	7.59	0.516	8.87
100	55	0.924	15.3	0.322	18.9
125	72	0.924	26.9	0.236	33.3
150	94	0.924	44.7	0.188	54.3
175	117	0.924	68.9	0.159	82.1
200	143	0.924	101	0.141	118
225	171	0.924	141	0.127	163
250	202	0.661	200	0.118	218
275	234	0.475	271	0.111	286
300	290	0.326	389	0.103	401

For the local roughness of 114 µm, the primary contributors to the total pressure drop are shown as percentages of the total pressure loss in Figure 3.7. For short cracks, the frictional pressure drop plays a dominant role. As the crack becomes longer, this wall friction effect falls off and the morphology of the crack face becomes more dominant. Figure 3.8 demonstrates that the same trends can be observed when the local roughness is 17 µm; however, the contribution of the wall friction to the total pressure loss decreases more rapidly than in the 114 µm case. In both cases the pressure drop due to crack path tortuosity dominates for longer crack lengths.

Figure 3.7. Primary contributors to total pressure drop with local Rz = 114 μm.
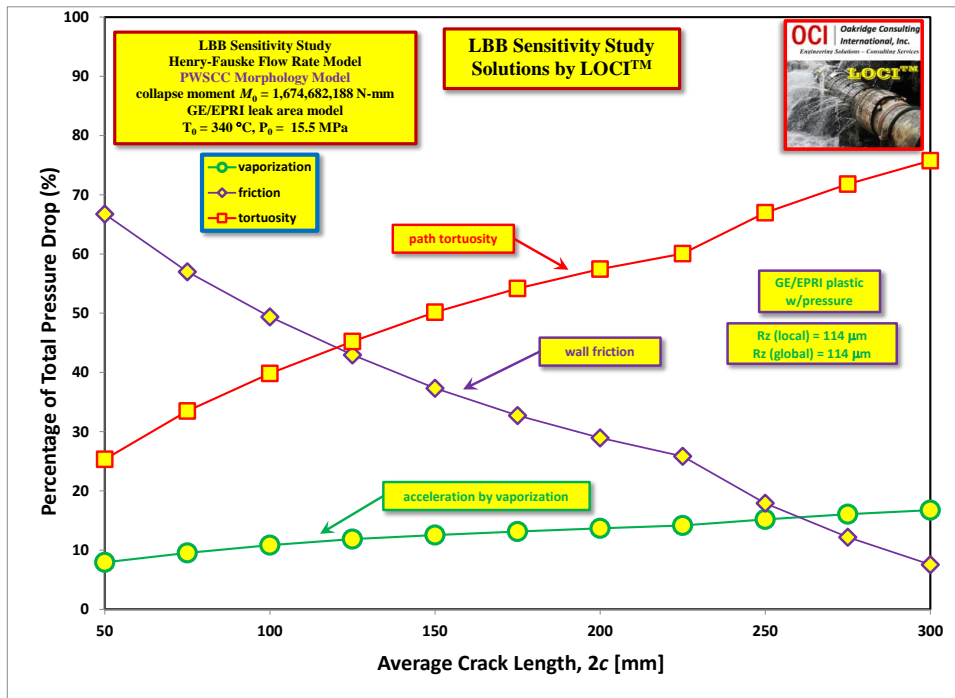
Figure 3.8. Primary contributors to total pressure drop with local Rz = 17 μm
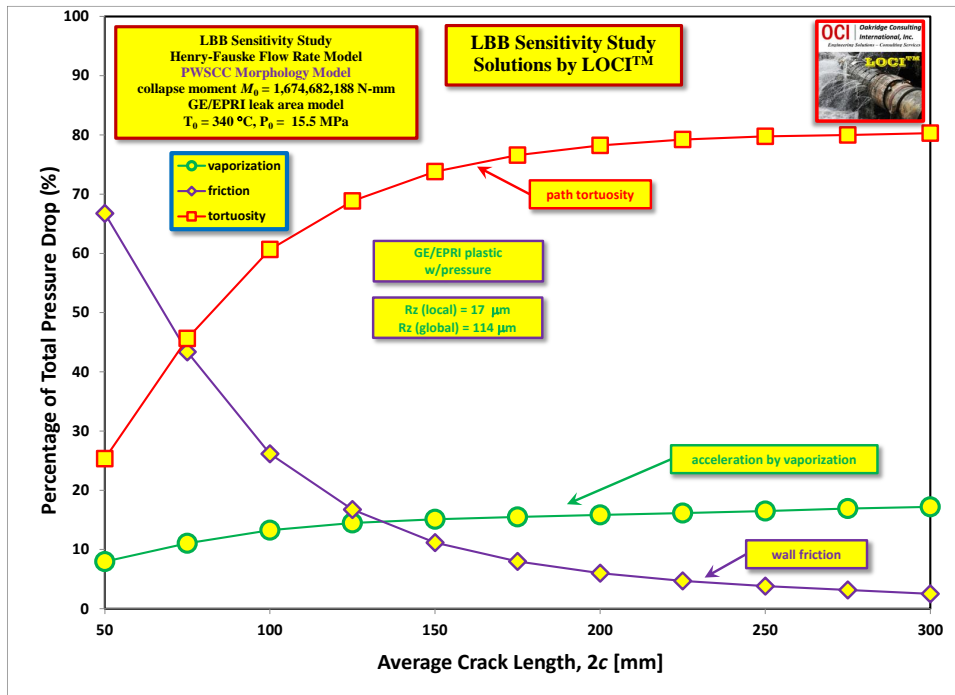
3.2.8. PSI

PSI used the LEAPOR (see Section 2.5.4) code with the Henry-Fauske model (see Section 2.4.4) to calculate the friction and resistance, and the homogeneous equilibrium model (HEM) was used as the flow model. The HEM approach considers the two-phase mixture to be a pseudo-fluid, which can be described by the same conservation law principles that are valid for a single-phase flow condition. In this model, the two phases are assumed to be everywhere in a state of both thermal and mechanical equilibrium. For adiabatic flow, the process is assumed to be reversible and, therefore, isentropic, and the velocities of the two phases are assumed to be equal. The equilibrium properties of the two phases can be obtained from a water-property formulation ("Steam Tables") implemented in the code or from some general equation of state.

Note that LEAPOR can only deal with pipe cases. Therefore, the plate was approximated as a very large pipe with an outer diameter of 10^{10} mm.

Table 3.31. PSI results of the artificial slit case

Data number	10	13	14	20	33	38
Pressure [bar]	45.2	70.3	75.2	35.4	48.6	10.4
Temperature [°C]	233.9	216.9	250.5	161.4	122.4	79.3
Measured mass flow rate [kg/s]	0.122	0.201	0.183	0.166	0.214	0.104
Second estimate [kg/s]	0.1	0.203	0.157	0.174	0.189	0.117
Leak rate [kg/s]	0.102	0.172	0.15	0.135	0.161	0.16
Difference [%]	2	2.9	3.3	3.1	5.3	5.1

Compared with the measured mass flow rate, the numerical leak rate is a bit lower when the temperature and pressure exceed 122.4°C and 35.4 MPa, respectively, but is more in agreement with the second estimate. However, the calculated flow rates are in good agreement with the measured ones because the difference between the measured and calculated rate is less than 5%. Note that the calculated leak rate is higher than the measured one when the temperature and pressure are lower, i.e. 79.3°C and 10.4 MPa, respectively. It can be inferred that there exists a pressure and temperature limit in the implemented model of LEAPOR, below which the leak rate would be overestimated.

In addition, it is found for the artificial slit case that the internal pressure has more influence on the leak rate than the temperature. When the pressure is increased from 45.2 bar to 48.6 bar, the leak rate is increased by 50% although the temperature is reduced from 233.9°C to 122.4°C. Likewise, the leak rate increased also by 50% with the temperature around 240°C when the pressure is increased from 45.2 bar to 75.2 bar.

Table 3.32. PSI results of the fatigue crack

Data number	2	9	27	45	61	80
Pressure [bar]	65.7	20.8	70.7	76.7	77.2	62.1
Temperature [°C]	204.3	204.4	254.4	20.8	229.9	161.8
Measured mass flow rate [kg/s]	0.016	0.0061	0.0164	0.0408	0.0165	0.0331
Second estimate [kg/s]	0.0226	0.0145	0.0182	0.0478	0.0217	0.0369
Leak rate from LEAPOR [kg/s]	0.0197	0.0046	0.0181	0.0452	0.0203	0.0208
Difference [%]	18.7	32.6	9.4	9.7	18.7	59.1

In the fatigue crack case, it is found that some leak rates calculated with LEAPOR are far from the measured mass flow rates, especially if the pressure and temperature are 62.1 bar and 161.8°C, respectively. When both pressure and temperature are at high levels, the simulated leak rate results are a bit higher than the measured ones. The leak rates are overestimated by the numerical method.

Table 3.33. PSI result of the real event analysis

Reference leak rate: 0.013 kg/s		Underestimation	Best-Estimate	Overestimation
Zero Bending	**Bending Moment [kNm]**	0	0	0
	Leak rate [kg/s]	0	0	0
Medium Bending	**Bending Moment [kNm]**	0.6	1.11	1.31
	Leak rate [kg/s]	0.00913	0.04613	0.05953
Large Bending	**Bending Moment [kNm]**	1.61	1.81	2.01
	Leak rate [kg/s]	0.08157	0.10893	0.12509

As LEAPOR code cannot deal with the variable bending moment, we can refer to the COD and leak rate calculation methods implemented into this code (Zahoor, see Section 2.2.1). Finally, we can conclude that the leak rate is regarded as zero when no bending moment is introduced. Hence, the best estimate lies on the applied medium bending moment range between 0.6 and 1.11 kNm, which causes the leak rate to approach the reference leak rate. It also reveals that the crack is closed without a bending moment.

Table 3.34. Result of the LBB sensitivity analysis

Local roughness		114 µm		17 µm	
Full crack length	**Crack open. displ.**	**Friction factor**	**Mass flow rate**	**Friction factor**	**Mass flow rate**
[mm]	[mm]	[-]	[kg/s]	[-]	[kg/s]
50	0.024	0.013361172	0.00195	0.009418383	0.00195
75	0.0368	0.013361172	0.00529	0.009418383	0.00533
100	0.0503	0.013361172	0.01075	0.009418383	0.01134
125	0.0649	0.013361172	0.01884	0.009418383	0.02211
150	0.0808	0.013361172	0.03009	0.009418383	0.03667
175	0.098	0.013361172	0.04499	0.009418383	0.05532
200	0.117	0.013361172	0.06443	0.009418383	0.07893
225	0.137	0.013361172	0.08845	0.009418383	0.1074
250	0.1595	0.013361172	0.11893	0.009418383	0.14331
275	0.183	0.013361172	0.15534	0.009418383	0.18439
300	0.209	0.013361172	0.20002	0.009418383	0.23477

As shown in Table 3.34, a higher local roughness increases the friction factor and as a result the mass flow rate is reduced. With an increase of the full crack length, the COD also increases, which results in the rise of the mass flow rate. The leak rate difference caused by different local roughness is bigger when the crack is longer. The conclusion is that the COD has more influence on the mass flow rate than the local roughness.

LEAPOR is a simple tool to simulate the leak rate. Therefore, external loadings are not considered as variables; only the definition of pressure and temperature is possible once the geometries and sizes of pipe and flaws are given.

3.2.9. SNC

For the *artificial slit* and *fatigue crack* exercise problems, the leak rate is estimated using LEAPOR (Section 2.5.4), SQUIRT (Section 2.5.8) and CFX's software (Section 2.5.1). In both SQUIRT and LEAPOR, the structure is considered a large diameter pipe (D>1000mm) instead of a plate and the COD is estimated from the crack length and cross sectional area, considering it was a rectangular shaped flaw. In SQUIRT, both ID and OD crack length are considered as average values of crack lengths provided in Table 3.1, while in LEAPOR, the actual crack lengths are used. For both these problems, CF is assumed in SQUIRT with crack morphology parameters from Table 3.9 of Reference [14]. Crack morphology parameter in Table 3.1 is used in LEAPOR.

In the CFX calculation, the flow inlet is modelled using the subsonic flow regime with "Total Pressure (stable)" option for mass and momentum setting. Medium turbulence (intensity = 5%) and the "Total Temperature" option are used for heat transfer setting. The flow outlet is modelled using the subsonic flow regime with "Average Static Pressure" option (pressure profile blend = 0.05) for mass and momentum setting. Pressure is considered averaging over the whole outlet. The pipe wall boundary is modelled using the "No Slip Wall" option for mass and momentum setting and the "Adiabatic" option for heat transfer setting. The "Rough Wall" option with different sand grain roughness is adopted.

The results of the *artificial slit* and *fatigue crack* exercise problems are presented in Table 3.35 and Table 3.36.

Table 3.35. SNC results of the artificial slit case

Data number	10	13	14	20	33	38
Pressure [bar]	45.2	70.3	75.2	35.4	48.6	10.4
Temperature [°C]	233.9	216.9	250.5	161.4	122.4	79.3
LEAPOR [kg/s]	0.0950	0.1580	0.1379	0.1245	0.1475	-
SQUIRT [kg/s]	0.0932	0.1535	0.1345	0.1202	0.1538	0.0711
CFX [kg/s]	0.1080	0.1360	0.1370	0.2000	0.2400	0.1116
Reference [kg/s]	0.122	0.201	0.183	0.166	0.214	0.104

When compared to the measured leak rate, both LEAPOR and SQUIRT underpredict the leak rate with a maximum absolute percentage difference of 46.3%. Since the temperature for data number 38 is low and it can be considered a single-phase flow, LEAPOR did not achieve a converged solution, and thus data number 38 is not considered in percentage difference calculations.

Ansys CFX overestimated the leak rate for three of the test data and underestimated it for the other three, with a maximum percentage difference of 47.8%.

<div align="center">**Table 3.36. SNC results of the fatigue crack**</div>

Data number	2	9	27	45	61	80
Pressure [bar]	65.7	20.8	70.7	76.7	77.2	62.1
Temperature [°C]	204.3	204.4	254.4	20.8	229.9	161.8
LEAPOR [kg/s]	0.0282	0.0078	0.0258	-	0.0290	0.0297
SQUIRT [kg/s]	0.0296	0.0083	0.0271	0.0463	0.0305	0.0312
CFX [kg/s]	0.0240	0.0120	0.0300	0.0380	0.0380	0.0372
Measured leak rate [kg/s]	0.016	0.0061	0.0164	0.0408	0.0165	0.0331

For the *fatigue crack*, in summary, all three methods overestimate the leak rate when compared to the measured one, except for data numbers 80 and 45 (CFX only). Due to the low temperature in data number 45 resulting in a single-phase flow, LEAPOR did not achieve a converged solution. The maximum absolute percentage differences for LEAPOR, SQUIRT and CFX are 58.3%, 45.9% and 56.6%, respectively.

The leak rate for the *real event* exercise problem is estimated with SQUIRT (Section 2.5.8) with crack morphology parameter of CF. An elliptical crack shape and an operating temperature of 40°C are assumed for the leak rate estimation in SQUIRT. For each level of bending moment, COD at mid-wall is estimated using an in-house solution. Mid-wall COD is assumed at both ID and OD surfaces.

The high bending moment was calculated using equation (9) in Article 3652 of ASME BPVC Section III using the Code value of design stress intensity of SA-312 Type 304. The medium bending moment was taken as half of the high bending moment, and the low bending moment was defined as zero. Results of the real event analysis are presented in Table 3.37.

<div align="center">**Table 3.37. SNC result of the real event analysis**</div>

Reference leak rate: 0.013 kg/s		**Best-estimate**
Zero Bending	**Bending Moment [kNm]**	0
	Leak rate [kg/s]	0.0294
Medium Bending	**Bending Moment [kNm]**	293.79
	Leak rate [kg/s]	0.2384
Large Bending	**Bending Moment [kNm]**	587.58
	Leak rate [kg/s]	1.87

For the real event analysis, even with zero bending moment, the predicted leak rate is above the measured leak rate of 0.013 kg/s. Uncertainty in temperature can be ignored as the given range of temperature from 40°C-70°C typically results in single-phase flow. Uncertainties in the crack morphology, COD solution and shape of the crack can be attributed to differences in the estimated leak rate.

Both SQUIRT and LEAPOR are used to estimate leak rates for LBB sensitivity analysis where COD was calculated using an in-house solution with weld material properties. As expected, the predicted leak rate is higher for lower local roughness parameters, but at a lower COD level, the leak rate is not sensitive to local roughness.

Table 3.38. SNC result of the LBB sensitivity analysis

Local roughness		114 μm				17 μm			
Full crack length	Crack open. displ.	SQUIRT		LEAPOR		SQUIRT		LEAPOR	
		Friction factor	Mass flow rate	Friction factor	Mass flow rate	Friction factor	Mass flow rate	Friction factor	Mass flow rate
[mm]	[mm]	[-]	[kg/s]	[-]	[kg/s]	[-]	[kg/s]	[-]	[kg/s]
50	0.0312		0.0029	0.92425	0.0025		0.0027	0.92425	0.0025
75	0.0485		0.0079	0.92425	0.0071		0.0073	0.84117	0.0073
100	0.0674		0.0163	0.92425	0.0144		0.0174	0.46856	0.0170
125	0.0888		0.0291	0.92425	0.0257		0.0323	0.32740	0.0316
150	0.1131		0.0474	0.92425	0.0419		0.0527	0.25528	0.0516
175	0.1413		0.0727	0.92425	0.0647		0.0804	0.21149	0.0787
200	0.1742		0.107	0.92425	0.0961		0.1173	0.18235	0.1148
225	0.2128		0.1546	0.92425	0.1386		0.1663	0.16171	0.1628
250	0.2583		0.2152	0.92425	0.1959		0.2313	0.14645	0.2263
275	0.3120		0.3068	0.60823	0.2862		0.3176	0.13484	0.3106
300	0.3754		0.4192	0.41379	0.4042		0.4328	0.12581	0.4230

In general, both LEAPOR and SQUIRT where able to predict the leak rates reasonably well; no consistent trend of overestimation or underestimation could be established and the results are very sensitive to the input parameters.

3.2.10. UJV

ÚJV analyses of the benchmark problems are done with the LeakH code (see Section 2.5.3) developed by ÚJV. Results are presented in the form of intervals corresponding to the COD scatter as defined in the input. Compliance between the measured and calculated flow rates is excellent, with a reasonable level of conservativity (lower values are conservative for LBB).

Table 3.39. ÚJV results of the artificial slit case

Pressure [bar]	Temperature [°C]	Measured mass flow rate [kg/s]	Numerical participant result [kg/s]
45.2	233.9	0.122	0.087 – 0.112
70.3	216.9	0.201	0.157 – 0.203
75.2	250.5	0.183	0.130 – 0.169
35.4	161.4	0.166	0.126 – 0.163
48.6	122.4	0.214	0.162 – 0.209
10.4	79.3	0.104	0.074 – 0.096

In the case of fatigue crack, the COD was defined by one value in the input, contrary to artificial crack, and therefore the calculated leak rate can be expressed by one value. The code LeakH was used in this calculation, as in the previous case. The results are shown in Table 3.40.

Table 3.40. ÚJV results of the fatigue crack

Pressure [bar]	Temperature [°C]	Measured mass flow rate [kg/s]	Numerical participant result [kg/s]
65.7	204.3	0.016	0.0317
20.8	204.4	0.0061	0.0105
70.7	254.4	0.0164	0.0248
76.7	20.8	0.0408	0.0425
77.2	229.9	0.0165	0.0314
62.1	161.8	0.0331	0.0347

The deviation between the model computation and the measurement is significantly larger than for the artificial slit case. In four cases, the computed leak rates are higher, while in two cases the measured values are practically identical with the calculated values.

In the real event analysis, low, medium and high bending moments were defined as 0 Nm, 40% of maximum allowable stress and 80% of maximum allowable stress of uncracked pipe. The maximum allowable stress was calculated according to the Czech code A.S.I. Only the best estimated value was calculated for both 40°C and 70°C. The COD was calculated according to Akram Zahoor Ductile Fracture Handbook (Section 2.2.1). One roughness of 7.6 µm was used. The computed values are shown in Table 3.41.

Table 3.41. ÚJV results of the real event analysis

Bending moment [kNm]	COD [mm]	Leak rate [kg/s]	
		40°C	70°C
0	0.075	0.159	0.158
0.187	0.597	1.79	1.77
0.374	2.021	6.19	6.14

The detected leakage of 0.013 kg/s is lower than the minimum calculated leakage corresponding to zero bending moment. This may be due to the effect of plugging. The effect of plugging is higher for lower COD. The influence of temperature is negligible.

Results of LBB sensitivity tasks are presented in Table 3.42 below. LEAKH is not able to calculate local surface roughness, only a global one can be entered as input. Instead of influence of roughness, the influence of type of turnings (either 90° or 45°) is considered. The COD was calculated according to the Akram Zahoor Ductile Fracture Handbook (see Section 2.2.1). The number and type of turning are crucial for LBB analysis, as seen in Table 3.42.

Table 3.42. ÚJV results of the LBB sensitivity analysis

Number of turns		90° turns 240	45° turns 240
Full crack length	**Crack open. displ.**	**Mass flow rate**	**Mass flow rate**
[mm]	[mm]	[kg/s]	[kg/s]
50	0.12008	0.00313	0.0232
100	0.306417	0.0365	0.377
150	0.60296	0.162	1.79
200	1.110101	0.473	5.39
250	2.002956	1.22	13.8
300	3.622305	3.48	37.9

3.3. Comparison

3.3.1. Artificial slit

In total, 12 contributions were received for the computation of the mass flow rates through artificial slits. The received computations and the reference values are shown in Figure 3.9. The tests were of data set numbers 10, 13, 14, 20, 33 and 38, and were numbered consecutively.

Figure 3.9. Left: Comparison of the calculated leak rates (coloured) with the reference (black). Right: The test conditions in the pT-diagram of water
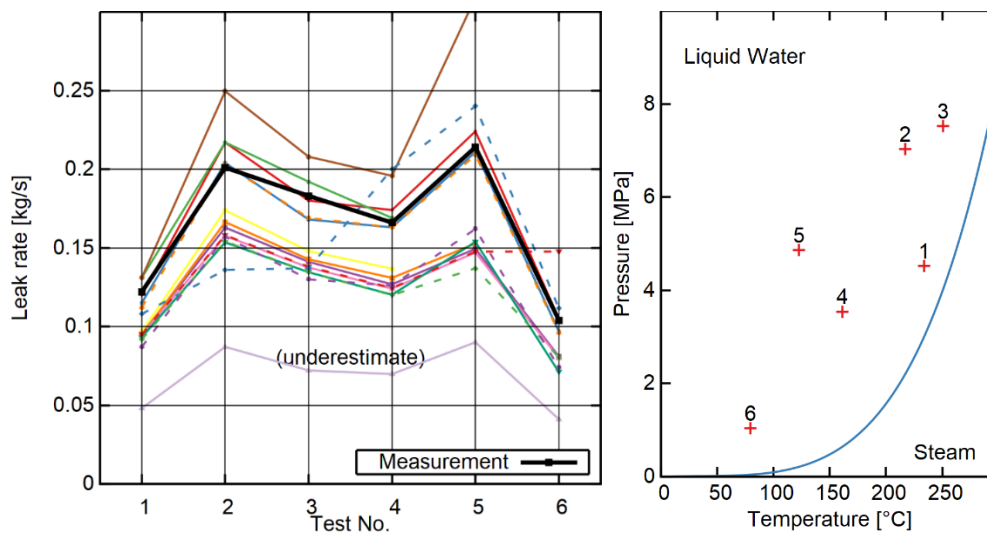
From this figure, it can be confirmed that most methods have a good qualitative agreement with the relation between thermodynamic conditions and mass flow rate. All except one are carried out as a best-estimate analysis, while one analysis is done as an underestimation (which consistently reports the lowest rates well below the measured values). For an understanding of the different approaches among the participants, a classification of the contributions is proposed.

Figure 3.10 shows which geometrical information is used by each participant, since the exercise table provides information about the inlet and the exit. In this graph, it is visible that the participants that use both sides are the largest group. Only one participant uses the COD specification as geometry information, which leads to significant differences to the other teams. Thus, the different choice in geometric information can be identified as a possible reason for a different leak rate prediction.

Figure 3.10. Analysis results for the artificial slit with emphasis on the leak geometry
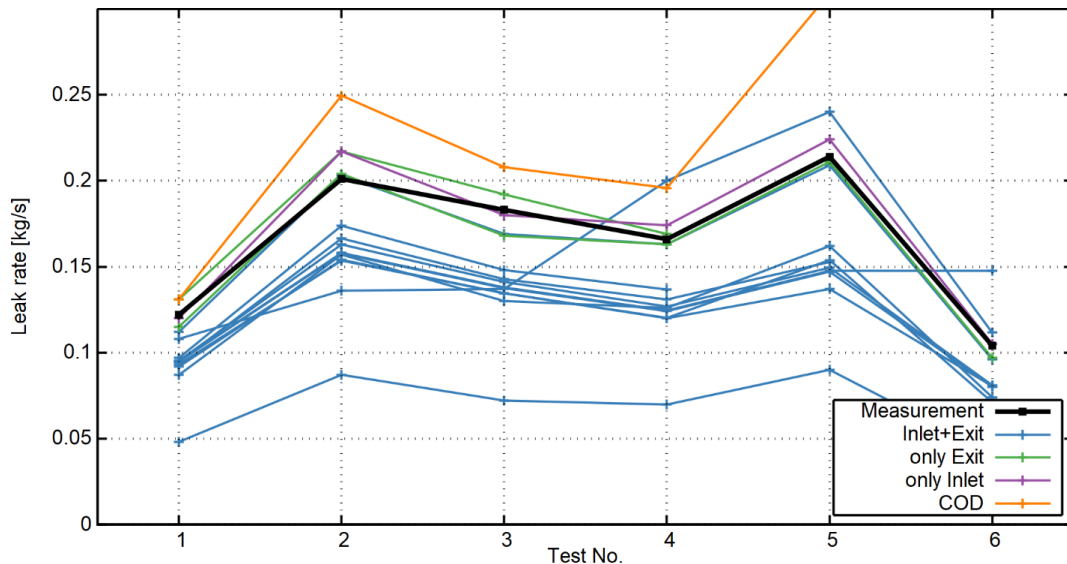
The second evaluation is done with respect to the friction and resistance model. There are different approaches: One fraction is computing a friction factor based on the morphology (roughness) information using a relation as the one by Paul et al., John et al., or KTA 3206. Two contributions use the single-phase flow resistance measured for the leak. One contribution assumes only a form loss coefficient and no frictional loss. In two contributions, the treatment of flow resistance cannot be well separated from the approach. The comparison of all approaches is shown in Figure 3.11.

Figure 3.11. Influence of friction modelling to the leak rate computation
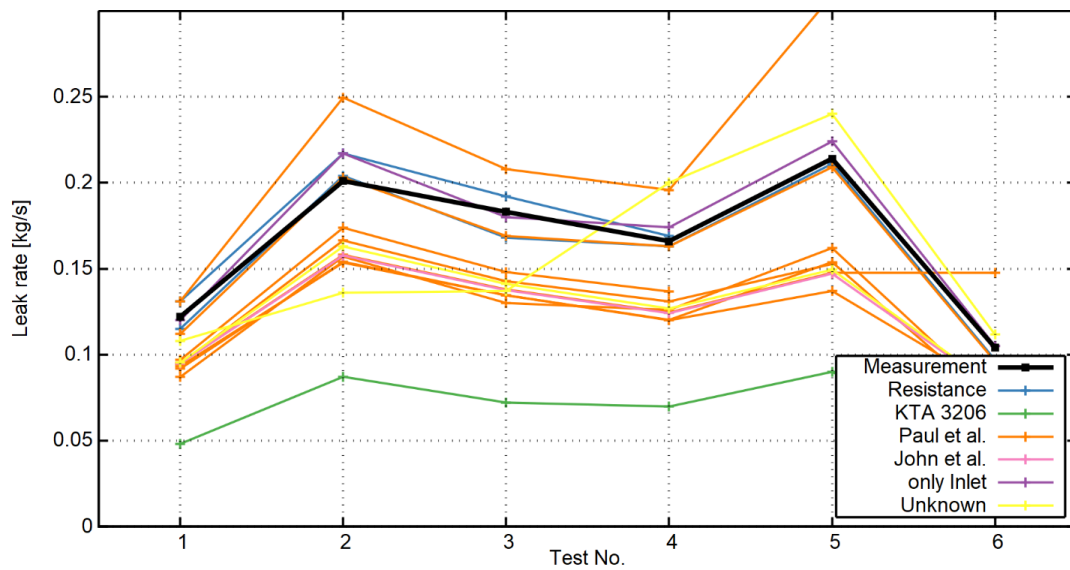
From this figure, it seems to be clear that the use of the actual resistance value yields a higher accuracy than the use of the morphology. The result for the inlet loss is also very good in this case. The use of the KTA 3206 relation is the key to obtaining the underestimating trend in this result, which is well achieved.

The third classification is the actual flow model, which describes the evolution of thermodynamical properties of water along the flow channel. The models according to Henry and Pana, a homogenous equilibrium approach, the modified Bernoulli equation, a computational fluid dynamic (CFD) approach, the CDR model, and the model from Zaloudek are used. A classification according to the actual flow model in the simulation is applied in Figure 3.12.

Figure 3.12. Evaluation of flow models in the artificial slit exercise
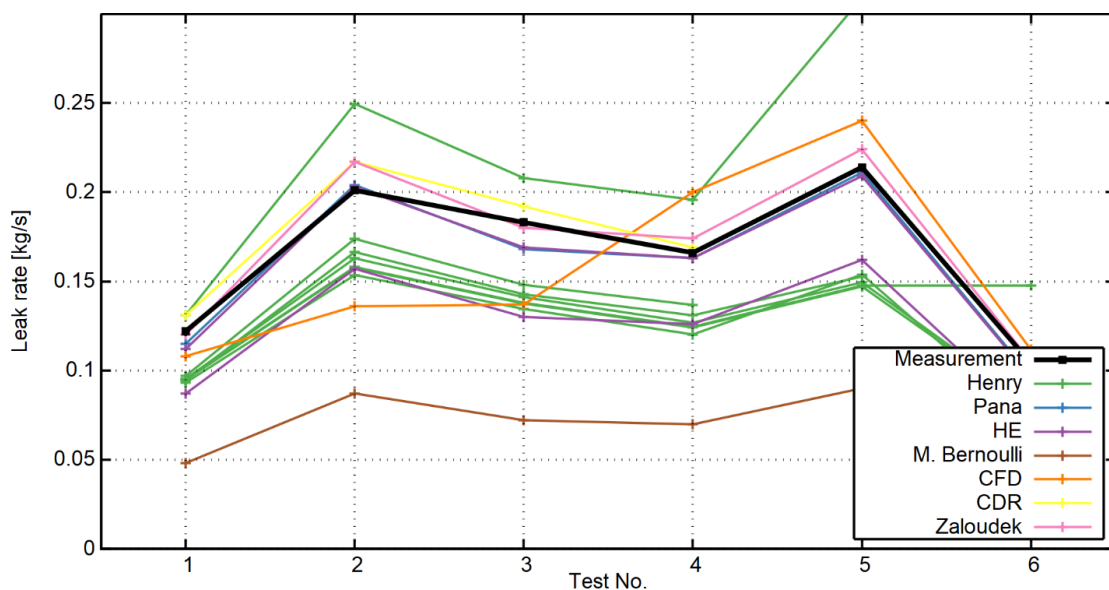
It is evident from this figure that the grouping influenced by the aforementioned geometry and resistance assumptions remains. The grouping of the Henry-like models with accurate cross-section and roughness-determined resistance is clearly visible. Compared with the other contributions, they do not have the highest accuracy, but rather show a trend to smaller leakage rates. To separate the flow model influence from geometrical and resistance assumptions, the dependency of the leak rate on the test number (i.e. from thermodynamic conditions) is a good measure. Most model computations (despite outliers) follow the measured trend, with the notable exception of the CFD contribution (test No. 3 and 4).

3.3.2. Fatigue crack

The 12 contributions for the fatigue crack are shown in Figure 3.13. One is an underestimating analysis, while all others are best-estimate analyses. As before, the tests are numbered consecutively.

Figure 3.13. Phase 1 fatigue crack result
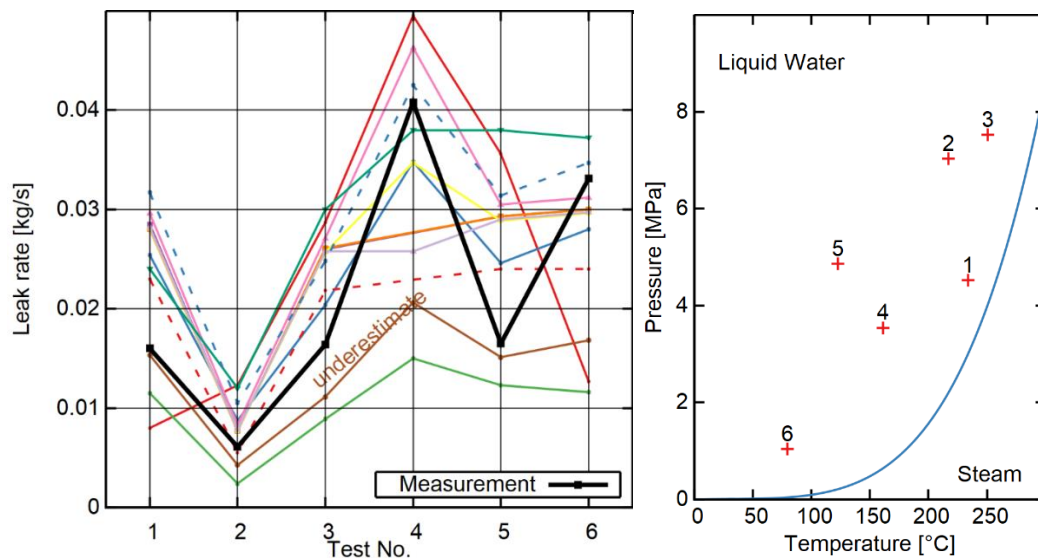
The differences between measured and computed values are satisfying; the worst examples differ by about a factor of 2. The underestimating analysis is below the measured values, but not the lowest of all.

The friction and resistance assumption are important building blocks of the analysis. In the assessment of the fatigue crack, different levels of information can be used:

- the fact that it is a fatigue crack and assuming standard values for the morphology;
- the measured surface roughness as morphology, and computing the friction factor by standard relations;
- the measured resistance as obtained in cold flow tests.

The classification according to this scheme is visualised in Figure 3.14.

Figure 3.14. Resistance classification for fatigue crack exercise
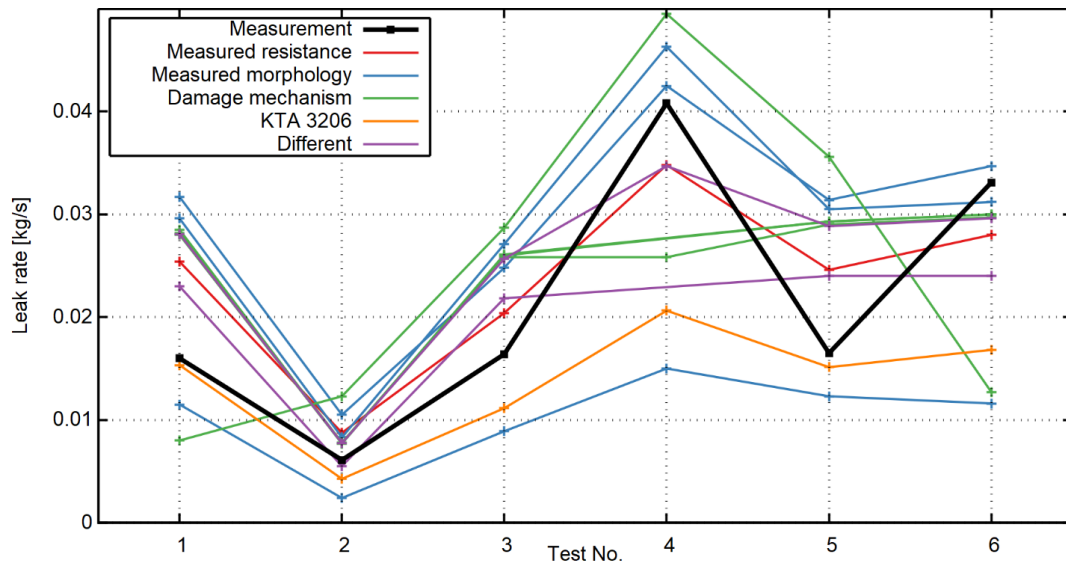
The use of the measured resistance leads to a good agreement between computation and measurement, but some of the results based on the measured morphology are of similar precision. The results based on the damage mechanism show a lower accuracy. The underestimating contribution is based on the conservative computation of the resistance and is therefore shown as a particular class (KTA 3206).

The influence of the flow model is discussed with help of Figure 3.15. Most of the participants use implementations of the Henry model – the users of the LEAPOR implementation are shown as a class of their own. The other participants use the Pana model, a homogeneous equilibrium approach, or the modified Bernoulli approach.

Figure 3.15. Flow model analysis for fatigue crack case
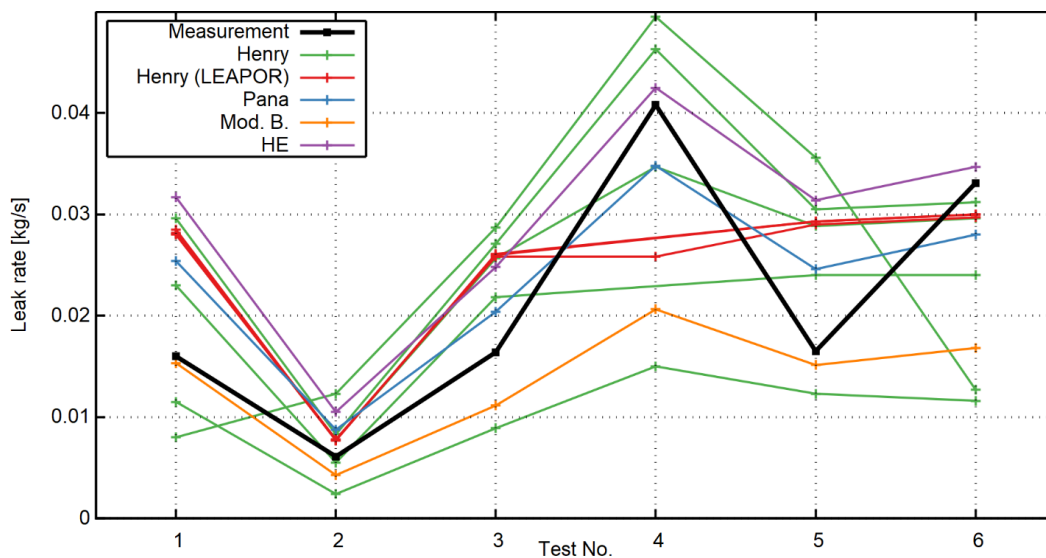
Test No. 4 is a cold water test, and several Henry model implementations fail to treat (or catch) this case correctly, mostly skipping the value (note the missing points in the diagram). The modified Bernoulli approach is not appropriate for the cold flow test either;

consequently, the behaviour at that point is of minor quality. However, the modified Bernoulli equation, the homogeneous equilibrium approach and the Pana model are the only models in the contributions that show the correct qualitative trend for all points – many Henry models fail to predict the increase in leak rate between point 5 and 6.

3.3.3. Real event

For the analysis of the real event, the task was to estimate the unknown bending acting on a circumferential crack, and to perform a sensitivity study with different bending assumptions. Fourteen different computations were received: nine best-estimate analyses, three under-estimations and two over-estimates. The predicted leak rates for the individual bending moment assumptions as chosen by each participant are shown in Figure 3.16.

Figure 3.16. Phase 1 real event
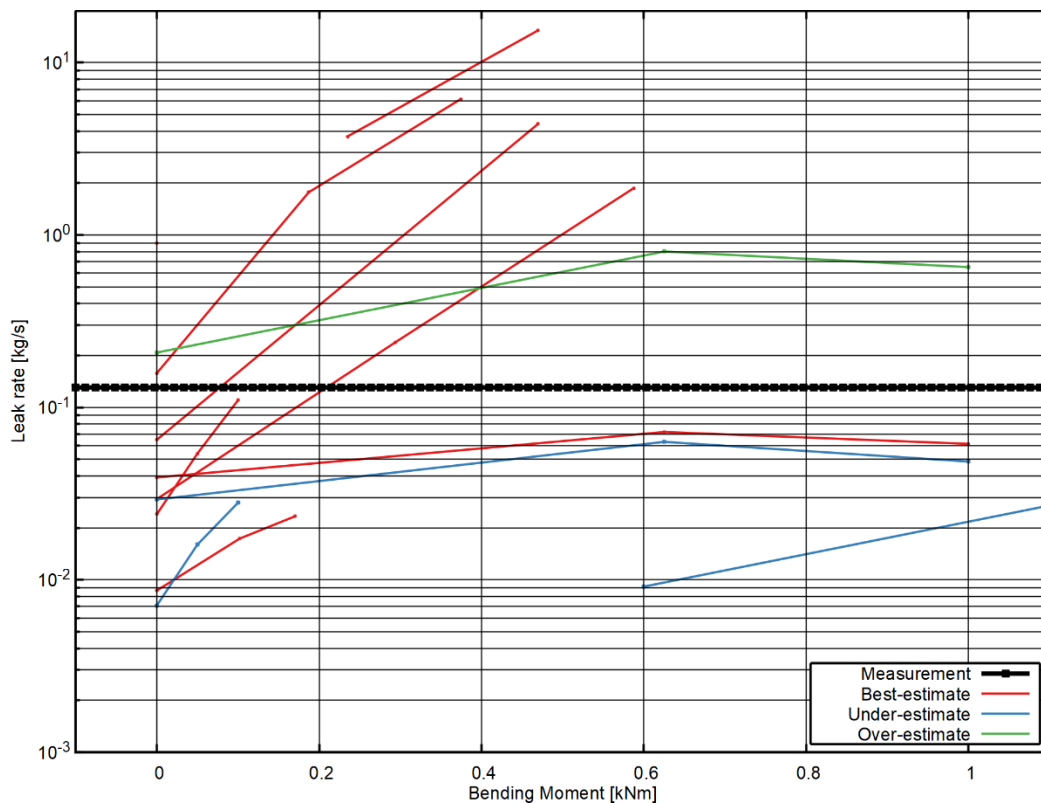
The under-estimates are significantly lower than the over-estimates, but the best-estimates range from very low to very high values. While the participants' assumptions of the realistic bending moment are in good agreement (between 0.1 and 1.0 kNm), the leak rates vary by three orders of magnitude.

One important assessment step is the computation of the leak opening, as manifested in the COD. Most participants use the GE/EPRI method from the ductile fracture handbook, and another significant group uses the elastic version of this method. One participant uses the LBB-ENG2-method and one (under-estimate) uses the GRS-PB method; other participants are not reporting the (intermediate) COD values and are thus not included in the comparison in Figure 3.17.

Figure 3.17. Phase 1 real event: COD analysis by method
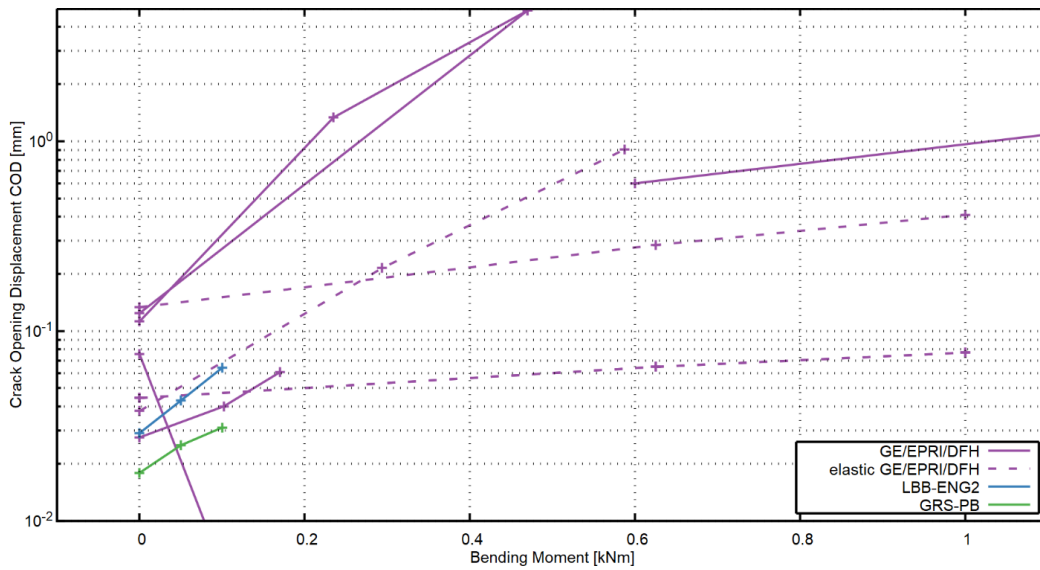
The figure shows that the COD values differ greatly. The elastic methods show an affine-linear dependence of the COD with the applied bending, as expected. As the material properties are not proposed, the contributions based on the same methods are not necessarily identical.

3.3.4. LBB sensitivity

In the analysis of the LBB sensitivity, eight contributions were received. As this analysis involves the whole computation from crack opening to mass flow (see Section 2), it is preferable to compare the results of intermediate steps. The first step, the computation of the COD as a function of crack length, is shown in Figure 3.18. The different contributions rely mostly on the ductile fracture handbook solution (GE/EPRI), its derivate LBB.ENG2 and the elastic approximation. The method of the xLPR code is also used in the contributions.

Figure 3.18. Phase 1 LBB sensitivity study crack opening displacement as a function of full crack length
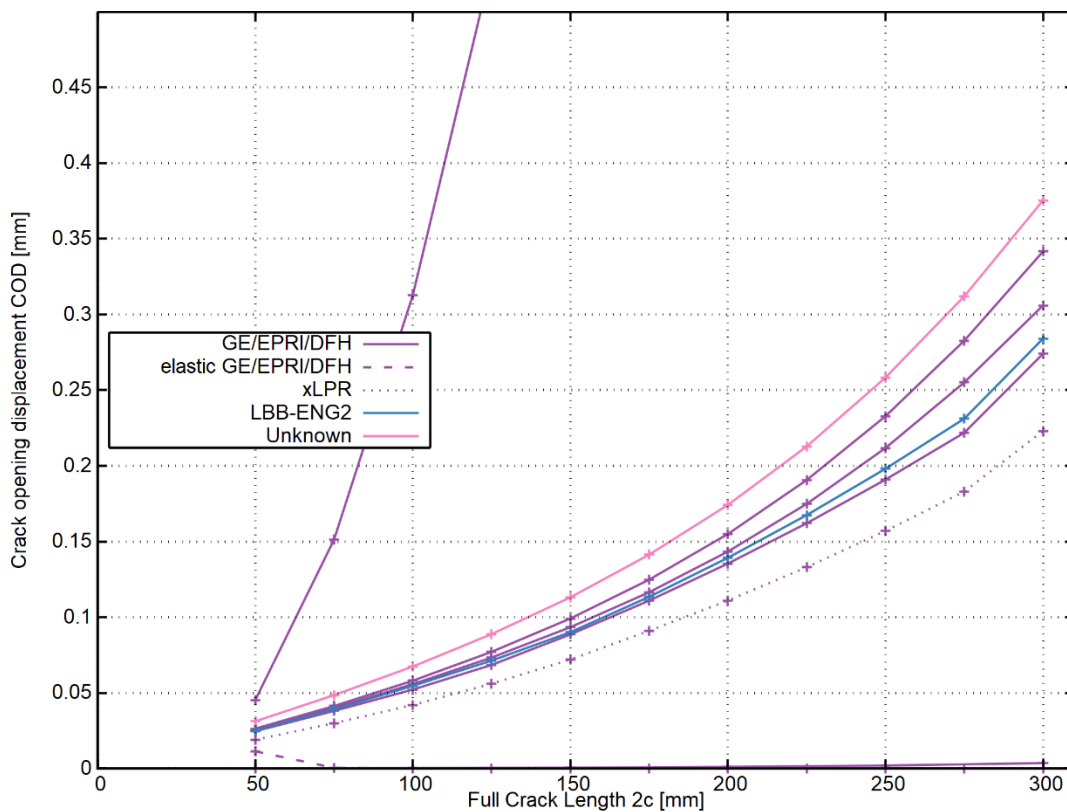
Most methods are in good agreement with each other, with two notable exceptions: The SQUIRT-implementation of the elastic EPRI method predicts a shrinking COD with increasing crack length, and one participant reports a very steep increase of the COD compared with the others.

The next step is assessing the friction factor as a function of the COD. All participants refer to the friction factor relation according to Paul et al., so it is not necessary to distinguish between the models. Unfortunately, only five participants reported this value in their contributions, so only those values are included in the comparison of models shown in Figure 3.19. Solid lines indicate the assumption of 114 µm local roughness, while dashed lines correspond to 17 µm.

Figure 3.19. Friction factor as a function of the crack opening displacement
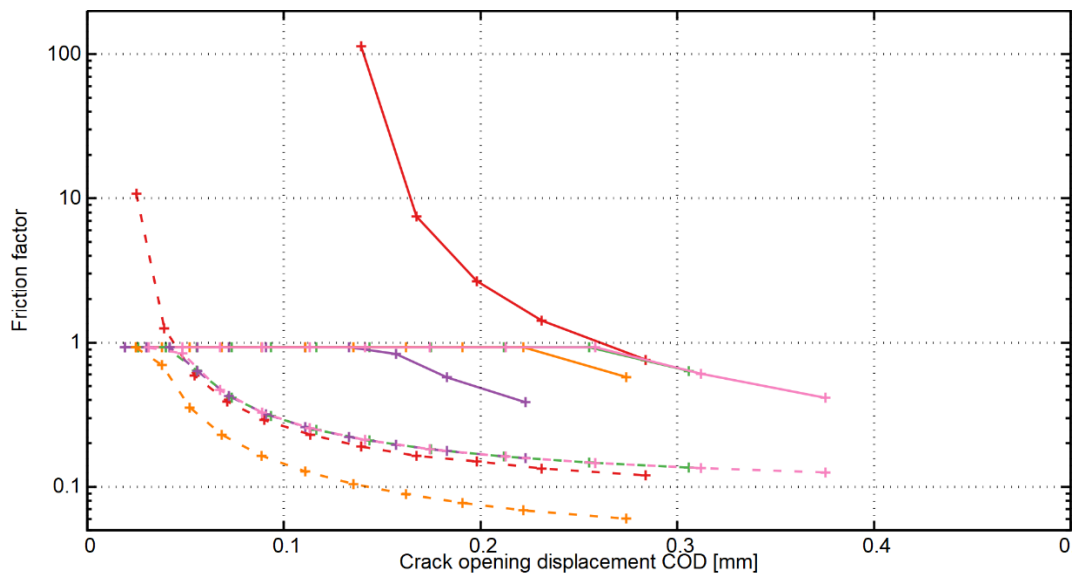
The results for 17 µm are in reasonable agreement, while the results for 114 µm differ significantly. In addition, all but one of the participants assume a saturation of the friction factor, i.e. the value is limited to unity, while the value is not truncated for the single participant.

The last step in the assessment is the computation of the leak flow rate for a given crack opening. This is clearly influenced by the friction factor modelling, as discussed above. The participants' results are compared in Figure 3.20. The line styles are identical to the ones in the previous figure.

Figure 3.20. Mass flow rate as a function of crack opening displacement
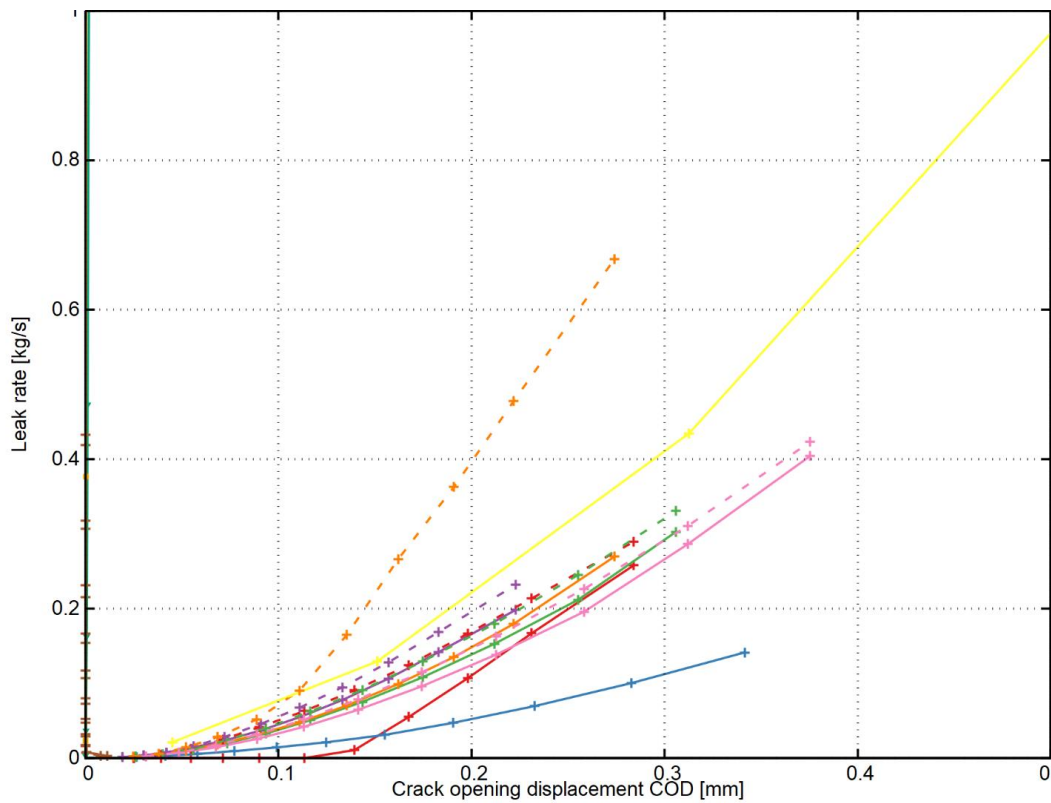
Many mass flow rate computations for a given COD coincide, resulting in similar COD computations and similar friction factors. The exceptions discussed previously can be identified in this figure as well. The small values of one solid curve, leading to very small values of leak rates for finite crack openings of about 0.1 mm, are a result of the diverging friction factor.

4. Second benchmark phase

The second benchmark phase was started after the results of the first benchmark phase were discussed. The computational phase was prolonged in order to allow blind computations even in case of delayed contributions.

4.1. Exercise set

4.1.1. Blind calculation of artificial slit

The exercise sheet for the blind calculation is given in Table 4.1. This test was done in analogy to the artificial slit test described in the first benchmark phase (Section 3.1.1), but with different specimen dimensions.

Table 4.1. Exercise sheet for the blind calculation of artificial slit

Category	Attribute		Variable	Value	Unit
Structure	Geometry type		-	Plate	-
	Wall thickness		t	16.85	mm
	Additional loads				
Leak geometry	Approximate shape		-		-
	Interior	Full length	2c	20.5	mm
		Maximal width	COD	138-158-147	µm
		Cross section	COA	3.08	mm²
	Exterior	Full length	2c	20.9	mm
		Maximal width	COD	211-213-204	µm
		Cross section	COA	4.39	mm²
Morphology	Damage mechanism		-	Eroded slit	-
	Inlet form loss		zeta_in	Unknown	-
	Roughness	Local	Rz	Unknown	µm
		Global	Rz	22	µm
	Bends	Local	N	Unknown	-
		Global	N	Unknown	-
	Measured total resistance		Zeta	4.56	-
Fluid (stagnation)	Pressure		p	variable	bar
	Temperature		T	variable	°C

The pressure and temperature variations are given in Table 4.2.

Table 4.2. Pressure and temperature variation of the blind artificial slit case

Test No.	1	2	3	4	5	6
Data set	8	15	18	38	40	55
Pressure [bar]	60.4	10.5	45	45.4	63.6	25.5
Temperature [°C]	19.9	122.1	122.3	234.6	213	206.1

4.1.2. Blind calculation of fatigue crack

The blind computation of a fatigue crack is the continuation of the first benchmark phase fatigue crack computation. The data sheet is reproduced in Table 4.3.

Table 4.3. Exercise sheet for the blind calculation of fatigue crack

Category	Attribute		Variable	Value	Unit
Structure	Geometry type		-	Plate	-
	Wall thickness		t	7.05	mm
	Additional loads			None	
Leak geometry	Approximate shape		-	Rectangular	-
	Interior	Full length	2c	52	mm
		Maximal width	COD	94	µm
		Cross section	COA	4.89	mm²
	Exterior	Full length	2c	41.05	mm
		Maximal width	COD	84	mm
		Cross section	COA	3.45	mm²
Morphology	Damage mechanism		-	Fatigue	-
	Inlet form loss		zeta_in	Unknown	-
	Roughness	Local	Rz	Unknown	µm
		Global	Rz	40	µm
	Bends	Local	N	Unknown	-
		Global	N	Unknown	-
	Measured total resistance		Zeta	ca. 32	-
Fluid	Pressure		p	variable	bar
	Temperature		T	variable	°C

The pressure- and temperature variation is in the same range as for the artificial slit case and the first phase exercises. The six selected points are shown in Table 4.4.

Table 4.4. Pressure and temperature variation for the blind calculation of fatigue crack

Test No.	1	2	3	4	5	6
Data set	31	18	32	13	44	49
Pressure [bar]	75.3	65.5	15.7	45.4	50.6	30.1
Temperature [°C]	199.4	234.8	200	238	16.7	151.9

4.1.3. Blind calculation of real event analysis

The blind calculation of a real event proposes the computation of an axial crack in a reducer. The data sheet is shown in Table 4.5.

Table 4.5. Exercise sheet for the blind calculation of real event

Category	Attribute		Variable	Value	Unit
Structure	Geometry type		-	Reducer (3 inch to 2 inch)	-
	Outer diameter		D	75 to 50	mm
	Wall thickness		t	12	mm
Material	Number			AISI type 304	-
	Young's Modulus		E	Unknown	MPa
	Yield stress		Rp0,1	Unknown	MPa
	Ultimate stress		Rm	Unknown	MPa
	Poisson number		nu	Unknown	-
	Ramberg-Osgood	Prefactor	alpha	Unknown	
		Exponent	n	Unknown	
Loads	Pressure		p	7	MPa
	Bending		M	Unknown	Nm
Leak geometry	Orientation		-	Axial	-
	Approximate shape		-	Wall	-
	Interior	Full length	2c	Unknown	mm
		Estimated maximal width	COD	Unknown	mm
		Cross section	COA	Unknown	mm²
	Mean	Full length	2c	Unknown	mm
		Estimated maximal width	COD	Unknown	mm
		Cross section	COA	Unknown	mm²
	Exterior	Full length	2c	<25	mm
		Estimated maximal width	COD	Unknown	mm
		Cross section	COA	Unknown	mm²
Morphology	Damage mechanism		-	Thermal fatigue	-
	Inlet form loss		zeta_in	Unknown	-
	Average roughness	Local	Rz	Unknown	µm
		Global	Rz	Unknown	µm
	Mean roughness		Ra	Unknown	
	Maximal roughness		Rt	Unknown	
	Bends	Local	N	Unknown	-
		Global	N	Unknown	-
	Measured total resistance		Zeta	Unknown	-
Fluid	Pressure		p	7	MPa
	Temperature		T	280	°C
Leak rate	Measured flow rate		m	(blind)	kg/s

Since this evaluation is only done with one single measured value, it is proposed to make a best estimate, an underestimation and an overestimation analysis.

4.1.4. LBB sensitivity analysis

The finding of the parallel LBB benchmark activity, that the computed leak opening has a strong effect on the leak rate, motivated the analysis of a past experiment on COD.

Table 4.6 summarises the test conditions of a pipe with a circumferential flaw under interior pressure and a variable bending load.

Table 4.6. Exercise sheet for the LBB sensitivity analysis

Category	Attribute		Variable	Value	Unit
Structure	Geometry type		-	Cylinder	-
	Outer diameter		D	796	mm
	Wall thickness		t	47.3	mm
	Type		-	NiMoCr-Cast	-
Material	Yield strength		Rp02	479.6	MPa
	Ultimate tensile strength		Rm	663	MPa
	Elastic modulus		E	196	GPa
	Poisson number		nu	0.3	-
	Ramberg-Osgood		σ_o	479	MPa
			ε_o	0.02	-
			α	3.9	-
			n	6	-
Loads	Interior pressure		p	15.8	MPa
	Temperature		T	140	°C
	Bending moment		M	Variable	MNm
Leak geometry	Orientation		tial		-
	Approximate shape		-		-
	Centre	Full length	2c	417	mm
		Full angle	2 gamma	63.8	°

The change in COD as the bending moment increases was measured in the test and computed by the participants. The measured dCOD values are shown in Table 4.7.

Table 4.7. Bending moment and resulting crack opening for the LBB sensitivity analysis

Bending moment M [MNm]	Crack opening displacement change dCOD [mm]
0.00	0.00
0.55	0.23
0.98	0.38
1.47	0.48
2.00	0.64
2.51	0.86
2.92	1.08
3.43	1.44
4.00	1.79
4.49	2.53
5.08	3.52
5.45	5.08

The dCOD value is defined to be zero at vanishing bending; due to the test conditions, a crack opening solely due to pressure is not relevant for this exercise.

4.1.5. Steam generator tube leak analysis

This exercise is different from the others, since a very thin test specimen with a leak is investigated. The test was also conducted at MPA University of Stuttgart, and the test conditions are summarised in Table 4.8.

Table 4.8. Exercise sheet for the SGT analysis

Category	Attribute		Variable	Value	Unit
Structure	Geometry type		-	Plate	-
	Wall thickness		t	1.23	mm
Leak geometry	Approximate shape		-	Circle	-
	Interior	Diameter	D	0.3	mm
		Cross section	COA	0.0707	mm²
	Exterior	Diameter	D	0.3	mm
		Cross section	COA	0.0707	mm²
Morphology	Damage mechanism		-	Eroded hole	-
	Inlet form loss		zeta_in	Unknown	-
	Roughness	Local	Rz	Unknown	µm
		Global	Rz	7.4	µm
	Bends	Local	N	Unknown	-
		Global	N	Unknown	-
	Measured total resistance		Zeta	Unknown	-
Fluid	Pressure		p	variable	MPa
Stagnation			T	variable	°C

As in the cases of the artificial slit tests and the fatigue crack tests, six fluid conditions are selected. The test conditions are summarised in Table 4.9.

Table 4.9. Pressure and temperature variation for the SGT analysis

Data number	10	13	19	20	22	24
Pressure [MPa]	7.59	2.09	8.08	5.55	6.54	7.45
Temperature [°C]	16.7	128.6	128.9	263.1	262.9	262.8

It was left to the discretion of the participants whether these tests were to be assessed with the same methods used for thick-walled components or with specific methods for steam generator tube leaks.

4.2. Computation

In this section, the individual participants' contributions are documented and shortly discussed. The subsections are arranged according to the participants' organisations.

4.2.1. BARC

BARC used the SCALE code (see Section 2.5.7) for the assessment; the Burnell model (Section 2.4.3), the Zaloudek model (Section 2.4.6) and the Henry model (Section 2.4.4) are compared. The results for the artificial slit cases are summarised in Table 4.10.

Table 4.10. BARC results of the artificial slit case

Data number		8	15	18	38	40	55
Pressure	[bar]	60.4	10.5	45.0	45.4	63.6	25.5
Temperature	[°C]	19.9	122.1	122.3	234.6	213	206.1
Burnell	[kg/s]	0.195	0.073	0.161	0.107	0.161	0.082
Zaloudek	[kg/s]	0.186	0.067	0.151	0.084	0.145	0.062
Henry	[kg/s]	0.220	0.024		0.123		0.091

The fatigue crack case is analysed with the same methods. The BARC result for this case is given in Table 4.11.

Table 4.11. BARC results of the fatigue crack case

Data number		31	18	32	13	44	49
Pressure	[bar]	75.3	65.5	15.7	45.4	50.6	30.1
Temperature	[°C]	199.4	234.8	200	238	16.7	151.9
Burnell	[kg/s]	0.209	0.165	0.053	0.115	0.119	0.138
Zaludek	[kg/s]	0.192	0.142	0.010	0.087	0.189	0.127
Henry	[kg/s]	0.086	0.082	0.038	0.128	0.224	0.033

4.2.2. GRS

As the organiser of the benchmark exercises, GRS was involved in the selection of the individual problem sets and the preparation of the descriptions. Therefore, GRS's analyses of the fatigue crack, the artificial slit and the real event are not performed as blind computations.

In the LBB sensitivity analysis, two analytical methods are chosen for the computation of the incremental COD change: the underestimating GRS-PB approach (see Section 2.2.3) and the best-estimate LBB.ENG2 approach (see Section 2.2.4). While the latter considers a Ramberg-Osgood material stress-strain relation, the plastic strain parts of GRS-PB are more qualitative and, in addition, conservative. The result is shown in Table 4.12; the dCOD values were obtained by considering the COD at zero bending moment.

Table 4.12. GRS' result of the LBB sensitivity analysis

Bending moment	Underestimating (GRS-PB)		Best-Estimate (LBB.ENG2)		
	Total COD	dCOD	Total COD	dCOD	Measured dCOD
[MNm]	[mm]	[mm]	[mm]	[mm]	[mm]
0	0.37	0.00	0.37	0.00	0.00
0.55	0.52	0.15	0.55	0.17	0.23
0.98	0.64	0.27	0.68	0.31	0.38
1.47	0.77	0.40	0.84	0.46	0.48
2.00	0.92	0.55	1.00	0.63	0.64
2.51	1.06	0.69	1.16	0.79	0.86
2.92	1.17	0.80	1.29	0.92	1.08
3.43	1.31	0.94	1.45	1.08	1.44
4.00	1.46	1.09	1.63	1.26	1.79
4.49	1.60	1.23	1.79	1.42	2.53
5.08	1.76	1.39	1.97	1.60	3.52
5.45	1.86	1.49	2.09	1.72	5.08

The conservative dCOD computation is well below the measurement. In the more elastic regime up to about 3 MNm bending moment, the best-estimate values and the measurement are in sufficient agreement, but at larger bending moments, the non-linearity of the dCOD cannot be predicted quantitatively by the analytical method.

The steam generator tube leak case computation is based on the Pana model, but it is questionable if such an equilibrium two-phase flow model is appropriate here, since it cannot be expected that the phase transition in this very short channel is in equilibrium. The computed values are shown in Table 4.13.

Table 4.13. GRS' result of the SGT analysis

Pressure	[MPa]	7.59	2.09	8.08	5.55	6.54	7.45
Temperature	[°C]	16.7	128.6	128.9	263.1	262.9	262.8
Measured leak rate	[g/s]	6.43	3.00	6.31	3.70	4.12	4.57
Computed leak rate	[g/s]	6.6	3.2	6.6	2.1	2.7	3.4

It can be seen that the accuracy is good for low temperature discharge, but the real leak rate is significantly underestimated for high temperatures, when evaporation is expected. This underlines the importance of the effect of a correct phase transition model for short orifice leaks.

As a conclusion from this second phase, the LBB sensitivity exercise showed that analytical methods for the computation of the CODs have inevitable accuracy limitations, especially when leaving the elastic regime. For higher accuracy levels, an analysis with Finite Elements Analysis (FEA) would be a better choice. However, conservative underestimation can be achieved with this approach. The steam generator tube case is a

good demonstration that LBB-related methods assuming friction and evaporation have their limitations for thin-walled specimens, and tailored suitable methods are required here.

4.2.3. KINS

KINS' analyses of the benchmark problems were performed using a LEAPOR code developed by Oak Ridge National Laboratory (see Section 2.5.4). LEAPOR is based on the modified Henry-Fauske model for the thermo-hydraulic calculation (Section 2.4.4).

The wall thickness, full lengths of the crack at both interior and exterior, COD values measured at three different positions, and COA were provided for the artificial slit case. The wall thickness and full lengths were employed for the analysis, and the COD values at both interior and exterior were assumed to be 0.148 and 0.209 mm, respectively, so that the calculated cross section is the same with the provided COA. For crack morphology parameters, both local and global roughness were assumed to be 22 μm, and local and global path deviations of 1.1 were applied. The calculated values are summarised in Table 4.14.

Table 4.14. Results of the artificial slit case calculated by KINS

Data number		8	15	18	38	40	55
Pressure	[bar]	60.4	10.5	45	45.4	63.6	25.5
Temperature	[°C]	19.9	122.1	122.3	234.6	213	206.1
Computed leak rate	[kg/s]	0	0.0507	0.1069	0.0637	0.1175	0.0406

In case of the fatigue crack analysis, global roughness was provided, and the statistical local roughness value of 8.814 μm was adopted according to Rahman's research [14]. Local and global path deviations were assumed to be 1.017 and 1.06, respectively [14]. As shown in Table 4.15, LEAPOR treats all cases except the case of low pressure and temperature (data number 44).

Table 4.15. Results of the fatigue crack estimated by KINS

Data number		31	18	32	13	44	49
Pressure	[bar]	75.3	65.5	15.7	45.4	50.6	30.1
Temperature	[°C]	199.4	234.8	200	238	16.7	151.9
Computed leak rate	[kg/s]	0.0543	0.045	0.008	0.0284	-	0.036

The real event analysis includes the calculation of COD with limited material properties. The elastic-plastic COD estimation of the GE/EPRI ductile fracture handbook (see Section 2.2.1) requires the Ramberg-Osgood parameter. R-O fit, proposed by Kim et al. [33], was employed using the material properties given. R-O parameters (α, n) can be determined as follows when considering only yield ($\sigma_{0.2}$) and tensile strength (σ_u):

$$\alpha = \frac{0.002E}{\sigma_{0.2}}$$

$$\frac{1}{n} = 0.629 - 1.536\left(\frac{\sigma_{0.2}}{\sigma_u}\right) + 1.723\left(\frac{\sigma_{0.2}}{\sigma_u}\right)^2 - 0.814\left(\frac{\sigma_{0.2}}{\sigma_u}\right)^3$$

Based on this approach, α and n were determined to be 1.76 and 5.48, respectively. The opening displacement of the crack with a length of 25 mm was obtained using R-O parameters. The statistical local roughness value of 8.814 μm and global roughness value of 40.51 μm were adopted according to Rahman's research [14]. Local and global path deviations were assumed to be 1.017 and 1.06, respectively [14]. The computed COD and leak rate are shown in Table 4.16.

Table 4.16. Result of the real event analysis calculated by KINS

Best-estimate	
Crack opening displacement [mm]	Leak rate [g/s]
0.01429	0.5

In the LBB sensitivity analysis, participants were required to calculate the crack opening by using incrementally increased bending moment. As stated in the previous exercise, the GE/EPRI elastic-plastic analytical method was used to calculate the COD. Table 4.17 shows the dCOD values obtained by considering the COD at zero bending moment.

Table 4.17. Result of the LBB sensitivity analysis estimated by KINS

Bending moment	Computed COD		Measured dCOD
	Total COD	dCOD	
[MNm]	[mm]	[mm]	[mm]
0	0.37	0.00	0.00
0.55	0.55	0.18	0.23
0.98	0.70	0.32	0.38
1.47	0.86	0.49	0.48
2.00	1.06	0.69	0.64
2.51	1.26	0.89	0.86
2.92	1.44	1.07	1.08
3.43	1.70	1.33	1.44
4.00	2.07	1.69	1.79
4.49	2.47	2.09	2.53
5.08	3.13	2.76	3.52
5.45	3.68	3.31	5.08

Overall, the calculation of dCOD shows a good agreement compared to the measured dCOD up to about 4 MNm of bending moment. The GE/EPRI method, however, underestimates the dCOD at the larger bending moments.

In the case of the steam generator tube leak, participants were required to predict the leak rate through the hole with a diameter of 0.3 mm in the thin plate specimen. Regarding crack morphology parameters, the local roughness was assumed to be 7.4 μm, which is the same

as the given global value. Local and global path deviations were both assumed to be 1. The calculated values are shown in Table 4.18.

Table 4.18. Result of the SGT analysis by KINS

Pressure	[MPa]	7.59	2.09	8.08	5.55	6.54	7.45
Temperature	[°C]	16.7	128.6	128.9	263.1	262.9	262.8
Measured leak rate	[g/s]	6.43	3.00	6.31	3.70	4.12	4.57
Computed leak rate	[g/s]	1.9	5.3	5.3	7.6	7.6	7.6

In conclusion, the exercise set for Phase II was treatable with the LEAPOR software except in the case of low pressure and temperature (see Table 4.15). Overall, the calculation of the dCOD shows a good agreement with the measured dCOD in the LBB sensitivity case. It is worth noting that the applicability of leak rate calculation software for short flow length is limited.

4.2.4. KIWA

KIWA's analyses of the benchmark problems are done with the ExcelSQUIRT code (see Section 2.5.2). ExcelSQUIRT has a simplified user interface as compared to previous versions (SQUIRT or WinSQUIRT). ExcelSQUIRT also lacks an opportunity to obtain intermediate results that are part of an analysis (leak rate is the only result from an analysis).

The artificial slit blind case has detailed information about the size of the crack and COD/COA values. However, some information regarding the crack morphology is missing. The global roughness is 22 mm. The unknown value for the local roughness does not have a large impact on the results. KIWA's results are given in Table 4.19, and the results from a sensitivity analysis are given in Figure 4.1.

Table 4.19. KIWA results of the artificial slit blind case

Data number		8	15	18	38	40	55
Pressure	[bar]	60.4	10.5	45	45.4	63.6	25.5
Temperature	[°C]	19.9	122.1	122.3	234.6	213	206.1
Computed leak rate	[kg/s]	---	0.0588	0.1173	0.0785	0.1358	0.0522

As shown in Table 4.19, no result was obtained for case 8 using ExcelSQUIRT. In order to get a valid result, it would have been necessary to assume a higher temperature for this case (> 52°C).

Figure 4.1. KIWA results of the artificial slit blind case, with a sensitivity analysis using different local roughness (1-22 μm)
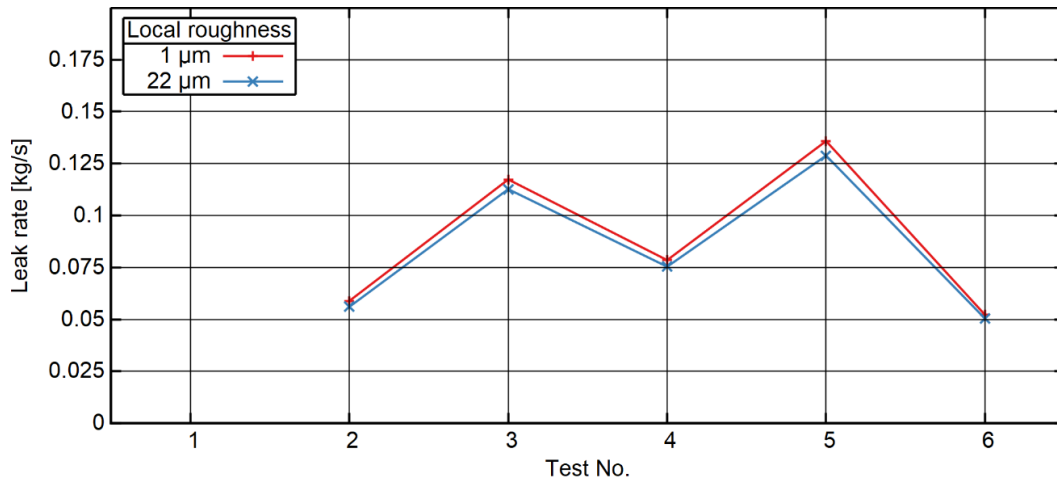

The fatigue crack blind case has detailed information about the size of the crack and that it is a fatigue crack (with "Global Roughness" = 40 μm given in the input data). KIWA performed a sensitivity analysis using different "Local Roughness" values and also compared its results with default data for CF (as given in ExcelSQUIRT). KIWA's results are given in Table 4.20, and the results from a sensitivity analysis is given in Figure 4.2.

Table 4.20. KIWA results of the fatigue crack blind case

Data number		31	18	32	13	44	49
Pressure	[bar]	75.3	65.5	15.7	45.4	50.6	30.1
Temperature	[°C]	199.4	234.8	200	238	16.7	151.9
Computed leak rate	[kg/s]	0.057	0.0472	0.008	0.0262	---	0.0373

Figure 4.2. KIWA results of the fatigue crack blind case, with a sensitivity analysis using different local roughness (1-40 μm) and predefined data within ExcelSQUIRT
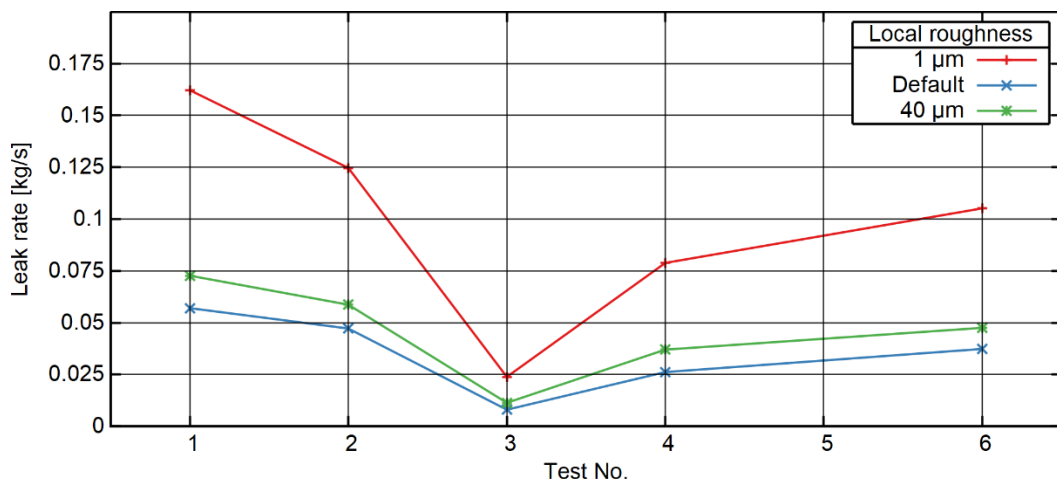
For the real event leak case**,** the actual position of the axial crack has a significant influence on the numerical result. However, this information is not given or known for this case. Furthermore, almost no information about the geometry and COD/COA of the crack is provided; the only value given is that the exterior crack length is less than 25 mm. Finally, the bending load is also unknown.

KIWA performed a number of sensitivity analyses of this case, based on what is stated in the input data (crack length less than 25 mm, wall thickness 12 mm and outer diameter 50-75 mm). Reasonable input data gave a very small leak rate (~0 kg/s); an attempt to get the upper bound value gave a leak rate in the interval 0.002-0.01 kg/s.

In the LBB sensitivity study, a sealed through-wall crack in a cylindrical pipe is subjected by a four-point bending at a constant pressure of 15.8 MPa. At the crack centre, the change in COD is measured as a function of the bending moment. The purpose of this study is to calculate the additional COD given by the bending moment and compare it with the measured values.

KIWA uses an in-house tool to calculate COD (inner, centre, outer position). The tool calculates an elastic and an elastic-plastic estimate of the COD. KIWA's results are presented in Figure 4.3 and Figure 4.4.

Figure 4.3. KIWA results of the LBB sensitivity study, using elastic COD estimates
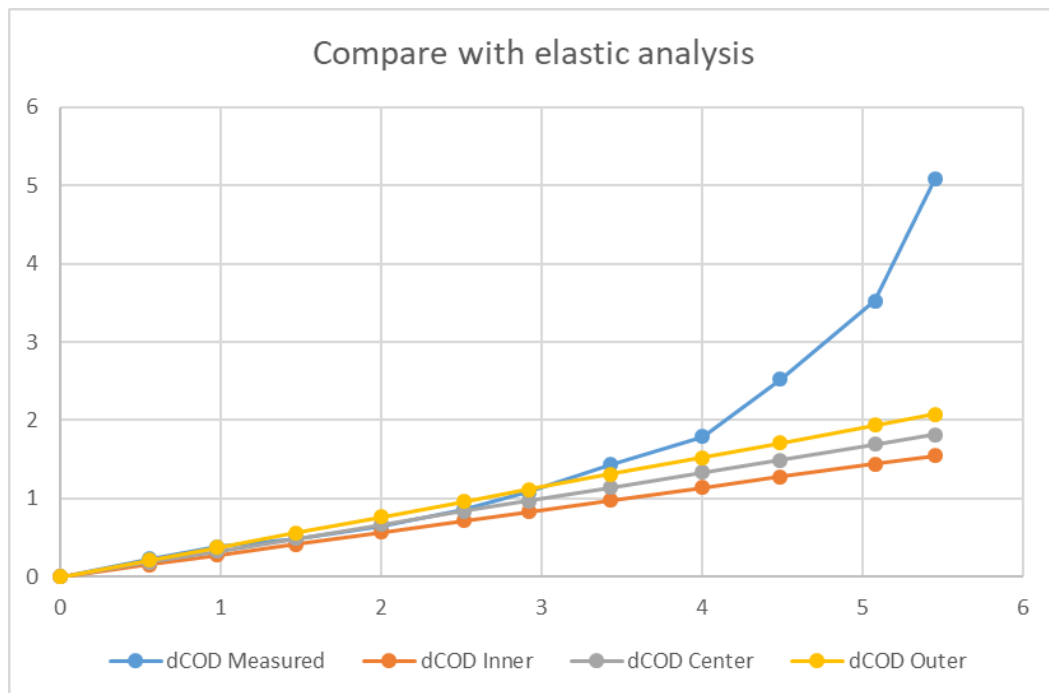
Figure 4.4. KIWA results of the LBB sensitivity study, using elastic-plastic COD estimates
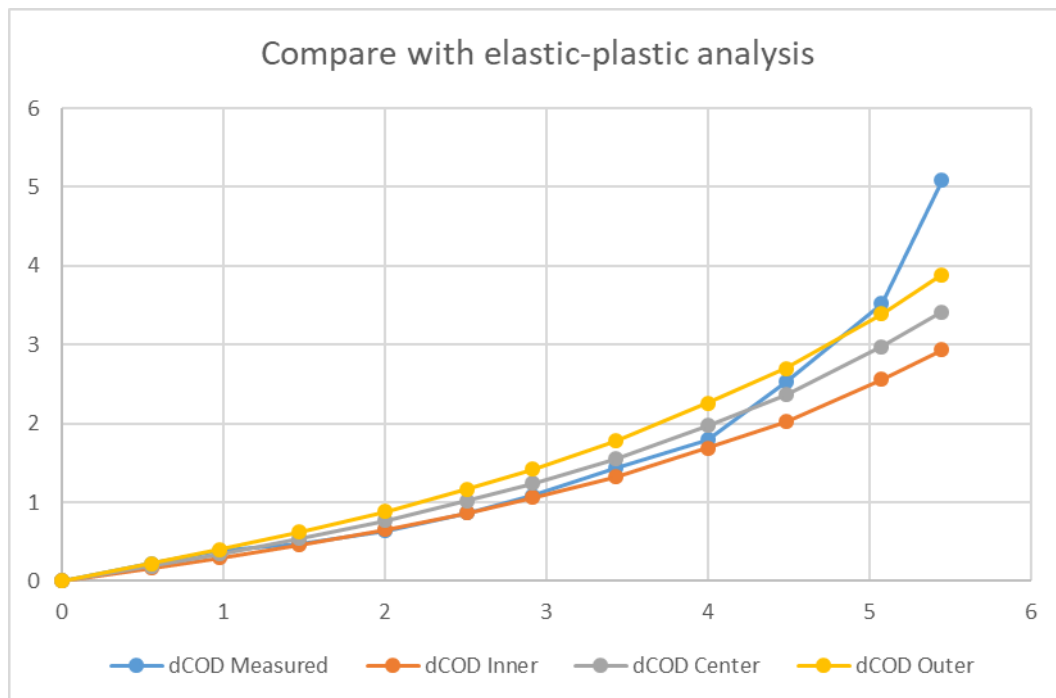
The steam generator tube leak specimen is a case with a very thin wall thickness (1.23 mm). This case differs from the others as it is a round hole to be analysed. KIWA's results using ExcelSQUIRT are presented in Table 4.21 and Figure 4.5.

Table 4.21. KIWA's results for the steam generator tube leak specimen

Data number		10	13	19	20	22	24
Pressure	[MPa]	7.59	2.09	8.08	5.55	6.54	7.45
Temperature	[°C]	16.7	128.6	128.9	263.1	262.9	262.8
Measured leak rate	[g/s]	6.43	3.00	6.31	3.70	4.12	4.57
Computed leak rate	[g/s]	3.67	1.83	3.67	2.83	3.00	3.33

Figure 4.5. KIWA's results for the steam generator tube leak specimen
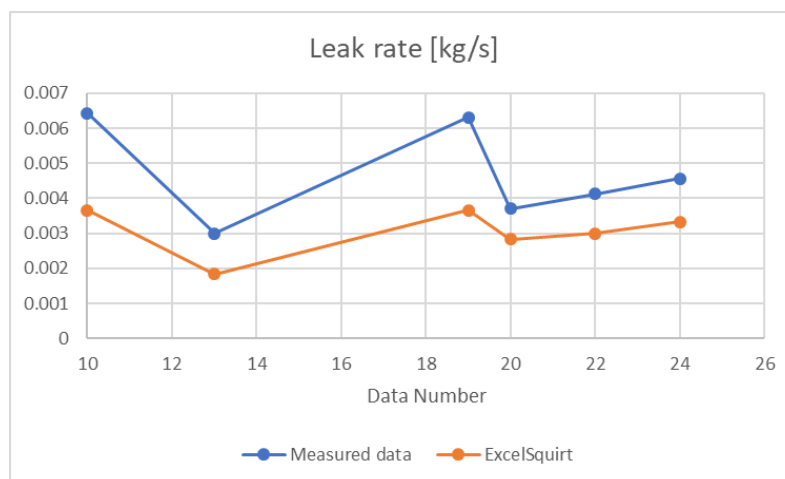
4.2.5. NRC

The leak rates for the blind artificial slit case (Table 4.22) were determined using LEAPOR (see Section 2.5.4) and its GUI input programme, LEAPOR-SA. The geometry and thermodynamic parameters for the Artificial Slit problem that were given in the problem description were used for the specified inside diameter and outside diameter. Crack lengths (2c) were used, and the COD values were the average of the three values specified in the problem description: 147.7 and 209.3 µm for the inside and outside, respectively. Further, a rectangular crack cross section was assumed. A second set of calculations was performed using COD values derived from the tabulated 2c and COA values: 150.2 and 210.0 µm for the inside and outside, respectively. The specified total resistance value, zeta, was not used in the calculations as LEAPOR internally performs its own calculation of the Darcy friction factor. Since the slit was artificial and no further information was given, a value of zero was assumed for the number of turns per unit length parameter. The leak path deviation parameters were assumed to be unity and an entry loss coefficient of 0.95 is hard-coded in LEAPOR. The calculation for single-phase leak, data number 8, could not be performed because LEAPOR is specifically designed for two-phase calculations. The calculation (2c, COA) for data number 18 did not converge so no result is given.

Table 4.22. NRC results for the blind artificial slit case

Data number		8	15	18	38	40	55
Pressure	[bar]	60.4	10.5	45	45.4	63.6	25.5
Temperature	[°C]	19.9	122.1	122.3	234.6	213	206.1
Leak rate (2c, COD)	[kg/s]	N/A	0.0507	0.1070	0.0637	0.1175	0.0406
Leak rate (2c, COA)	[kg/s]	N/A	0.0517	N/A	0.0649	0.1195	0.0414

For the fatigue crack case, COD-dependent crack morphology parameters for CF with local roughness of 8.8 µm, global roughness of 40.5 µm, 6 730 turns per metre, global path length of 1.017 and global plus local path length of 1.06 were chosen. As before, the COD was evaluated from the COA and 2c values, but since the calculated COD values did not differ significantly from the tabulated COD values, only calculations using the tabulated COD values were performed (Table 4.23). Data number 45 could not be evaluated because it involved a single-phase leak.

Table 4.23. NRC results for the blind calculation of fatigue crack

Test No		1	2	3	4	5	6
Data set		8	15	18	38	40	55
Pressure	[bar]	75.3	65.5	15.7	45.4	50.6	30.1
Temperature	[°C]	199.4	234.8	200	238	16.7	151.9
Leak rate	[kg/s]	0.0786	0.0696	0.0135	0.0499	N/A	0.0582

Input parameters for the blind calculation of the real event, i.e. wall thickness, internal pressure and temperature, and crack shape and axial orientation, were specified in the problem description. Other parameters, i.e. material properties, leak geometry, and crack morphology, were supplied by the participants for best- as well as under- and over-estimates (Table 4.24). The NRC chose the values to minimise the COD and leak rate as the under-estimate.

Material parameters were those of 304 stainless steel taken from the xLPR Inputs Group Report [36], and the COD was calculated using the xLPR axial crack COD module [37]. Crack morphology parameters were those of air fatigue of stainless steel [14]. Local and global roughness values were varied for the under- and over-estimation, but the number of turns per length of 2520/m and the global and local + global deviation factors of 1.07 and 1.33, respectively, were held constant for all three cases.

Table 4.24. NRC exercise sheet for the blind calculation of real event

		Under-estimation	Best-stimate	Over-estimation	Comment
Assumptions	Pipe diameter	D = 50	D = 62.5	D = 75	Straight pipe assumed
	Justification	Min D → min COD, min leak	Mean D → nominal	Max D → max COD, max leak	
Parameter estimates	Young's Modulus [MPa]	203 200	176 700	150 200	304SS from xLPR Inputs Report [35]
	Yield stress [MPa]	190	153	123	
	Ultimate stress [MPa]	507	442	438.6	
	Poisson number [-]	0.3	0.3	0.3	
	Ramberg-Osgood alpha [-]	2.137	2.314	2.439	
	Ramberg-Osgood n [-]	3.838	3.558	3.253	
	Bending [kNm]	0	0	0	Axial flaw: no bending effect
	Full crack length [mm]	15	18	22	Engineering judgement
	Local roughness [µm]	15	8	3	Air fatigue (SS) NUREG/CR-6004 Under- and over-estimation: Engineering judgement
	Global roughness [µm]	50	33.65	20	
Crack opening area results	Crack opening displacement [mm]	0.00272	0.00358	0.00521	Midwall
	Crack opening area [mm²]	0.0320	0.0506	0.0900	Midwall
	Hydraulic diameter [mm]	0.0042	0.0055	0.0080	

Table 4.24. NRC exercise sheet for the blind calculation of real event (Continued)

		Under-estimation	Best-stimate	Over-estimation	Comment
Effective morphology results	Effective roughness [μm]	15.0	8.02	3.28	
	Effective flow length [mm]	16.0	16.0	16.0	
	Effective number of turns	2 520	2 519	2 483	
Flow resistance results	Inlet resistance		CD = 0.95		
	Darcy Friction Factor	0.924	0.924	0.854	
	Frictional resistance				
	Total resistance				
Leak rate	Mass flow rate [kg/s]	2.76E-05	4.95E-05	1.04E-04	

For the LBB sensitivity analysis (Table 4.25), the COD for zero bending moment was computed for an axial force that resulted from the internal pressure. Two sets of inputs were chosen for the computation of the COD. The first set included the influence of 50% crack face pressure (CFP, 7.9 MPa) while the second set did not include CFP in the COD calculation. The dCOD values were calculated by subtracting the COD value at zero bending moment from the COD value at the applied bending moment (Table 4.25). All of the reported COD values are those at the mid-wall.

Table 4.25. NRC result of the LBB sensitivity analysis

	COD with 50% crack face pressure		COD without crack face pressure		Measured dCOD
Bending moment	Total COD	dCOD	Total COD	dCOD	
[MNm]	[mm]	[mm]	[mm]	[mm]	[mm]
0	0.495	0	0.382	0.000	0.00
0.55	0.718	0.224	0.606	0.224	0.23
0.98	0.895	0.400	0.782	0.400	0.38
1.47	1.099	0.604	0.985	0.603	0.48
2.00	1.327	0.832	1.211	0.829	0.64
2.51	1.561	1.066	1.442	1.060	0.86
2.92	1.765	1.271	1.643	1.261	1.08
3.43	2.052	1.557	1.921	1.539	1.44
4.00	2.436	1.941	2.292	1.910	1.79
4.49	2.846	2.351	2.686	2.304	2.53
5.08	3.482	2.987	3.294	2.912	3.52
5.45	3.989	3.494	3.777	3.395	5.08

For both sets of input, the calculated dCOD was smaller than the measured values. For lower bending moments, M ≤ 1 MNm, where the strains were probably elastic, the dCOD for the calculations with and without CFP were identical and closely mirrored the measured COD values. However, for larger applied moments where plasticity was presumably

involved, the calculated dCOD lagged the measured dCOD values. The dCOD values when CFP was included became increasingly larger than those when CFP was not included, as might be expected when plastic deformation is occurring.

For the steam generator tube leak case, the wall thickness of 1.23 mm and the tube hole diameter of 0.3 mm resulted in a thickness to diameter ratio of 4.1, which placed it within the LEAPOR orifice flow regime (Regime 4). The computed values for all cases except for the single-phase leak case are shown in Table 4.26.

Table 4.26. NRC result of the SGT analysis

Pressure	[MPa]	7.59	2.09	8.08	5.55	6.54	7.45
Temperature	[°C]	16.7	128.6	128.9	263.1	262.9	262.8
Measured leak rate	[g/s]	6.43	3.00	6.31	3.70	4.12	4.57
Computed leak rate	[g/s]	N/A	2.05	4.04	3.05	3.31	3.54

As was the case for the artificial slit, LEAPOR significantly underestimated the real leak rate. The reason for this underestimate is not clear as the LEAPOR Regime 4 for orifice flow was specifically developed for such a problem.

4.2.6. OCI

Blind artificial slit case – LOCI™ solutions using the extended Henry-Fauske model for the blind artificial slit case are presented in Table 4.27.

Table 4.27. OCI results for blind artificial slit case

Data number		8	15	18	38	40	55
Pressure	[bar]	60.4	10.5	45.0	45.4	63.6	25.5
Temperature	[°C]	19.9	122.1	122.3	234.6	213.0	206.1
Henry-Fauske	[kg/s]	0.179	0.051	0.107	0.064	0.118	0.041

Blind fatigue crack case – LOCI™ solutions using the extended Henry-Fauske model for the blind Fatigue Crack Case are presented in Table 4.28. The morphology parameters were obtained from the LOCI™ morphology database for the fatigue damage mechanism as given in Table 3.26.

Table 4.28. OCI Results for blind fatigue crack case

Data number		31	18	32	13	44	49
Pressure	[bar]	75.3	65.5	15.7	45.4	50.6	30.1
Temperature	[°C]	199.4	234.8	199.4	238.0	16.7	151.9
Henry-Fauske*	[g/s]	54.3	45.0	8.0	28.4	51.6	36.0

*Morphology parameters taken from Table 3.26 LOCI™ database for fatigue.

Blind real event case – LOCI™ solutions for the blind real event case are presented in Table 4.29. The morphology parameters were obtained from the LOCI™ morphology database for the fatigue damage mechanism as given in Table 3.26. The COA for a rectangle is calculated by the GE/EPRI EPFM model with crack face pressure included. The under-estimate solution was obtained with the modified Bernoulli model; the best-

estimate solution applied the Henry-Fauske model, and the over-estimate solution applied the Bernoulli model.

Table 4.29. OCI Results for blind real event case

Leak rate [g/s]		
Under-estimate	Best-estimate	Over-estimate
0.158	0.243	0.545

Blind LBB sensitivity case – LOCI™ solutions for the blind LBB Sensitivity Case are presented in Table 4.30. The COD for a rectangle is calculated by the GE/EPRI EPFM model with crack face pressure included.

Table 4.30. OCI Results for blind LBB sensitivity case

	Best-estimate (EPRI/GE EPFM)		
Bending moment	Total COD	dCOD	Measured dCOD
[MNm]	[mm]	[mm]	[mm]
0	0.34	0.00	0.00
0.55	0.49	0.15	0.23
0.98	0.61	0.27	0.38
1.47	0.74	0.40	0.48
2.00	0.89	0.55	0.64
2.51	1.03	0.69	0.86
2.92	1.14	0.80	1.08
3.43	1.28	0.94	1.44
4.00	1.44	1.10	1.79
4.49	1.58	1.24	2.53
5.08	1.74	1.41	3.52
5.45	1.85	1.51	5.08

Blind SGT case – Applying the modified Bernoulli model, the LOCI™ solutions for the blind SGT case are presented in Table 4.31.

Table 4.31. OCI results for blind SGT case

Pressure	[MPa]	7.59	2.09	8.08	5.55	6.54	7.45
Temperature	[°C]	16.7	128.6	128.9	263.1	262.9	262.8
Measured leak rate	[g/s]	6.43	3.00	6.31	3.70	4.12	4.57
Computed leak rate	[g/s]	5.58	2.65	5.48	1.41	2.28	2.85

4.2.7. PSI

PSI applied the LEAPOR and the WinLeck code. The analysis results for the blind artificial slit case are shown in Table 4.32.

Table 4.32. PSI results of the blind artificial slit case

Pressure	[MPa]	6.04	1.05	4.5	4.54	6.36	2.55
Temperature	[°C]	19.9	122.1	122.3	234.6	213	206.1
Leak rate	[kg/s]	0.04463	0.01941	0.03933	0.02917	0.04388	0.02064

Table 4.32 shows that the leak rate calculated with LEAPOR increases with higher pressure and temperature. At pressures above 6 MPa, its influence on the leak rate increases. The leak rate is 0.45 kg/s and 0.44 kg/s when the temperature is 19.9°C and 213°C, respectively. For the eroded slit, it is likely that the leak rate is influenced more by the primary loadings, e.g. internal pressure and bending moment, than by the thermal stress caused by temperature difference.

Table 4.33. PSI results of the blind fatigue crack

Pressure	[MPa]	7.53	6.55	1.57	4.54	5.06	3.01
Temperature	[°C]	199.4	234.8	200	238	16.7	151.9
Leak rate	[kg/s]	0.13529	0.10428	0.01946	0.07126	0.0447	0.08925

For the blind fatigue case, the highest leak rate is obtained at the highest pressure and temperature. It is found that at higher temperature, the leak rate is increased. Around a certain temperature (i.e. 200°C), the leak rate drops by six times when the pressure is reduced from 7.53 MPa to 1.57 MPa. However, when the pressure is around a certain value (i.e. 4.54 MPa and 5.06 MPa), the leak rate drops by 1.6 times when the temperature is reduced from 238°C to 16.7°C. The leak rate drops from 0.13 to 0.1 (by 23%) when the internal pressure is reduced by 1 MPa, despite a temperature increase of 34°C. It is likely that the leak rate is more influenced by internal pressure rather than by the temperature.

The results for the blind real event case are shown in Table 4.34; a crack length of 50 mm was assumed to produce these results.

Table 4.34. PSI result of the real event analysis

		Underestimation	Best-estimate	Overestimation
Leak rate	[kg/s]	0.0144	0.0173	0.019

The moment of inertia I and the polar moment of inertia W are given in the following formulas,

$$I = \frac{\pi\left(D_o^4 - D_i^4\right)}{64} \tag{65}$$

$$W = \frac{\pi\left(D_o^4 - D_i^4\right)}{32D_o} \tag{66}$$

where D_o and D_i are the outer diameter and the inner diameter of the pipe, respectively. Given a certain thickness, both I and W increases with larger D_o. The maximum bending moment is given as below:

$$M_b^{max} = \frac{\sigma \cdot I}{D_o/2} = \sigma \cdot W \tag{67}$$

Therefore, M_b^{max} is proportional to the polar moment of inertia W. It can be concluded from this case that with a certain wall thickness, a larger outer diameter increases the bending moment linear, causing a higher mass flow rate.

Table 4.35. PSI results of the LBB sensitivity analysis

Bending moment	Total COD	COA	dCOD	Measured dCOD
[MNm]	[mm]	[mm²]	[mm]	[mm]
0	0.002	0.65469	0	0.00
0.55	0.180107279	58.95721712	0.178107279	0.23
0.98	0.318699101	104.3245571	0.316699101	0.38
1.47	0.478282791	156.5634802	0.476282791	0.48
2.00	0.651598229	213.2974221	0.649598229	0.64
2.51	0.817816256	267.7080624	0.815816256	0.86
2.92	0.949308716	310.7514615	0.947308716	1.08
3.43	1.11521434	365.0598381	1.11321434	1.44
4.00	1.301953353	426.1879203	1.299953353	1.79
4.49	1.459980559	477.9173361	1.457980559	2.53
5.08	1.652111781	540.810531	1.650111781	3.52
5.45	1.773389307	580.5101226	1.771389307	5.08

Figure 4.6. PSI result for bending moment and COD
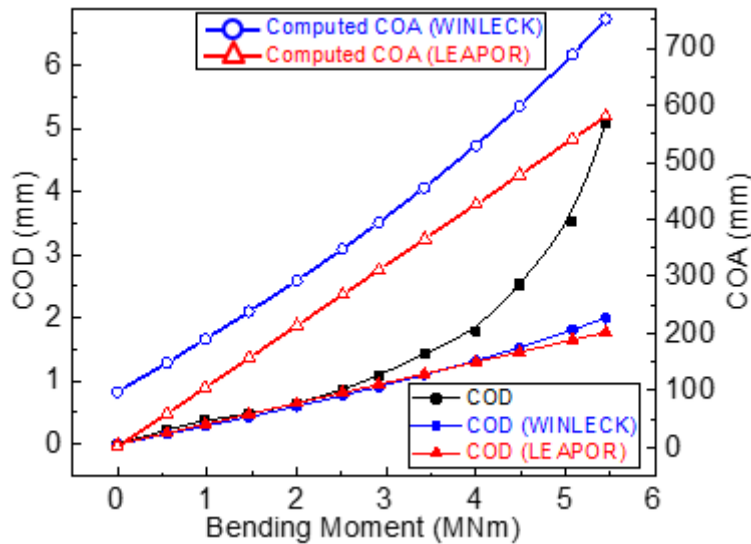
As LEAPOR code cannot deal with the variable bending moment, the COD calculation method implemented into this code (Zahoor, see Section 2.2.1) can be referred to. Meanwhile, WinLeck software was also applied in this case. The calculated results from these two different tools are in good agreement, but the computation results do not agree with experimental findings if the bending moment is over 2.5 MNm. One possible reason

for the difference in COD is that the implemented models in LEAPOR and WINLECK can only assume the conservative CODs at lower bending moment.

Table 4.36. PSI results of the SGT analysis

Pressure	[MPa]	7.59	2.09	8.08	5.55	6.54	7.45
Temperature	[°C]	16.7	128.6	128.9	263.1	262.9	262.8
Measured leak rate	[kg/s]	0.00643	0.00300	0.00631	0.00370	0.00412	0.00457
Computed leak rate	[kg/s]	0.00517	0.00263	0.00517	0.0039	0.00424	0.00453

Because LEAPOR-SA can only be used for cylindrical pipes, here it is assumed that the outer diameter of this pipe is very large (10^6 mm) and can be regarded as a plate. It is assumed that the crack length is 0.6 mm and the COD is 0.3 mm. The final results are in good agreement with the measured results. There is only one exception: The calculated leak rate with lower temperature is lower than the measured leak rate. It is likely that there is a temperature limit in the LEAPOR code, as mentioned in Section 3.2.8.

4.2.8. SNC

Leak rates for the exercise set in Phase II of the benchmark are estimated using LEAPOR, and for single-phase flow problems with low temperature, a single-phase flow equation is used.

For the blind artificial slit problem, a pipe with a large diameter (D=2000 mm) is considered instead of a rectangular shaped plate. Based on the crack length and COA, the COD is calculated at ID and OD. As the information of local roughness was not provided, it is assumed to be the same as the global roughness (22 µm). The results of the blind artificial slit problem are provided in Table 4.37.

Table 4.37. SNC results of the blind artificial slit case

Pressure	[MPa]	60.4	10.5	45	45.4	63.6	25.5
Temperature	[°C]	19.9	122.1	122.3	234.6	213	206.1
Leak rate	[kg/s]	0.127	0.052	0.109	0.065	0.12	0.041

For the test cases with temperatures of 19.9°C and 122.3°C, LEAPOR was unable to converge to a solution, hence a single-phase flow equation was used.

Similarly, for the blind fatigue crack problem, a pipe with large diameter (D=2000 mm) is considered instead of a plate, and a local roughness of 40 µm is used, which is the same as the global roughness. The results of the blind fatigue crack problem are provided in Table 4.38.

Table 4.38. SNC results of the blind fatigue crack

Pressure	[MPa]	75.3	65.5	15.7	45.4	50.6	151.9
Temperature	[°C]	199.4	234.8	200	238	16.7	151.9
Leak rate	[kg/s]	0.073	0.059	0.012	0.043	0.106	0.049

The leak rates for all test cases were estimated using LEAPOR, except for the case with a temperature of 16.7°C, for which a single-phase flow equation was used.

For the real event analysis, a full crack length of 25 mm is considered for all the cases. For underestimation and best-estimation case, the crack is assumed to be smaller than the OD

of the reducer. For overestimation case, the crack is considered larger than the OD, as the influence of hoop stress on the axial crack would be higher.

The COD is computed using the formulation used in xLPR. The effect of the bending moment on the axial crack COD is not considered. The material property in the underestimation case is based on reference material property provided in the test problem. Experimental data is used for estimating the material properties for best-estimate and overestimation cases. For all the three cases, crack morphology due to CF (Table 3.9 of Reference [14]) is considered.

Table 4.39. SNC result of the real event analysis

		Underestimation	Best-estimate	Overestimation
Leak rate	[kg/s]	1.07E-04	1.16E-04	2.39E-04

The COD in the LBB sensitivity analysis is computed using the solution available in API 579-1/ASME FFS-1, June 2016, which is based on the WRC method (see Section 2.2.6), with plastic correction factor applied. The correction factor is purely based on reference stress solution with yield strength.

Table 4.40. SNC result of the LBB sensitivity analysis

Bending moment	Total COD	COA	dCOD	Measured dCOD
[MNm]	[mm]	[mm]	[mm]	[mm]
0	0.444	145.247	0.000	0.00
0.55	0.605	197.916	0.161	0.23
0.98	0.726	237.743	0.283	0.38
1.47	0.868	284.175	0.424	0.48
2.00	1.033	338.216	0.589	0.64
2.51	1.218	398.863	0.775	0.86
2.92	1.399	457.879	0.955	1.08
3.43	1.692	554.041	1.249	1.44
4.00	2.151	704.355	1.708	1.79
4.49	2.687	879.592	2.243	2.53
5.08	3.582	1 172.710	3.138	3.52
5.45	4.324	1 415.600	3.880	5.08

The computed COD reasonably agrees well with the measured one, expect for a few cases. In general, the calculated COD is lower than the measured one for the load levels.

For steam generator tube leak assessment, LEAPOR is used without any modification to the programme. A pipe with a large diameter and an elliptical crack is considered. The CODs at ID and OD are calculated from the crack diameter and COA provided. Additionally, local roughness is assumed to be the same as global roughness.

Table 4.41. SNC result of the SGT analysis

Pressure	[MPa]	7.59	2.09	8.08	5.55	6.54	7.45
Temperature	[°C]	16.7	128.6	128.9	263.1	262.9	262.8
Measured leak rate	[kg/s]	0.00643	0.00300	0.00631	0.00370	0.00412	0.00457
Computed leak rate	[kg/s]	0.0040	0.0021	0.0040	0.0031	0.0033	0.0035

LEAPOR under-predicts the leak rate for all the cases considered and the percentage difference varies from 21.25% to 58.9%.

4.3. Comparison

In this section, the individual submissions are compared, and the agreement among the participants as well as the accuracy relative to the reference values is discussed.

4.3.1. Blind artificial slit case

Seven organisations submitted a total of eight contributions with analyses of the artificial slit case. Due to a unit mistake in the evaluation sheet, two evaluations were asked to be repeated as they deviated by several orders of magnitude, but they were also received without information about the actual measured leak rate values. All evaluations are based on the COD values of the slit and the roughness value; one participant used the flow resistance value. The graph with the individual mass flow rates and the reference (the measured mass flow in the experiment) is shown in Figure 4.7.

Figure 4.7. Result comparison for the blind artificial slit case
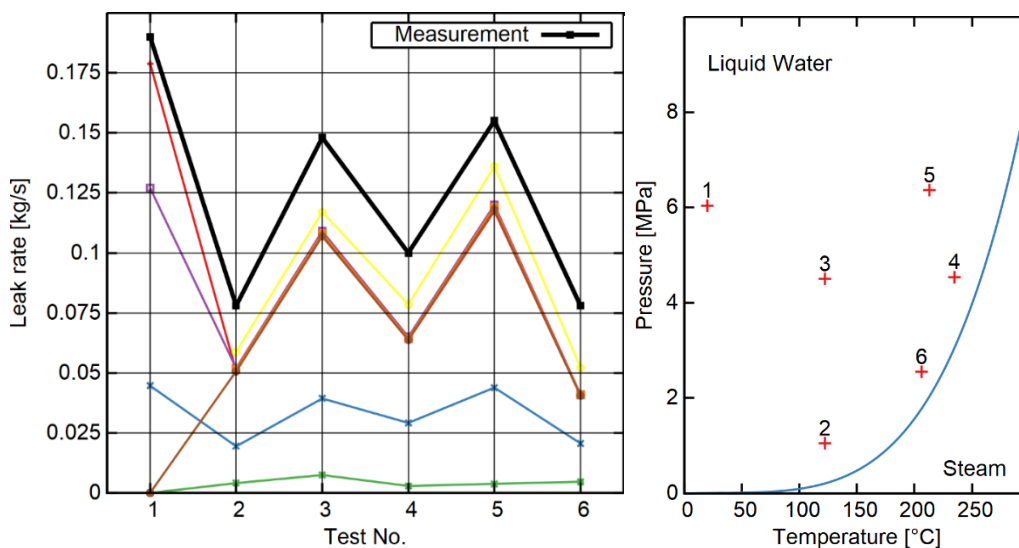
The contributed values are mostly very close to each other. All computed values underestimate the real leak rate for most cases. The accuracy is in most cases between about 20% and 30%, which is in agreement with the non-blind artificial slit cases and evaluation based on roughness instead of measured resistance. Two contributions (two variants produced by a single participant) are significantly lower than the rest. For the analysis of the influence of different approaches, the flow contributions are ordered according to the used flow model in Figure 4.8.

Figure 4.8. Comparison of flow model influence in the artificial slit case (blind contributions)
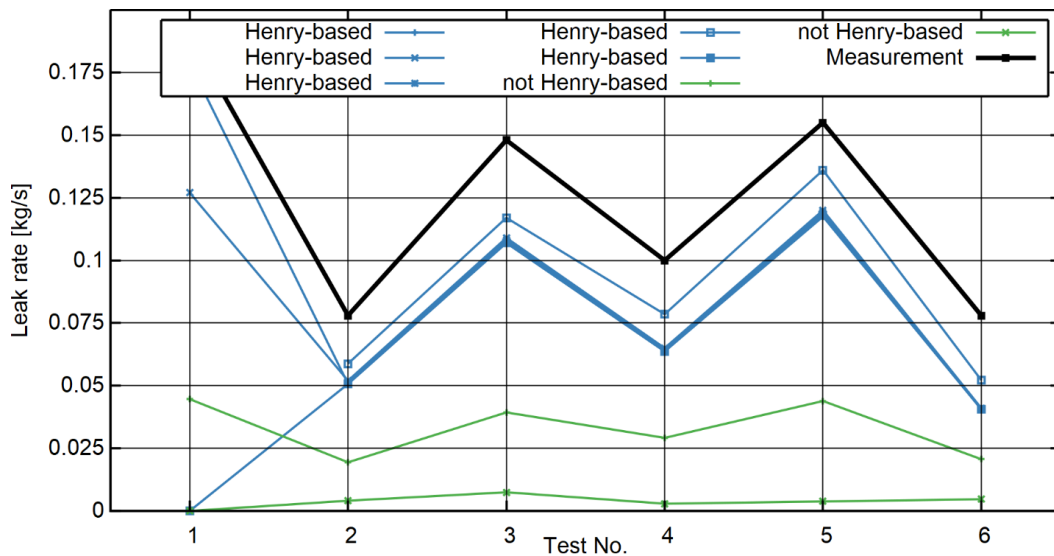
This evaluation shows that participants with the same model have very similar results, even in a blind analysis. There were also four non-blind contributions of two participants, which are evaluated separately in Figure 4.9.

**Figure 4.9. Comparison of non-blind contributions for the artificial slit case**
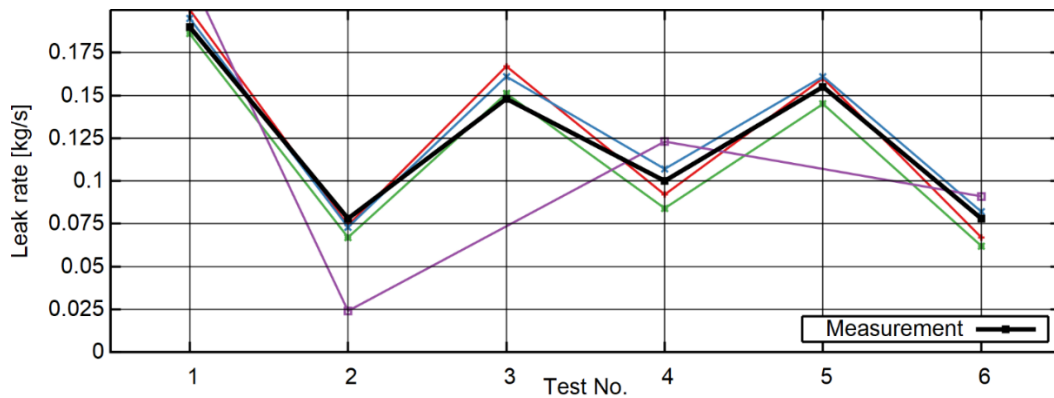
In this comparison, it is visible that the contributions are in good agreement with the reference result. The agreement of three of the contributions is apparently better than that of the blind contributions, which justifies the separate analysis.

4.3.2. Blind fatigue crack case

For the blind fatigue crack case, eight contributions from six participants were received. Due to a unit conversion mistake in the case definition, three contributions originally deviated by several orders of magnitude from the rest; these analyses were done again without knowledge of the actual leak rates in the tests. Most evaluations are based on the COD values, and all but one participant based their evaluations on the reported roughness values instead of the total resistance measured in the test. The comparison of the results is shown in Figure 4.10.

Figure 4.10. Result comparison of the blind fatigue crack case
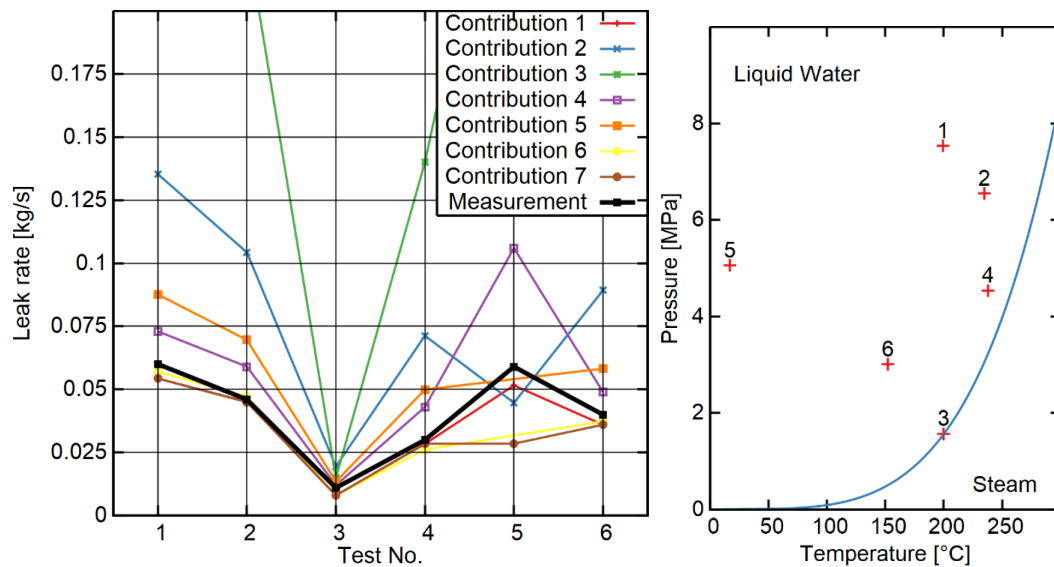
The agreement of most participants with the measured leak rate in the actual test is satisfying. Most participants have a good agreement between each other and with respect to the measurement in test 3, which is close to the saturation line. Another qualitative difference is observed for test 5, which is in the cold water regime. This overall result is comparable with the observations in the non-blind fatigue crack test. Contributions 2, 3 and 5 show a systematic overestimation – while 2 and 3 originate from the same contributor, 2 and 5 are both produced with LEAPOR.

To analyse the differences between the contributions, the friction characterisation is considered first, as some participants report the friction factor λ. The indication of the friction influence in each contribution is shown in Figure 4.11. It can be verified that the three contributions with a friction factor of 0.14 are very accurate and very close to each other (there is an exception for the cold test No 5). However, the other contributions are not directly scaling with the friction factor, which could be explained by different effective flow paths and additional pressure loss effects considered by the participants.

Figure 4.11. Characterisation of friction and pressure loss in the blind fatigue crack case
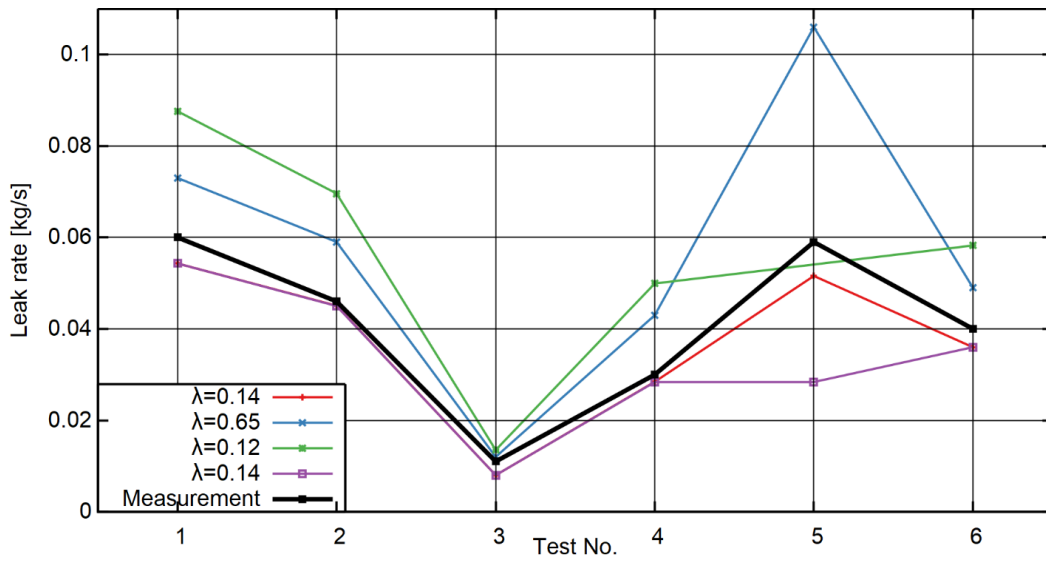

Concerning the flow model, all contributions but one use a Henry-based approach, while contribution 3 applies a modified Bernoulli model. The latter has the tendency to underpredict leak rates close to saturation conditions, so one could argue that the good match for test 3 compensates a general overestimation by chance. This can be verified in Figure 4.12.

Figure 4.12. The blind fatigue crack case by applied flow model
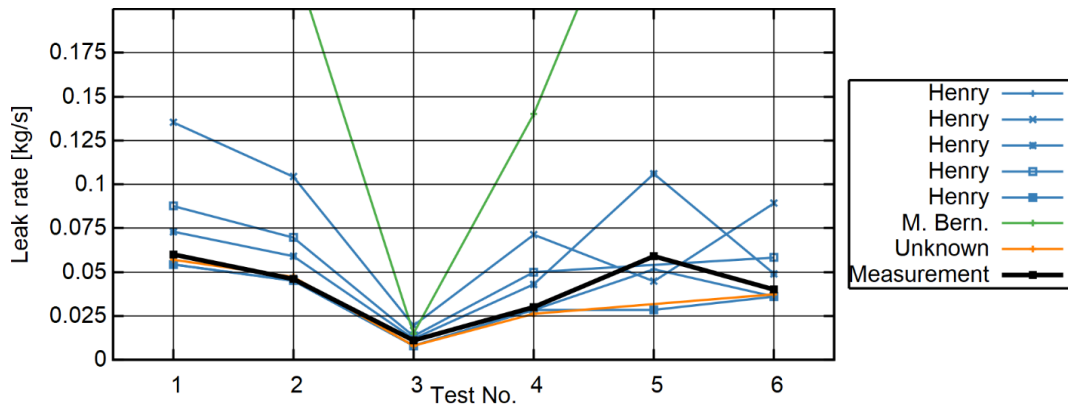
As with the artificial slit case, non-blind contributions were received to this case as well. They are compared in Figure 4.13. Analyses 1 and 5 show a better agreement than analyses 2, 3 and 4; in general, the non-blind contributions have a similar accuracy as the blind contributions.

Figure 4.13. Comparison of non-blind analyses of the fatigue crack
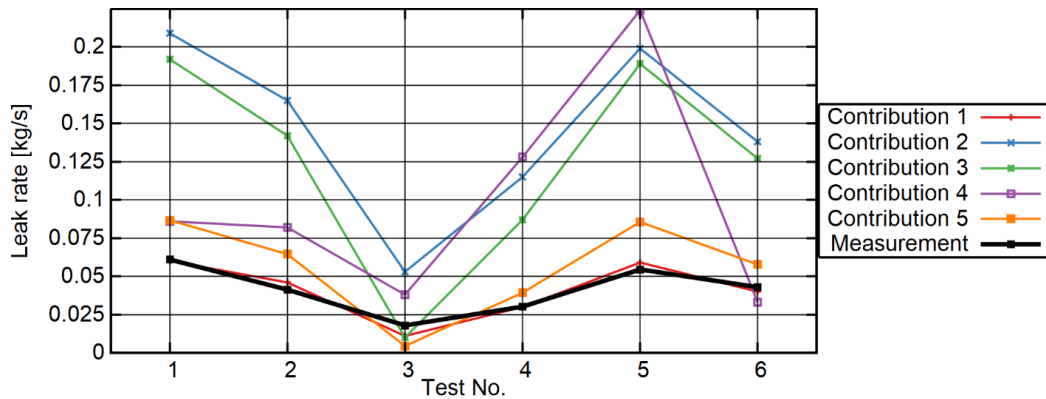
In summary, it can be concluded that some participants from the blind comparison were able to accurately and consistently predict the leakage rate of the specimen. Most have a moderate accuracy, and two outliers show a good result close to saturation conditions and minor quality for the rest of the tests.

4.3.3. Blind real event case

Seven analysis contributions were received from six organisations for the blind real event case, but two contributions were based on significantly different geometry assumptions and produced very different results; these two contributions were therefore removed from the comparison. All but one of the remaining contributions gave underestimating, best-estimate and overestimating predictions for the leak rate. The trend was obtained by choosing different ODs (from 50 mm to 75 mm), motivated by the fact that the crack is located at a reducer. Another uncertainty was the actual crack length, which is only known to be smaller than 25 mm (full crack length), and which was also used for estimating the possible range of leak rates. Both choices have a significant impact on the crack opening, as shown clearly in Figure 4.14 (one contribution did not indicate the COD values and is not included in this evaluation).

Figure 4.14. COD as a function of the full crack length in the blind real event case; the different choices of the effective pipe radius (not indicated) are a reason for vertical scattering
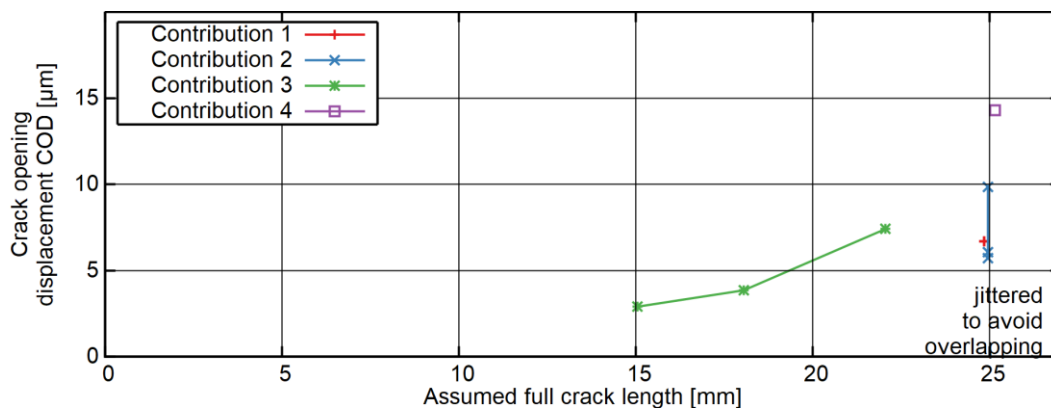
In this figure, the deviations in COD for the same 2c are mostly due to different choices of effective pipe diameter: Larger CODs correspond to larger radii since the pressure-induced hoop stress acting on the axial crack is larger. By virtue of their geometry alone, these

different leak areas already have a strong effect on the mass flow rate; other influences originate from friction and flow model. The comparison is shown in Figure 4.15 (the over-estimate contribution 4 did not indicate its COA value, and its reported value is hence shown as a horizontal line in the comparison).

Figure 4.15. Leak rate as a function of the leak opening area
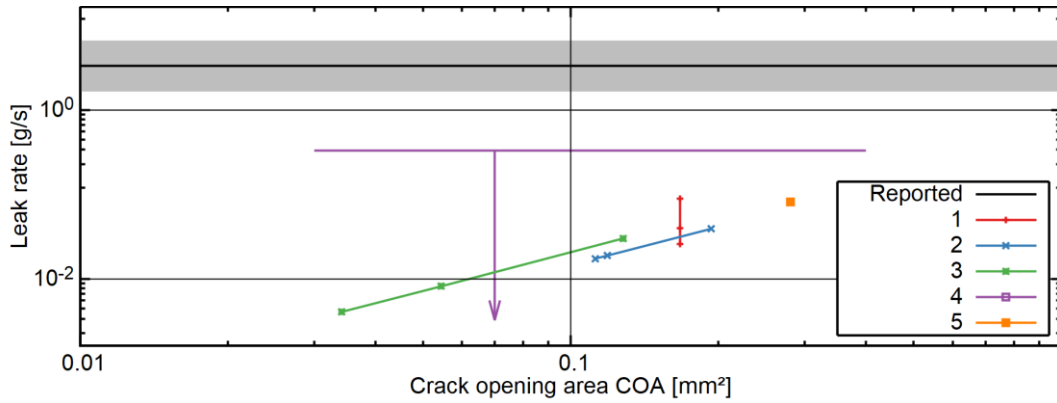
The figure shows clearly that the COA is the main influence on the computed leak rate, and friction/morphology effects and model differences between participants seem to be of minor importance. With regard to the reported leak rate, all teams compute much smaller mass flow values. The overall comparison of all contributions, ordered by underestimation, best-estimate and overestimation, is shown in Figure 4.16.

Figure 4.16. Result comparison of the blind real event case
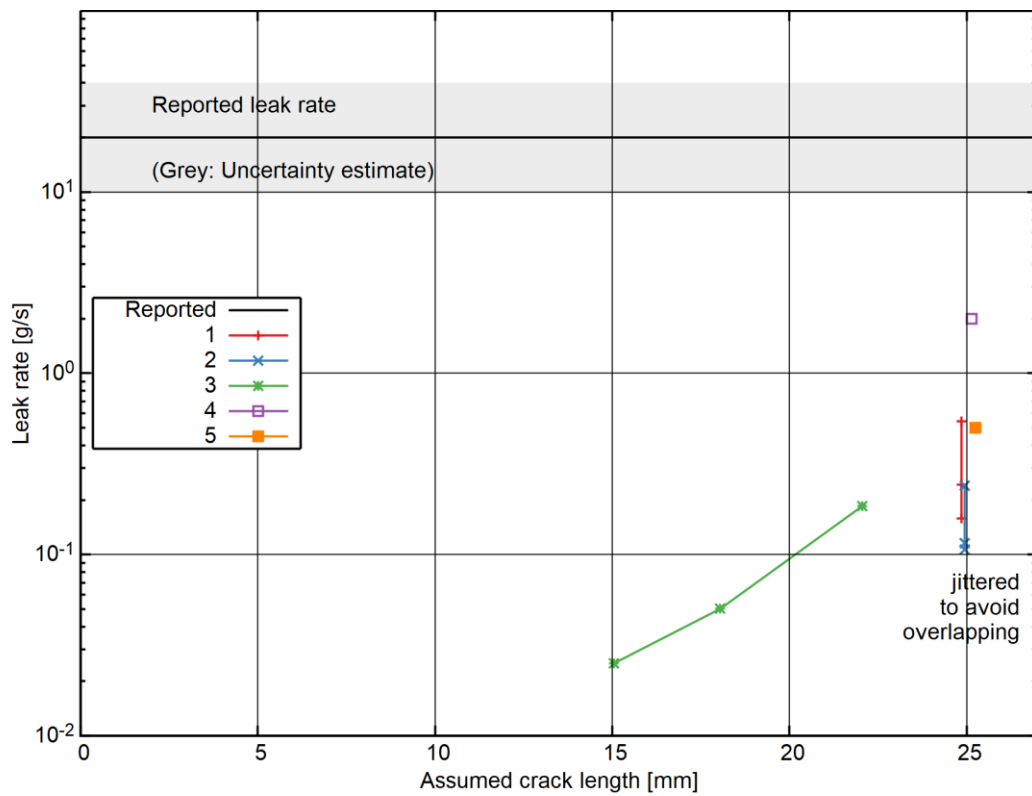
From this figure, it is visible that most contributors underestimate the reported leak rate significantly.

Three non-blind contributions were also received for this analysis. They assume a crack length of 25-27.4 mm and also underestimate the reported leak rate (Figure 4.17).

**Figure 4.17. Results comparison of non-blind analyses of the real event case**
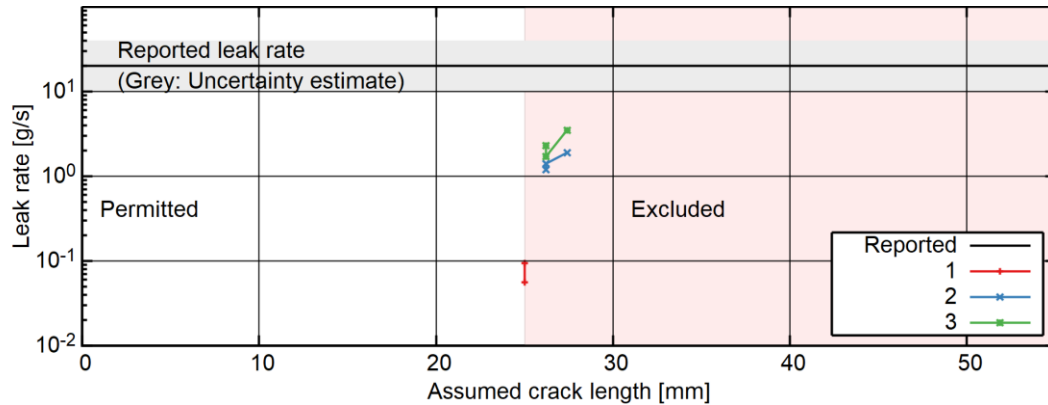
This finding raises the question about the reason for the systematic underestimation for all computation with consistent crack geometry. In principle, two mechanisms are observed that cause an excess of the leak rate from the fracture mechanical idealisation: Material loss due to (possibly flow accelerated) corrosion causes a larger leak opening than the pure mechanical displacement of the crack faces, and plastic deformations due to overloading which cause a permanent plastic opening in addition to the load-induced contribution. (Since clogging of narrow cracks is a well-known mechanism for the contrary effect.) This seems to be more likely than an error in the event report (for instance, the leak rate of 20 g/s is an estimated and not a measured value).

### 4.3.4. LBB sensitivity case

For the computation of the differential leak opening (dCOD) as a function of the applied bending moment in a full-scale test for the LBB sensitivity case, seven organisations provided nine contributions in total. One contribution is overestimating (1), two are underestimating (3 and 8) and the rest is best-estimate. The results are compared in Figure 4.18.

Figure 4.18. Result comparison for the LBB sensitivity case
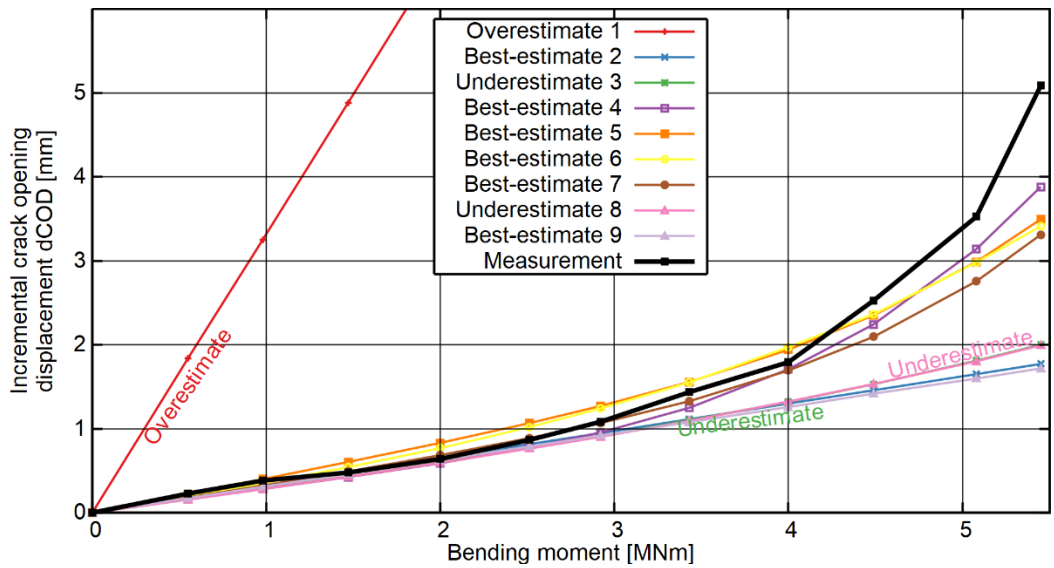
In the result, all contributions (except the intentionally overestimating contribution 1) find the correct elastic behaviour at small bending moment; deviations appear as plastic effects are manifest in the measured differential COD. The overestimating trend of contribution 1 and the underestimating trend of contribution 8 are clearly verified. In the best-estimate approaches, contributions 4, 5, 6 and 7 have the best accuracy event for large bending moments. The analysis of the contributions by method is shown in Figure 4.19.

**Figure 4.19. LBB sensitivity case by COD model**
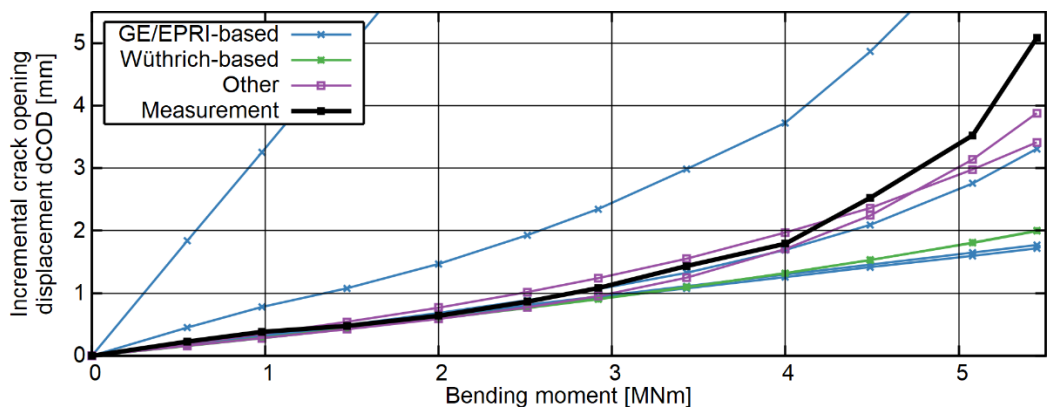
In this comparison, it is visible that the two Wüthrich-based approaches (which use the GRS-PB and the KTA 3206 approach) are very close. The GE/EPRI based contributions differ much (note that the intentionally overestimating contribution is an elastic approach). The two contributions classified as "Other" are most accurate.

4.3.5. Steam generator tube leak case

The steam generator tube leak case was analysed by seven participants with a total of nine contributions. The comparison of the leak rate computation with the actual measured leak rates is shown in Figure 4.20.

Figure 4.20. Result comparison for the steam generator tube leak case
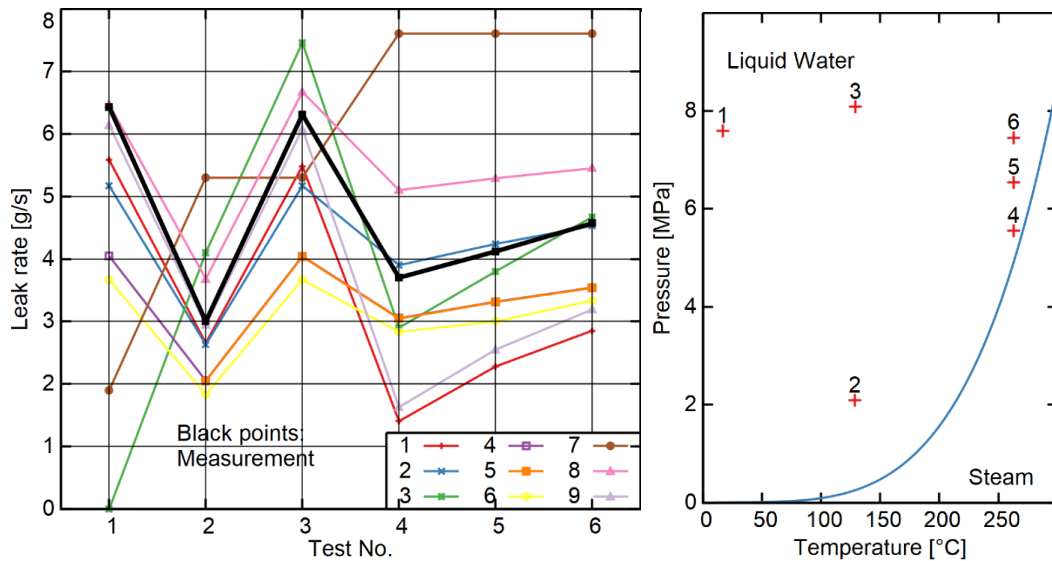
The measured leak rate is in most cases higher than the computed values of the participants. Contributions 2 and 8 show a good agreement with the measured leak rate in specific regimes. Contribution 3 does not include a value for the cold water case (test No. 1). Most others qualitatively follow the trend between the selected test points, except for contribution 7. A remarkable difference compared to e.g. the artificial slit case is the fact that the accuracy varies with the thermodynamic fluid conditions (test number), rather than them being a rough scaling factor. For an improved understanding of the different predictions, the applied flow models are indicated in Figure 4.21. Note that one LEAPOR-Henry contribution does not include a cold water test (test No. 1) and is almost identical to a Henry-based contribution for the other test numbers.

Figure 4.21. Steam generator tube leak case analysed by model
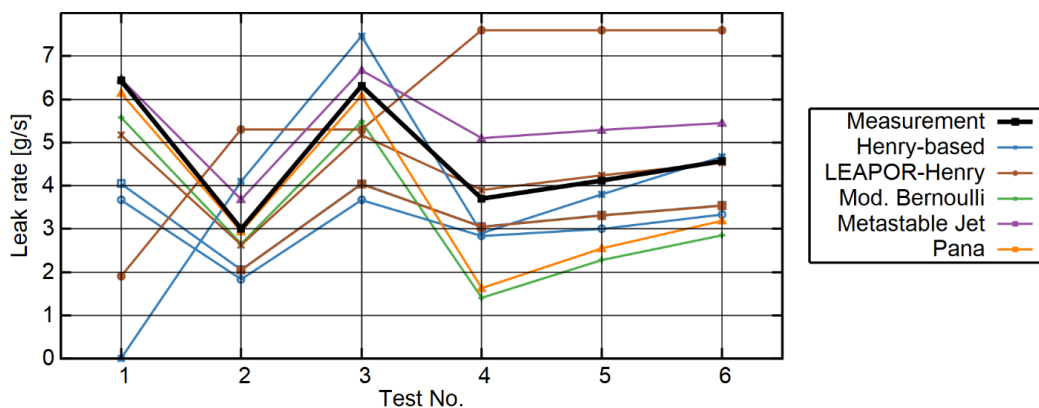
Most of the participants use Henry-based approaches (although the strict Henry model is not applicable since the ratio of wall thickness to hole diameter is too small), three of them by applying the LEAPOR code. The Pana model, the modified Bernoulli model and the metastable jet model are all used by one contribution each. Apparently, the Pana and modified Bernoulli contributions resemble each other, and they both underestimate the leak rate at high temperatures (test nos. 4-6). The metastable jet approach instead overestimates the high-temperature points. Two participants using the Henry approach and one using the LEAPOR analysis have very similar results, underestimating the measured leak rates

systematically with a slightly better performance for the tests closer to the saturation line (2, 4, 5, 6). One other LEAPOR analysis has a quite good agreement with the measurement (also with larger deviations for tests 1 and 3), while the others are different.

These findings indicate that the thermodynamic phenomena for steam generator leaks can be different from thick-walled piping leaks in specific regimes of fluid conditions. It can be expected that the vapour content in a short leak channel is smaller compared to long leaks, which increases the density and hence the mass flow rate. This could be an explanation for the systematic underestimating trend of most model predictions in this case and the rather good performance of uncommon models.

5. Conclusions and recommendations for further work

The two-phase activity on leak rate computation makes it possible to draw several conclusions on different levels. The following section summarises the conclusions from the benchmarking approach, the result analysis and the lessons learnt. It also provides recommendations for future activities.

The instructions for the benchmark exercises in tabular sheet form can be seen as a good approach to define the different test cases. However, additional details about the laboratory tests would be beneficial, as well as schematic drawings to make geometric settings clearer.

In general, the participants saw the benchmarking as an effective way to understand leak rate computation. The combination of open and blind sections was informative and can be seen as a distinct feature of this activity.

An important conclusion is that the participants applied different software (see Section 2.5), but these software tools often implement the same models and should consequently lead to similar results. In this way, this benchmarking was technically a code comparison, but the analysis of the contributions made it possible to identify the imprints of the model implementations. This reveals details about the individual tools used in the analysis and emphasises the (software) design background of each tool and what distinguishes them from one another. This survey gives an overview of the state of the art of approaches, methods and tools. The experience gained in this round robin activity can also help to improve the programmes in the future, while the experiment analysis and code comparison contribute to their validation.

The leakage model perspective (in contrast to the computation code perspective) played a key role in the analysis of the different contributions. Starting from fixed settings or assumptions of structure geometry, leak geometry and loads, the leak rate computation involves a model for leak opening (such as COD), for flow resistance and friction, and for the actual fluid motion. Each analysis approach, in principle, combines a model for leak opening, one for friction and one for fluid motion. In the analysis of contributions, this made it possible to track differences and agreements between different participants to model choices – even despite blind test case settings, as notably seen in Section 4.3.1.

Given this insight in the analysis of the contributions, it is possible to estimate the agreement between prediction and measurement with each model. As an alternative to the absolute accuracy, the suitability of approaches for underestimation or overestimation is also discussed. Thus, the round robin activity gives indications on the uncertainties in leak rate predictions and the approaches used by the participants. The limited selection of cases is not sufficient to quantify the uncertainties (e.g. for statements concerning probabilistic treatments). A preliminary conclusion is that the relevant influence factors on accuracy and the reliability of the leak rate prediction can be traced back to the performance of individual models and to detailed knowledge about the leak situation. Moreover, the present comparison gives an impression about the general range of variability to be expected in leak rate predictions.

From the perspective of individual computer codes, the margin between predicted and measured leak rates within the benchmark cases is interesting, as several codes were able to find that the difference is bounded by a factor of 2 (for the laboratory tests). Also, it is interesting that several analyses show conservative underestimating behaviour, which is also relevant from a regulatory perspective. The benchmarking showed also that there is

indeed a difference between blind and non-blind computations, though blind analyses also have a good accuracy.

Within the different test cases in the round robin, the analyses of real leak events stand out from the rest. These open analyses in the first benchmark phase and the blind analysis in the second benchmark phase have a surprising outcome. The first phase test case is based on a publication that demonstrates the capability of a leak rate software. The analysis result for this case shows that most participants are able to explain the reported leakage rate, but the uncertainties in the case definition due to unknown parameters allow for a larger range of possible leak rates. The second phase test case is based on event data and was selected according to the availability of data allowing an accurate model. The uncertainties in this case seem to be under control, but, remarkably, no model can explain the observed leakage rate. The actual leak rate is beyond the range that seems to be possible under the allowed conditions.

This behaviour of leakage rate is, of course, a singular observation, and it is too early to draw conclusions about this finding. However, the behaviour of real leaks from the operational experience is relevant for all leak rate assessments, and also for LBB procedures. While most analyses and model validations in leak rate analysis concentrated on laboratory specimens, it seems justified to think about validation of leak rate models also under consideration of real leaks from the operational experience. This would also be in accordance with the IAEA guide for deterministic safety analyses [35]. This finding could motivate follow-up activities in analysing leak events.

One of the test cases discussed within the benchmark was a steam generator tube-like specimen, which is different from ordinary LBB-related leak rate setups by a much smaller wall thickness and a smaller mass flow rate. This turned out to be an unusual case for leak assessment based on the traditional models, which provided new data for model comparison and showed a different behaviour than the other cases (namely a variation of the accuracy with the thermodynamic stagnation conditions).

Finally, the leak rate benchmark within the WGIAGE can also be seen as an update of former CSNI leak rate benchmark activities. A benchmark performed about 15 years ago [46] came to the conclusion that "the compilation of the results shows very large scatterbands in general, with deviations equally large between the calculations of the different participants and the calculation and the measurements." Progress has been achieved in gaining a deeper understanding of the phenomena, and improved analysis tools have been developed. Therefore, the current activity shows a rather good accuracy, at least for the (well-controlled) laboratory leak tests. Also, the comparative assessment approach is able to understand in detail the differences between approaches and to explain deviations.

References

[1] Heckmann, K., J. Sievers and F. Weyermann (2018), *Leak Rate Computation: Flow Resistance vs. Thermal-Hydraulic Aspect*, ASME Pressure Vessel and Piping Conference, 15-20 July 2018, Prague.

[2] Kumar, V., M.D. German and C.F. Shih (1981), *An Engineering Approach for Elastic-Plastic Fracture Analysis*, Electric Power Research Institute, Palo Alto.

[3] Kumar, V. et al. (1984), *Advances in Elastic-Plastic Fracture Analysis*, Electric Power Research Institute, Palo Alto.

[4] Heckmann, K., C. Bläsius and J. Sievers (2019), *WinLeck 5.0: User's Manual and Validation Report*. GRS-P-6, Vol. 1-2, Rev. 9, Handbuch, Cologne.

[5] Rahman, S. et al. (1998), "Crack-opening-area analyses for circumferential through-wall cracks in pipes - Part I: analytical models", *International Journal of Pressure Vessels and Piping*, 75 (5), pp. 357 - 373.

[6] Wüthrich, C. (1983), "Crack opening areas in pressure vessels and pipes", *Engineering Fracture Mechanics*, 18 (5), pp. 1049-1057.

[7] Gilles, P. and F.W. Brust (1991), "Approximate fracture methods for pipes - Part I: theory", *Nuclear Engineering and Design*, 127 (1), pp. 1-17.

[8] Tada, H., P.C. Paris and G.R. Irwin (2000), *The Stress Analysis of Cracks Handbook*, ASME Press.

[9] Anderson, T.L. (2003), "Stress intensity and crack growth opening area solutions for through-wall cracks in cylinders and spheres", *WRC Bulletin 478*, Welding Research Council, New York.

[10] John, H. et al. (1988), "Critical two-phase flow through rough slits", *International Journal of Multiphase Flow*, 14 (2), pp. 155-174.

[11] Paul, D.D. et al. (1991), *Evaluation and refinement of leak-rate estimation models*, US Nuclear Regulatory Committee, Washington, United States.

[12] Burnell, J.G. (1947), "Flow of boiling water through nozzles, orifices and pipes", *Engineering*, 164, pp. 572-576.

[13] Henry, Robert E. (1970), "The Two-Phase Critical Discharge of Initially Saturated or Subcooled Liquid", *Nuclear Science and Engineering*, 41 (3), pp. 336-342.

[14] Rahman, S. et al. (1995), Probabilistic Pipe Fracture Evaluations for Leak-Rate-Detection Applications" *NUREG/CR-6004, BMI-2174*.

[15] Abdollahian, D. and B. Chexal (1983), "Calculation of Leak Rates Through Cracks in Pipes and Tubes", *EPRI NP-3395, Project 1757-19*, Campbell.

[16] Nikuradse, J. (1933), Strömungsgesetze in rauhen Rohren", *Forschung auf dem Gebiet des Ingenieurwesens*, 361 (B4), pp. 1-22.

[17] Heckmann, K. et al. (2022), "A Metastable Jet Model for Leaks in Steam Generator Tubes", *Nuclear Engineering and Design,* Vol. 389.

[18] Zaloudek, F.R. (1963), *The critical flow of hot water through short tubes*, US Atomic Energy Commission (USAEC), Richland.

[19] Pana, P. (1975), *A modified Bernoulli-equation for the computation of fluid flow in the subcooled regime* (in German), Cologne.

[20] Nuclear Safety Standards Commission (KTA) (2016), *Break Preclusion Verifications for Pressure-Retaining Components in Nuclear Power Plants*, KTA 3206, Bundesamt fuer kerntechnische Entsorgungssicherheit (BfE), Salzgitter.

[21] Pana, P. and M. Müller (1978), "Subcooled and two phase critical flow states and comparison with data", *Nuclear Engineering and Design*, 45 (1), pp. 117-125.

[22] ANSYS (2020), *ANSYS CFX-Solver Theory Guide*, Release 2020 R1 ANSYS, Inc.

[23] Cox, A., B.A. Young and P.M. Scott (2013), "Advances in COD Modeling: Validation of an Analytical Model to Experimental Results", *Structural Mechanics in Reactor Technology (SMiRT) 22, Division II – Fracture Mechanics and Structural Integrity*, San Francisco.

[24] Young, B.A., R.J. Olson. and P.M. Scott (2013), "Advances in COD Modeling – Multiple Loading Modes: Concurrent Axial and Crack Face Pressure with a Subsequent Applied Bending Moment", *Structural Mechanics in Reactor Technology (SMiRT) 22, Division II – Fracture Mechanics and Structural Integrity*, San Francisco.

[25] Young, B.A., R.J. Olson and M. Kerr (2012), "Advances in COD Modeling: Circumferential Through-Wall Cracks", *ASME International, PVP 2012*, Toronto.

[26] The International Association for the Properties of Water and Steam (IAPWS) (2005), *Obsolete IAPWS recommendations*.

[27] Norris, D.M. and B. Chexal (1987), *PICEP: Pipe Crack Evaluation Program (Revision 1)*, Report EPRI-NP-3596-SR-Rev.1, Electric Power Research Institute, Palo Alto.

[28] Bläsius, C., K. Heckmann and J. Sievers (2019), "Quality Management, Verification, and Validation of Structure Mechanical Computer Codes at GRS. Division III", *Structural Mechanics in Reactor Technology (SMiRT-25)*, 4-9 August 2019, Charlotte.

[29] US NRC (2007), "Standard Review Plan: 3.6.3 Leak-Before-Break Evaluation Procedures", NUREG-0800, Rev. 1, US Nuclear Regulatory Commission, Washington DC.

[30] Silber, F. et al. (2017), "Investigation of Leakage Rates in Pressure Retaining Piping", ASME 2017 Pressure Vessels and Piping Conference, 16-20 July 2017, Waikoloa.

[31] Herbst, O., N. Huber and W. Kastner (2001), "Application of the Leak Flow Rate Calculation Program FLORA to Real Cracks in Piping", *SMiRT 16*, August 2001, Washington DC.

[32] The American Society of Mechanical Engineers (ASME) (2021), *Boiler and Pressure Vessel Code (BPVC) Section III – Rules for Construction of Nuclear Facility Components-Division 1-Subsection NB-Class 1 Components*, BPVC-III NB – 2021.

[33] Kim, Y.-J. et al. (2004), "On Relevant Ramberg-Osgood Fit to Engineering Nonlinear Fracture Mechanics Analysis", *Journal of Pressure Vessel Technology*, Vol. 126, pp. 277-283.

[34] xLPR Technical Seminar Series (2020): Models Overview, http://www.youtube.com/watch?v=vsOOtdXYxoY (deterministic models start at 25:30; COD at 57:30; LEAPOR at 59:30, accessed 8 December 2023).

[35] Scott, P. et al. (2010), *Development of the PRO-LOCA Probabilistic Fracture Mechanics Code*, MERIT Final Report, https://inis.iaea.org/collection/NCLCollectionStore/_Public/42/011/42011406.pdf?r=1&r=1, Swedish Radiation Safety Authority.

[36] Homiack, M. and M. Burkardt (2017), xLPR Version 2.0 Inputs Group Report, Appendix B, ADAMS Accession Number ML19337B876.

[37] Benson, M., B. Young, D-J. Shim and F. Brust (2013), *Crack Opening Displacement Model for Through-Wall Axial Cracks in Cylinders*, Proceedings of the 2013 ASME Pressure Vessels and Piping conference, 14-28 July 2013, Paris.

[38] Henry, R.E. and H.K. Fauske (1970), "Two-Phase Critical Flow at Low Qualities, Part II: Analysis", *Nuclear Science and Engineering*, 41 (1970), pp. 92-98.

[39] Williams, P.T. et al. (2017), *LEAPOR – A Computer Code for Leakage-Rate Calculations Cracks in Cooling Water Piping Systems*,Proceedings of the ASME 2017 Pressure Vessels and Piping Conference, 16-20 July 2017, Waikoloa.

[40] Williams, P.T. et al. (2021), *Comparative Assessments of Different Leakage-Rate Models for ATLAS+*, Proceedings of the ASME 2021 Pressure Vessels and Piping Conference, 12-16 July 2021.

[41] Young, B.A. (2013), *xLPR Software Design Description for a Circumferential Through-Wall Combined Tension and Bending COD Module*.

[42] Kumar, V. and M.D. German (1988), *Elastic-Plastic Fracture Analysis of Through-Wall and Surface Flaws in Cylinders*, EPRI Report NP-5596, Research Project 1237-5, Electric Power Research Institute, Palo Alto.

[43] Keim, E. and R. Rippel (1991), *Bestimmung von Leckflächen, Rißöffnungen und Leckraten*, KWU E121/91/058, 1991.

[44] Reimann J. (1984), "Vergleich von Kritischen Massenstrom-Modellen im Hinblick auf die Strömung Durch Lecks," Leck-vor-Bruch-Verhalten Druckbeaufschlagter Komponenten, Fortschr.-Ber. VDI-Z. 18(14), pp. 63-95.

[45] IAEA (2019), "Deterministic safety analysis of nuclear power plants", *Specific Safety Guide SSG-2 Rev. 1*, International Atomic Energy Agency, Vienna.

[46] NEA (1995), *Report on round robin activities on the calculation of crack opening behaviour and leak rates for small bore piping components*, OECD/NEA, OCDE/GD(95)90, NEA/CSNI/R(95)4, OECD publishing, Paris, www.oecd-nea.org/jcms/pl_16054.

[47] Schmid, S. (2021), "Leak rate testing in the range of leak detection systems", *Nuclear Engineering and Design*, 372 111000.

Appendix

This appendix presents the leak rate tests and the test facility where the main source of cases was performed. It should be stated that the information presented in this appendix was not distributed to the participants in the analysis phase of the benchmark; it serves at this place for further information for interested readers of this report. The test facility is the fluid-structure-interaction (FSI) test rig, depicted in Figure A.1, which is located at the Materials Testing Institute (MPA) at the University of Stuttgart, Germany.

Figure A.1 FSI test rig
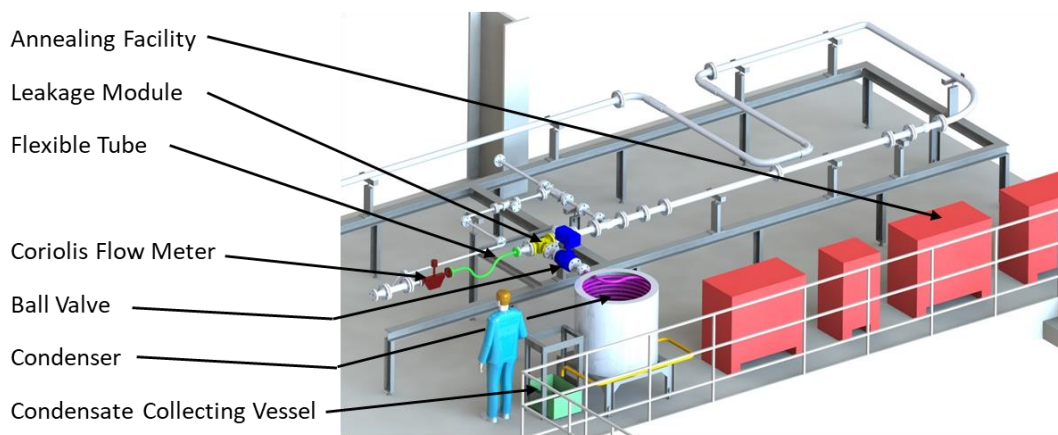
In this test rig, water as a fluid circulates within a closed loop and allows a variety of experimental opportunities. It can be operated up to pressure of 8 MPa and temperatures of up to 270°C. The leakage module within the test rig makes it possible to insert a specific type of leak specimens; due to the operating requirements of the test rig, specimens with a leak rate of up to 0.2 kg/s can be tested. The water and steam lost through the leak are condensed and collected in a vessel equipped with a load cell. The leak rate can be quantified from the increase of mass in the vessel over time; an additional estimate comes from differential flow measures in the test rig upstream and downstream of the leak measurements with Coriolis flow meters. The specimens used in the first benchmark phase are shown in Figure A.2, while the specimens used in the second benchmark phase are shown in Figure A.3.

Figure A.2. First benchmark phase artificial slit specimen (left) and fatigue crack specimen (right)
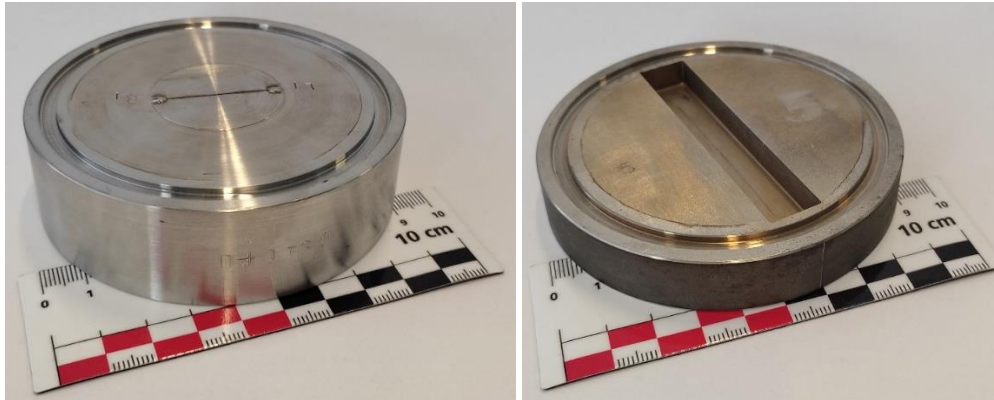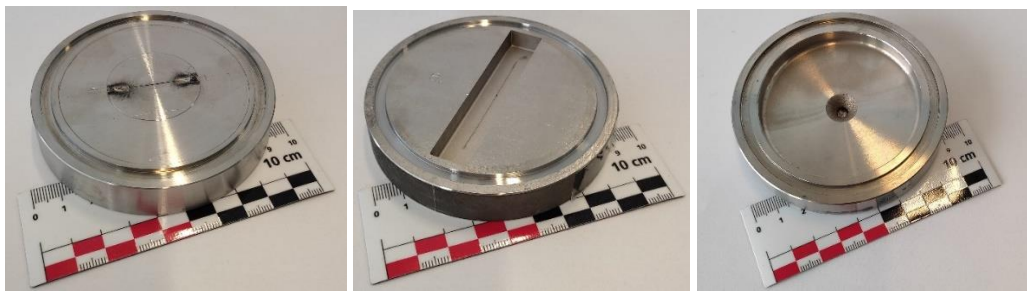

Figure A.3. Second benchmark phase specimens: Artificial slit (left), fatigue crack (centre), and a detail of the thin specimen for steam generator tube leak testing (right)

From a large number of different fluid test conditions available, six points were selected for each specimen for this benchmark study. More details about the test procedures and additional results can be found in [30] and [47].